Synthesis and characterization of electrospun organic-inorganic hybrid graft copolymer nanofibers of poly(methyl methacrylate) and polydimethylsiloxane

By

Morne Swart

Thesis presented in partial fulfillment of the requirements for the degree of Master of Science at the University of Stellenbosch

Study leader
Dr. PE Mallon

Stellenbosch
December 2007

I, the undersigned, hereby declare that the work contained in this thesis is my own original work and that I have not previously in its entirety or in part submitted it at any university for a degree

Signature: ……..

Date: ……..

Dedicated to my parents,
your love and guidance will always be my cornerstone

And to Chanél,
for your love, support and being there every step of the way

Abstract

Two series of poly(methyl methacrylate)-graft-poly(dimethylsiloxane) copolymers were synthesized via conventional free radical copolymerization of methylmethacrylate and monomethacryloxypropyl terminated PDMS macromonomers of different lengths. It is shown how these copolymers can be electrospun to produce the copolymer nanofibers. The affects of copolymer compositions, the electrospinning tip-to-collector (TCD) distance and the concentration of the polymer solution on the fiber morphology are discussed. Scanning Electron Microscopy (SEM) and Transmission Electron Microscopy (TEM) were used to establish the surface topography as well as the fiber morphology of the electrospun copolymer nanofibers. It is also shown that these nanofibers produce superhydrophobic surfaces where the preferential surface segregation of the PDMS component is combined with the roughness of the nanofiber surface. It is shown that after exposure of these nanofiber surfaces to corona discharge, the initial superhydrophobic surfaces become easily wettable. The samples show the phenomena of hydrophobicity recovery after corona exposure. The rate and extent of this recovery depends on the PDMS content of the nanofibers as well as the time of corona treatment. The hybrid copolymer nanofibers were evaluated as potential reinforcing fillers for cross linked polydimethylsiloxane compounds. The fibers show a remarkably good distribution in the PDMS matrix and show a dramatic improvement in the mechanical properties of the composites.

Opsomming

Twee verskillende poli(metiel metakrilaat)-g-poli(dimetiel siloksaan) polimeer reekse met ‘n variasie in die lengte van die PDMS makromonomeer syketting is geproduseer seur konvensionele vrye radikaal ko-polimerisasie. In hierdie studie word dit getoon hoe die ko-polimere ge-elektrospin kan word om nanovesels te vorm. Die effek wat ko-polimeer komposisie, electrospin afstand en polimeer konsentrasie op die vessel morphologie het word ook ondersoek en bespreek. Skandering Elektron Mikroskopie (SEM) en Transmissie Elektron Mikroskopie (TEM) word gebruik om die oppervlak topografie en vessel morphologie van die ko-polimeer nanovesels vas te stel. Hierdie nanovesels produseer oppervlaktes wat super-hidrophobies is. Dit word bewerkstellig deurdat die PDMS component, tesame met die natuurlike growwe oppervlak van die nanovesels, by voorkeur oppervlak segregasie ondergaan. Dit word ook getoon dat na blootstelling aan korona ontlaaing (veroorsaak deur hoë spanning) die nanovesels se oorspronklike super-hidrophobiese karakter verander na super-hidrophilies. Die hidrophobiese herstelling verskynsel word egter gesien na ‘n sekere periode na hoë spanning blootstelling. Die hoeveelheid en tempo van die herstelling is egter afhankilik van die hoeveelheid PDMS in die nanovesels sowel as die tyd wat die vesels aan hoë spanning ontlaaing blootgestel is.

Acknowledgements

The author would like to convey his sincere thanks to the following:

A special thanks to Dr. Peter Mallon for his interest, enthusiasm, assistance and his always open door policy. Also for giving me the opportunity to travel to Sweden for research.

To Gareth Bayley for all his help, ideas and endless patience to all my questions. And especially for his help with the HPLC and other chromatography aspects of this study. Gareth, I cannot thank you enough!

To Jean MecKenzie and Elsa Malherbe for the running of NMR samples.

To Prof. Mikael Hedenqvist, Richard Olsson, Sung-Woo Cho and Thomas Blomfeldt of the Royal Institute of Polymer Technology (KTH) for their hospitality and help during my stay in Sweden.

The staff at Polymer Science, our often forgotten and unsung heroes, Aneli, Margie, Erinda, Calvin and Oom Hennie.

The Department of Chemistry and Polymer Science, University of Stellenbosch and the National Research Foundation for financial support.

To everyone in lab 134, Wael, Abdu, Mohammed, Muhammed, Gareth and Elana.

On a more personal note, I would like to thank my parents. They gave me the opportunity to be here and further my studies. Mom, Dad, thank you for all your trust, support, love, guidance and encouragement throughout my study career. Also to my brother and sister, thank you for your support throughout.

To all my friends at Polymer Science, Liesl, Maggie, Adine, Adele and Gareth, and to the rest, Christie, Craig, Donna, Leanne, Raymond and Ewan, thanks for every cup of coffee (there were a lot), golf game and braai. You guys made everything much easier.

Lastly and most importantly to my fiancé, Chanel, without your support and love none of this would have been possible. Thank you for being there every step of the way and for being there through the many long nights I spent working on my thesis. You kept me focused and motivated on what is important. For this I can never thank you enough!

Table of Contents

Chapter 1

Chapter 2

Chapter 3

Chapter 4

Chapter 5

Glossary

List of Acronyms

AFM	Atomic Force Microscopy
ATR	Attenuated Total Reflectance
ATRP	Atom Transfer Radical Polymerization
CRS	Confocal Raman Spectroscopy
SCA	Static Contact Angle
DBES	Doppler Broadening of Energy Spectra
DC	Direct Current
DMF	Dimethylformamide
DMSO	Dimethyl Sulfoxide
DSC	Differential Scanning Calorimetry
ELSD	Evaporative Laser Light Scattering Detector
FT-IR	Fourier Transform Infrared
GPC	Gel Permeated Chromatography
GPEC	Gradient Polymer Elution Chromatography
GS	Graham Schmidt Profile
^{1}H NMR	Proton Nuclear Magnetic Resonance Spectroscopy
HPLC	High Performance Liquid Chromatography
LC-FTIR	Liquid Chromatography Fourier Transform Infrared
KOH	Potassium Hydroxide
MMA	Methyl methacrylate
NMR	Nuclear Magnetic Resonance
PAS	Photo Acoustic Spectroscopy
PDMS	Poly(dimethyl siloxane)
PMMA	Poly(methyl methacrylate)
PS	Polystyrene
SEC	Size Exclusion Chromatography
SEM	Scanning Electron Microscopy
TCD	Tip-to-Collector Distance
TEM	Transmission Electron Microscopy
Tg	Glass Transition Temperature
THF	Tetrahydrofurane
UV	Ultra-violet
VBC	4-vinylbenzyl chloride
wt%	Weight Percentage

XPS	Angle resolved X-ray Photoelectron Spectroscopy

List of Symbols

$\gamma_{sg,sl,\mathrm{lg}}$	Surface tension of solid/gas, solid/liquid and liquid/gas interfaces
r	Roughness factor
θ_a	Advancing Contact Angle
θ_r	Rear Contact Angle
k	Rate constants
r_1, r_2	Reactivity ratios
M_n	Number average molecular weight
M_w	Weight average molecular weight
V_r	Volume fraction
m_r	Residual mass of polymer
m_s	Residual mass of solvent
ρ_r	Density polymer
ρ_s	Density solvent
M_c	Average molecular mass between crosslinks
χ	Solvent interaction parameter
V_{ms}	Molar volume solvent
E_+	Incident energy
Z	Penetration depth

List of Figures

Chapter 2

Chapter 3

Chapter 4

Appendix

List of Tables

Chapter 2

Chapter 4

List of Schemes

Chapter 2

Chapter 3

Introduction and Objectives

In this chapter hybrid materials and electrospinning are discussed briefly as a general introduction. Synthesis and subsequent characterization and possible applications of the resultant materials are also discussed briefly. The objectives of the study are also summarized.

1.1 Introduction

The demand for materials with specific properties, showing improved characteristics and that are multifunctional is almost increasing daily. Hybrid polymers have the ability to combine properties of different materials into that of a single individual material. In this project a series of organic-inorganic hybrid graft copolymers based on poly(methyl methacrylate) and polydimethysiloxane (PMMA-g-PDMS) were synthesized. The polymers were prepared via the grafting through technique. Here a PDMS macromonomer was used with conventional free radical polymerization to produce the graft hybrids. The properties of PDMS and PMMA are vastly different. PDMS has a very low glass transition temperature (T_g = -125^{o}C), due to the flexible backbone of the siloxane linkages. When molecular weights are sufficiently high enough chains become entangled and this leads to an unusually high level of viscoelasticity. PMMA is a clear, colorless polymer with good weatherbility properties and high scratch resistance. However, PMMA generally has a very low impact strength and poor chemical resistance. By combining these two individual polymers to produce a hybrid material a superior polymer was created showing characteristics of both. These hybrid materials were also electrospun to produce non-woven nanofibers mats.

Electrospinning is a remarkably simple method for generating nanofibers of polymers and it provides a versatile technique for producing nanofibers with either a solid, porous, or hollow structure. Flexibility in surface functionalities, and superior mechanical performance (e.g. stiffness and tensile strength) compared with any other known form of the material ensures that the resultant polymer nanofibers have outstanding properties[1]. From 1934 to 1944, Formhals published a series of patents[2-6] where he describes an experimental setup for the production of polymer filaments using an electrostatic force.

These non-woven nanofiber mats essentially produced infinitely rough surfaces. In addition the PDMS component provided a very low surface energy to the nanofibers and therefore produced an overall “superhydrophobic surface” (water contact angle of greater than 150°). Modification of the surface by corona discharge will also be investigated. This treatment has the potential to change the superhydrophobic surface into a superhydrophilic one using a very simple electrical discharge.

Superhydrophobic and superhydrophilic surfaces produced in this way have possibly have many applications in the field of bioengineering (both polymer components are bio-

compatible) and electronics. This technique has the potential to produce these surfaces at a low cost.

A further investigation on using the electrospun nanofibers as a possible reinforcing filler in a silicone matrix was also done. The modification of the resultant reinforced composite for the production of templating materials was also investigated.

Analysis and characterization of the synthesized bulk graft copolymer and the electrospun nanofibers were done by making used of a multitude of analytical techniques. These included Nuclear Magnetic Resonance (NMR), Size Exclusion Chromatography (SEC), Gradient Elution High Performance Liquid Chromatography (HPLC), Scanning Electron Microscopy (SEM), Transmission Electron Microscopy (TEM), Static Contact Angle Measurements (SCA), Slow Positron Annihilation Spectroscopy (SLOPOS), LC transform FTIR, Confocal Raman Spectroscopy, Differential Scanning Calorimetry (DSC) and Thermo-gravimetric Analysis (TGA). All of the above mentioned techniques helped to classify the chemical, physical and morphological characteristics of the hybrid polymers.

1.2 Objectives

The following objectives were set out at the start of the study:

- Synthesis of PMMA-g-PDMS copolymer with varying PDMS branch lengths.
- Development of an electrospinning process that produces PDMS containing hybrid non-woven nanofiber mats.
- Evaluation of varying spinning conditions (i.e. spinning distance, spinning voltage, solution concentration, etc.) on the morphology of the hybrid polymers
- Evaluation of the surface morphology and possible preferential surface segregation of the PDMS component.
- Evaluation of the hydrophobic nature of the polymer via SCA and determination of the reasons for the hydrophobicity.
- Surface modification of polymer via high voltage corona discharge and the effects of the modification on the hydrophobic character of the polymer as well as on the surface morphology.
- Preparation of crosslinked PDMA composites using the nanofibers as a filler
- Evaluation of the physical properties of the composites.

1.3 References

1. Huang, Z.; Zhang, Y. Z.; Kotaki, M.; Ramakrishna, S. *Comp. Sci. Technol.* **2003,** 63, 2223–2253.
2. Formhals, A. *US Patent* **1934,** 1,975,504.
3. Formhals, A. *US Patent* **1939,** 2,160,962.
4. Formhals, A. *US Patent* **1940,** 2,187,302.
5. Formhals, A. *US Patent* **1943,** 2,323,025.
6. Formhals, A. *US Patent* **1944,** 2,349,950.

Historical and Literature Review

This chapter gives an introduction to the field of hybrid materials with regards to synthesis, characterization, applications and their ability to produce superhydrophobic surfaces. Also discussed is the electrospinning process and its ability to produce nanofibers

2.1 Hybrid materials

Because the need for novel materials with improved or specific properties are ever increasing, the ability to control molecular structure on an atomic and molecular level is of the utmost importance to produce materials with specific programmed activities. Well established materials like metals, ceramics and plastics cannot fulfill mans need for various new applications. Hybrid polymers have the ability to combine different properties of individual materials into that of a single material. These novel materials show improved characteristics like better mechanical properties. An example of such hybrids are fiber reinforced polymers. A hybrid material is a material that includes two or more moieties blended together on a molecular scale[1]. The forms in which one of these moieties is incorporated into another vary from lamallae, particles, fibers, meshes, etc. or in single molecules for example by condensation polymerization. Ways of synthesizing well-defined hybrid polymers are discussed by Jeffrey Pyun *et al*[2].

Most often one of the compounds used is inorganic and the other organic in nature. Another way of defining a hybrid material is to distinguish between the interactions connecting the organic and inorganic species. By using this definition hybrid materials can be classified into two classes. Class I materials are those types that show weak interactions between the different phases, such as van der Waals forces, hydrogen bonding or weak electrostatic interactions. Class II hybrids consist out of strong chemical interactions between the phases. In addition to using the bonding characteristics to define hybrid materials, structural properties can also be used to distinguish between various hybrid materials[1].

2.1.1 PDMS based hybrid materials

Poly(dimethylsiloxane) (PDMS)-based hybrids are widely used as insulating materials, in medical devices, as membranes, in optical parts and antifouling and water-repellent coatings. PDMS based hybrid polymers are well known in literature. Chain architectures vary from statistical (also known as periodic), gradient, block, grafts, comb, multi-arm and dendrimeric. These architectures can be seen in Figure 2.1. Here dark balls represent the organic component of the polymer and the lighter balls represent the inorganic components.

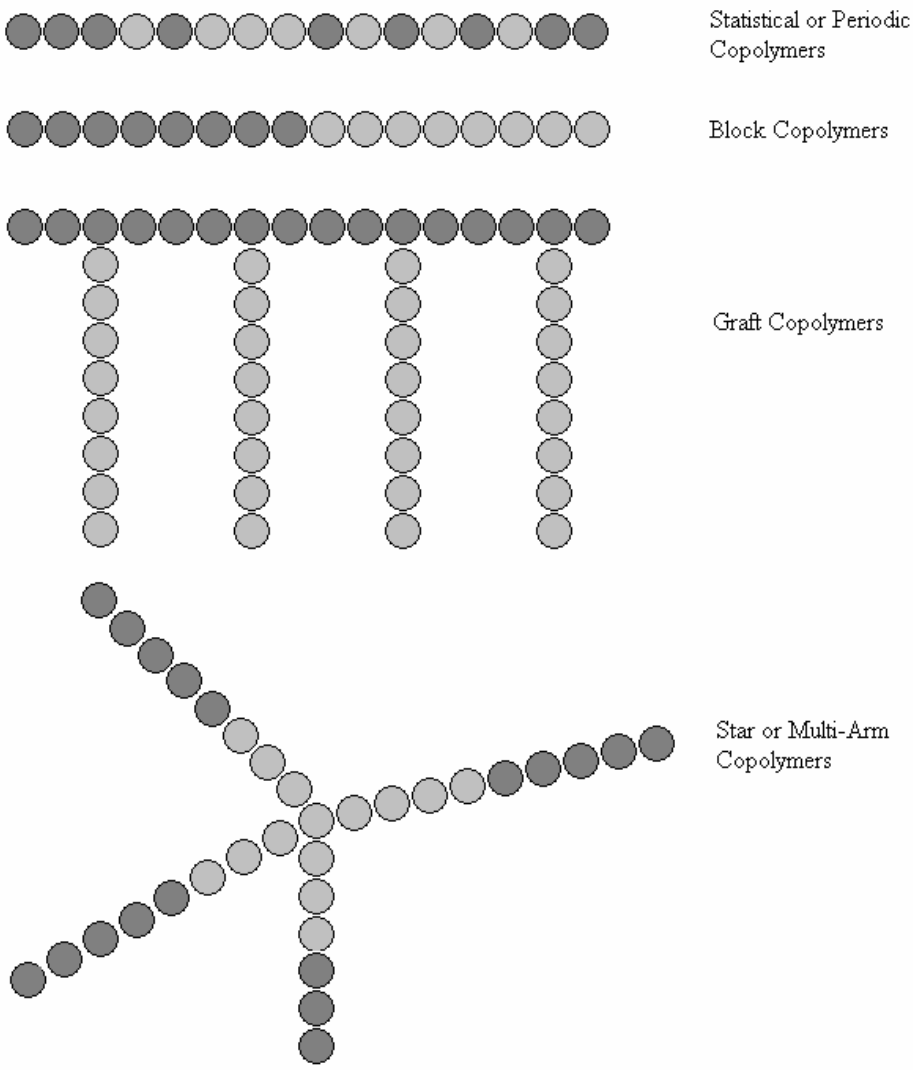

Figure 2.1 *Graphic illustration of different chain architectures.*

Several papers discuss ways of synthesizing PDMS hybrids consisting out of block copolymers. Minglin Ma *et al*[3] synthesized a poly(styrene-b-dimethylsiloxane) diblock copolymer. This hybrid polymer was synthesized via sequential controlled anionic polymerization of styrene and then hexamethylcyclotrisiloxane (D_3). The synthesis of this polymer is shown in the reaction scheme below.

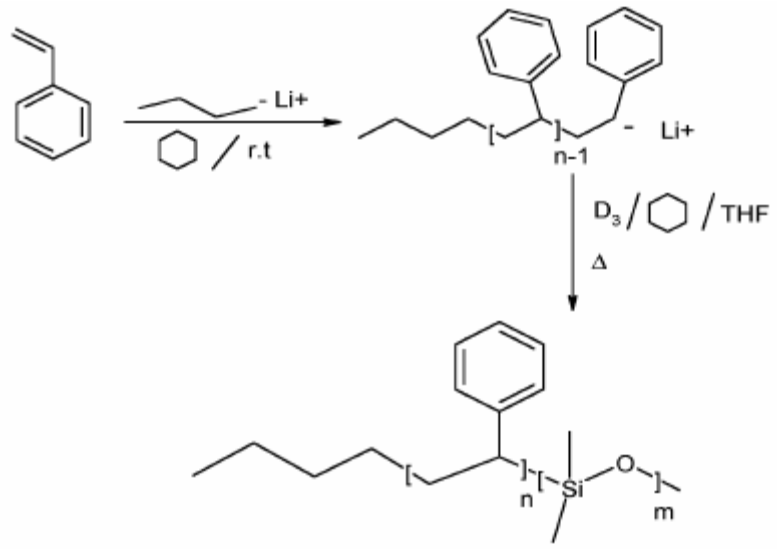

Scheme 2.1 *Synthesis of Poly(Styrene-b-Dimethylsiloxane) block copolymers*

In this case, calorimetric studies showed a considerable segregation between the polystyrene and poly(dimethylsiloxane) blocks.

Mark *et al*[4] first used the sol–gel method to prepare PDMS networks containing *in situ* precipitated silica; this kind of inorganic/organic hybrid material has been intensively studied[5-7]. They investigated the bulk and surface composition, structure and morphology of the hybrids with different amounts of inorganic components. Martos *et al*[8] used inverse gas chromatography to measure the surface energy of silica–TEOS–PDMS hybrids with 60 wt% inorganic component and reported that the amount of PDMS was not enough to cover all silica surfaces. This resulted in different surface energies of the surfaces, originating from the presence of hydroxyl groups on silica surfaces. In a similar study Han *et al*[9] added a small amount of PDMS. They claimed that during the sol–gel process the hydrophobic PDMS tended to be localized at the surface, thereby lowering the free energy of the system.

The various applications for graft copolymers are also in great demand. This is mainly due to the fact that these materials often show improved impact resistance and thermal properties. The uses of these polymers vary from impact resistant plastics, emulsifiers, thermoplastic elastomers to compatibilizers. Many components can be varied to produce these polymers with specific tailored characteristics to improve or enhance properties of existing materials. Shinoda *et al*[10-12]showed that control over the distribution of branch spacing could be obtained by making use of methacrylate-terminated PDMS macromonomers with MMA to produce copolymers. Using different techniques to produce PMMA-g-PDMS hybrid graft

copolymers, the spacing of the branches along the main chain could be varied. They produced polymers that were heterogeneously branched by making use of conventional free radical polymerization, homogeneously branched polymers by making use of ATRP and tapered structured polymers by RAFT polymerization. Figure 2.2 show a schematic of the different type of chain structures produced.

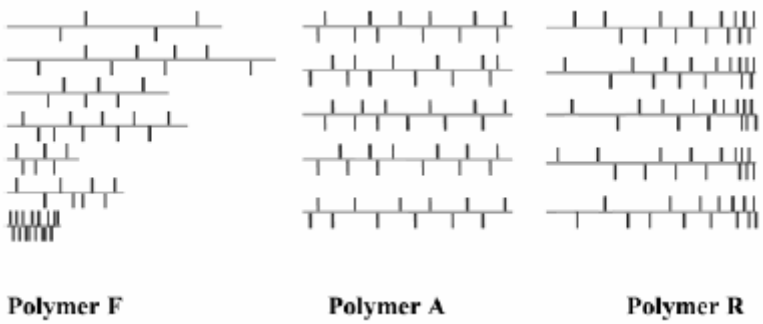

Figure 2.2 *Reaction schemes showing the different PDMS branch distributions obtained. Polymer F shows heterogeneous distribution, polymer A shows homogeneous distribution and polymer R shows a tapered structure*[10].

Knauss *et al*[13] reported on the synthesis and characterization of star block copolymers. They used convergent living anionic polymerisation to synthesize PDMS polymers with star shaped polystyrene end blocks. These uniquely branched siloxane containing triblock copolymers were synthesized by combining convergent living anionic polymerisation of styrene with living anionic ring opening polymerisation of hexamethylcyclotrisiloxane.

2.2 Superhydrophobicity

There are various different examples of superhydrophobic surfaces[14]. These include the wings of a butterfly[15] and the leaves of various plants like that of the cabbage and Indian cress[16]. Maybe the best known example of a super- or ultra-hydrophobic surface, is that of the self-cleaning lotus plant or *Nelumbo nucifera.*

2.2.1 Superhydrophobicity in general

The affinity that surfaces have towards water can be classified into four main groups[17]. The method used to establish these groups is known as the static contact angle. The contact angle can be defined as that angle at which a liquid-vapour interface meets a solid surface. The

basic laws for determining the equilibrium shape of a water droplet on the surface were formulated by Thomas Young[18]. The interactions across the three interfaces; the solid/gas, the liquid/solid and the liquid/gas interface determine the shape of the drop on the surface. The forces per unit length acting on this three phase line are known as the surface tension. The balance of these forces leads to the famous Young's equation shown below.

$$\gamma_{sg} - \gamma_{sl} = \gamma_{\mathrm{lg}} \cos\theta$$

The symbol γ represents the surface tension between the three different surface interfaces. If the drop is small enough (normally in the millimetre to micrometer scale) the effect of gravity can be ignored. The drop will then have the form of a spherical cap and the liquid/gas interface meets the solid at an angle, which is called the intrinsic contact angle.

As mentioned above, contact angles can be classified into four groups; superhydrophilic, hydrophilic, hydrophobic and superhydrophobic[17]. Hydrophilic surfaces exhibit contact angles between 10^o and 30^o. With surfaces that have a large affinity for water (as well as materials that absorb water) the water droplet will completely spread over the surface and results in a 0^o contact angle. These surfaces are classified as superhydrophilic. Hydrophobic surfaces are incompatible with water and show a contact angle of between 70^o and 90^o. Some surfaces, however, are completely incompatible with water and water droplets simply rest on the surface without actually wetting the surface to any significant extent. These surfaces are classified as superhydrophobic and show contact angles of between 150^o to 180^o. Materials that exhibit these properties include fluorinated surfaces like Teflon coatings[18].

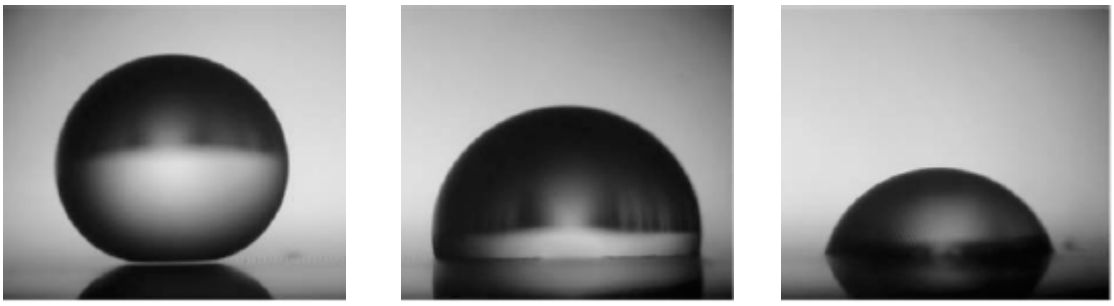

Figure 2.3 *Example of different contact angles ranging from superhydrophobic to hydrophilic[19].*

Water repellency is not only affected by the chemical nature of the material, but also has a microtexture origin that influences the affinity for water. Hence there are two origins for the

effect of water repellency, either the liquid follows the solid surface, or it leaves air inside the texture[19]. This is illustrated below where Figure (a) shows the case where the water follows the surface and Figure (b) shows where air is trapped inside.

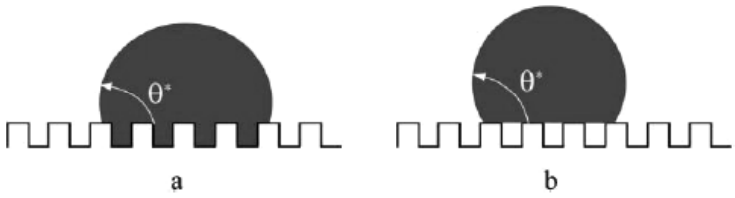

Figure 2.4 *Illustration of different origins that affect water repellency[19].*

In the first case, illustrated by Figure (a) (the Wentzel scenario), the increase of the surface area due to the microtextured effect, increases the hydrophobicity of the material. In the second state (known as the Cassie state) the water droplet only makes contact with the top asperities, thereby leaving air below the droplet. This leads to a higher contact angle.

The parameter governing the contact angle θ* on the surface in the Wentzel scenario is known as the solid roughness factor, r. This parameter is defined as the ratio between the true surface area over the apparent one. This leads to the following equation:

$$\cos\theta^* = r\cos\theta$$

where θ is the Young's contact angle on the smooth surface.

Out of this equation we would expect to find that the rougher the surface the more hydrophobic. This, however, is not always the case mainly due to two reasons. (1) In contrast with the equation above, the contact angle is generally spread over a large interval. This interval is responsible for the sticking of drops to the surface and is often referred to as the contact angle hysteresis. In the Wentzel state the hysteresis is very large yielding a low receding contact angle hence giving the surface an almost hydrophilic property[19, 20]. (2) The energy stored for following the solid surface in very rough materials is much larger than the energy associated for leaving air pockets under the water droplet. A more detailed description of the parameters governing contact angles can be found in the paper "On water repellency", by Mathilda Callies *et al*[19].

2.2.2 The Self-Cleaning Effect

Another important characteristic that goes with superhydrophobicity is the so-called "self cleaning" property of these materials. To clean a surface, material has to be transported off it. There are basically two ways in which this can occur. With a very wettable surface decontamination can be based on film flow. Non-wettable surfaces, however, like that of the Lotus leaf have a built-in cleaning mechanism. David Quere *et al* studied the dynamic behaviour of super- or ultra-hydrophobic surfaces in great detail[21]. Because the contact area decreases with increasing contact angle, the contact line (formed by the three phase interfaces) can be deformed less easily and hence the hysteresis in the contact angle between the advancing and receding angles is drastically reduced. The advancing angle θ_a is the front angle in the direction of the droplets' motion and the receding angle θ_r is the rear angle. A simple way to measure the contact angle hysteresis is the pinning force per unit length (F) of the drop parameter given by the equation below:

$$F = \gamma_{lg}(\cos\theta_r - \cos\theta_a)$$

Where θ_a is the front angle, θ_r is the rear angle and γ_{lg} is the surface tension of the liquid/gas interface. It is this contact angle hysteresis that is responsible for droplet motion and hence the self-cleaning effect. If the hysteresis is too large and the driving force too low, the drop would stick to the surface or be smeared across it. Below is an illustration of the self-cleaning effect.

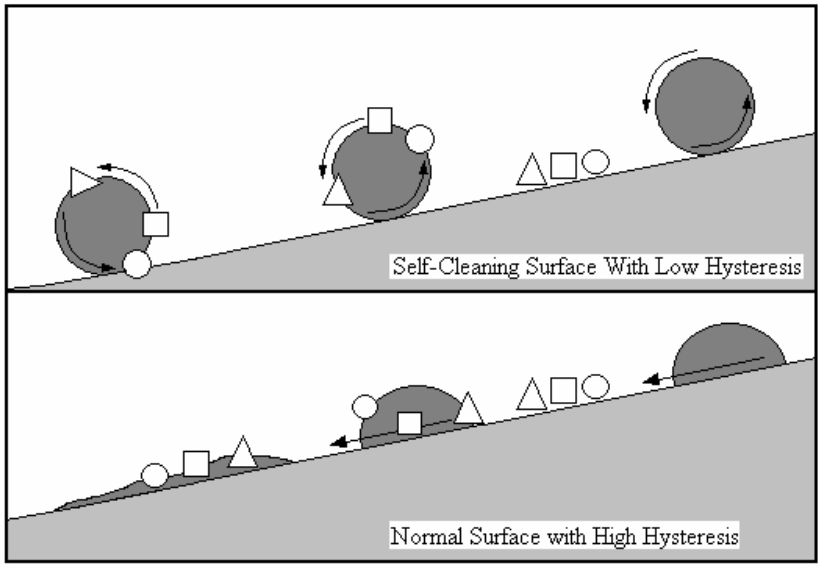

Figure 2.5 *Illustration of the difference between a self- cleaning surface and a non-self-cleaning surface.*

2.2.3 Ways of making superhydrophobic surfaces

The first group to make artificial superhydrophobic surfaces was that of Kao[22] in the mid 1990's. Since then a number of very innovative ways have been used to manufacture these surfaces. Besides water repellency, other properties like colour, transparency, flexibility etc. have also been incorporated into these systems.

Techniques to manufacture superhydrophobic surfaces can be divided into two main categories. The first is to make rough surfaces from low surface energy materials and the second is to modify a rough surface of a material with low surface energy.

2.2.3.1 Roughening of a low surface energy material

Several ways of roughening a surface can be used to produce superhydrophobic surfaces. They include mechanical stretching[23], laser plasma/chemical etching[24, 25], lithography[26], sol-gel processing and solution casting[27], layer by layer and colloidal assembling[28], electrical and chemical reaction[29] and electrospinning[3]. These are but a few ways of producing roughened surfaces.

One group of materials that is of great interest is fluorocarbons. The reason for this is because of its extremely low surface energy. An effective way of using this material to produce superhydrophobic surfaces was put forth by Zang *et al*[23]. They used mechanical stretching of tetrafluoroethylene (Teflon®) film. By doing so the film consists of fibrous crystals with a large fraction of void space in the surface. Shiu *et al*[24] on the other hand used oxygen plasma to treat Teflon® and thereby obtained a rough surface structure. Shimomura[30] prepared a porous membrane by casting fluorinated block polymer solution under humid atmospheric conditions. Another material readily used for its low surface energy is polydimethylsiloxane (PDMS). To roughen the surface, Khorasani *et al*[31] used CO_2-pulsed lasers as an excitation source. The contact angles obtained were in excess of 175^o and it was concluded that the hydrophobicity was due to the high porosity and chain ordering on the PDMS surface. This is illustrated in Figure 2.6 (a) below. Another popular method is to make a negative template out of an existing superhydrophobic material, like that of the lotus leaf. By then using that template as a positive template, a nanocasting procedure with PDMS can thereby produce superhydrophobic materials. This is shown in Figure 6 (b). As mentioned previously and illustrated in Figure 6 (c), by electrospinning poly(styrene-b-dimethylsiloxane) with

polystyrene homopolymer Ma *et al*[3] was able to produce superhydrophobic surfaces. Figure 6 (d) shows the result of a PS-PDMS micellar cast solution in humid air done by Zhai *et al*[32].

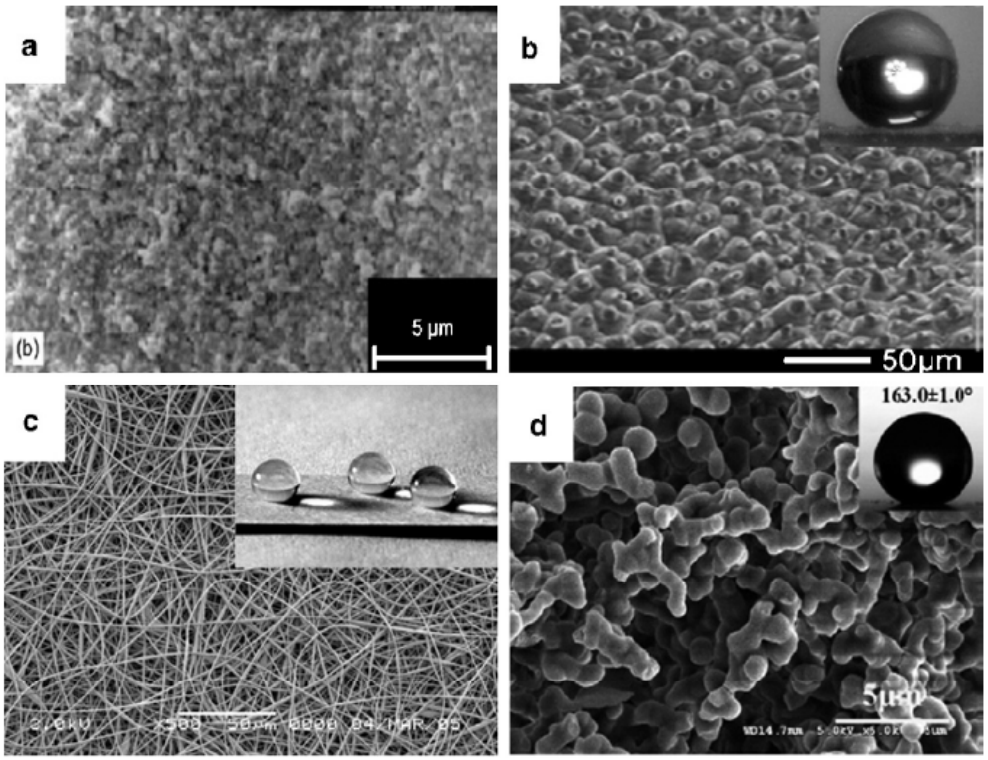

Figure 2.6 *SEM images illustrating different superhydrophobic surfaces obtained by roughening the surface of low surface energy substrates*[14]*. Figure (a) illustrates high porosity and chain ordering, Figure (b) shows a surface prepared via a negative template followed by nanocasting, Figure (c) shows a surface created by electrospinning and Figure (d) is the result of a micellar cast solution in humid air.*

2.2.3.2 Making a rough surface and then modifying it with low surface energy material

Several methods exists to produce these types of materials with modified surface chemistry[14]. They include covalent bond formation between gold and alkyl thiols, the use of silanes, physical binding, adsorption and coating. Teshima *et al*[26] produced transparent superhydrophobic surfaces from a PET substrate by firstly etching it with oxygen plasma and then treating it with plasma enhanced chemical vapour deposition using tetramethylsilane. Numerous other examples exist in literature. Techniques used in these instances include sol-gel processing[21], layer-by-layer and colloidal assembly[22] and electrical reaction and deposition[23].

2.3 Graft Copolymers

There are three main techniques of producing graft copolymers, i.e. grafting onto, grafting from and grafting through[33]. Below follows a short review of each of these techniques.

2.3.1 Grafting Onto

In the grafting onto technique the polymer backbone and the branches (often referred to as arms) are prepared separately by living or controlled polymerizations. The backbone is prepared in such a way that it has reactive groups distributed along the chain. These functional groups can react with the functional groups on the branches made by living polymerization to form a graft copolymer. Mixing the two separate moieties in the desired proportions under the correct conditions allows a coupling reaction to take place resulting in the final comb shaped polymer.

By making use of anionic polymerization the molecular weight, polydispersity and chemical composition of both the branches and polymer backbone can be controlled. The average number of branches can be controlled by controlling the number of functional sites on the backbone as well as by the ratio of the functional groups to the active chain end concentration of the branches used in the coupling reaction. Branches of combed shaped polymers are often prepared by anionic polymerization and backbones with electrophilic functionalities such as anhydrides, esters, pyridine or benzylic halide groups are employed[34]. By determining the overall molecular weight of the copolymer and by knowing the molecular weights of the backbone and branches separately, the actual number of branches in the copolymer can be determined. An example of the grafting onto mechanism can be found by looking at the preparation of poly(butadiene-graft-styrene) graft copolymers[35].

2.3.2 Grafting From

In the grafting from technique, active sites are produced on the main chain. These sites are then able to initiate polymerization of other monomers. Polymerization of other monomers then leads to the formation of the branches and hence the final graft copolymer. The number of branches can once again be controlled by controlling the number of active sites on the polymer backbone, assuming that each site only leads to the formation of one side chain. An

example of grafting from can be seen by looking at the synthesis of a PMMA-g-poly(β-Butyrolactone) copolymer[36].

2.3.3. Grafting Through

Grafting through makes use of the fact that preformed macromonomers can be copolymerised with another monomer to produce graft copolymers. Macromonomers can be classified as oligomeric or polymeric chains with a polymerizable end group. Here the macromonomer then forms the branch of the copolymer where the polymer backbone is created *in situ*. Several factors that control the amount of branches per backbone need to be considered[33].

- Relative ratio of the molar concentrations of the macromonomer and co-monomer
- Copolymerization behaviour of the macromonomer and co-monomer forming the backbone. Depending on the reactivity ratios, r_1 and r_2, of the reacting species, different degrees of randomness can be achieved. Changing concentrations by feeding one or both of the two moieties to the mixture with time, results in the fact that different kinds of graft copolymers can be formed as a function of time.
- Phase separation can also occur due to the formation of the copolymer. This leads to increased molecular weight heterogeneity in the final product.

An example of grafting through can be seen by looking at the synthesis of a PMMA-g-PDMS copolymer via ATRP. PDMS macromonomers can be created by making use of the cyclic trimer hexamethylcyclotrisiloxane or D_3 reaction. In 1969, Frye *et al*. showed that this reaction yields PDMS with a narrow molecular weight distribution[37, 38].

Generally the polymerization of D_3 is initiated using an alkyllithium reagent in a nonpolar solvent (i.e cyclohexane) at room temperature. DeSimone *et al*. confirmed this result in the formation of a monoadduct of initiator with D_3[39, 40]. To allow the reaction to proceed further, the addition of a polar promoter (i.e. tetrahydrofuran (THF) or dimethyl sulfoxide (DMSO)) to the nonpolar hydrocarbon is necessary[38]. This allows the reaction to proceed until all monomer is used and the "living" siloxanolate is terminated.

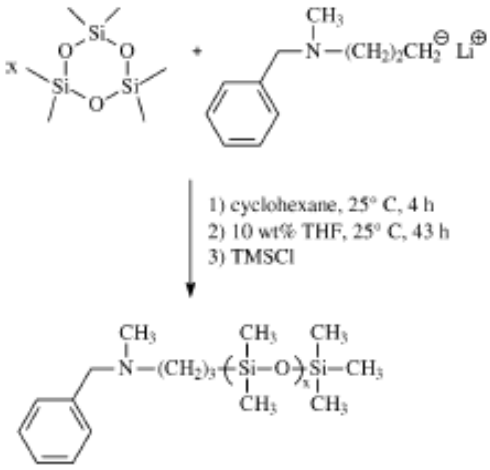

Scheme 2.2 *Anionic Polymerization of D3 Using 3-[(N-Benzyl-N-methyl)amino]-1-propyllithium*[41]

Normally, polymers that are prepared using organolithium initiators are end-functionalized with a variety of post-polymerization reactions. This results in the formation of a macromolecule with a desired functionality on the chain end.

A PDMS macromonomer with methacryloxy terminal functionality can be formed by reacting the siloxanolate anion resulting from the D_3 ring opening reaction with [3-(methacryloxy)propyl] dimethylchlorosilane[42]. The PDMS macromonomer can then be precipitated in methanol and dried under vacuum at 60°C.

The PDMS macromonomer is then reacted with MMA as the co-monomer and Ethyl 2-Bromoisobutyrate. This leads to the formation of a PMMA-graft-PDMS graft copolymer as depicted in the scheme below.

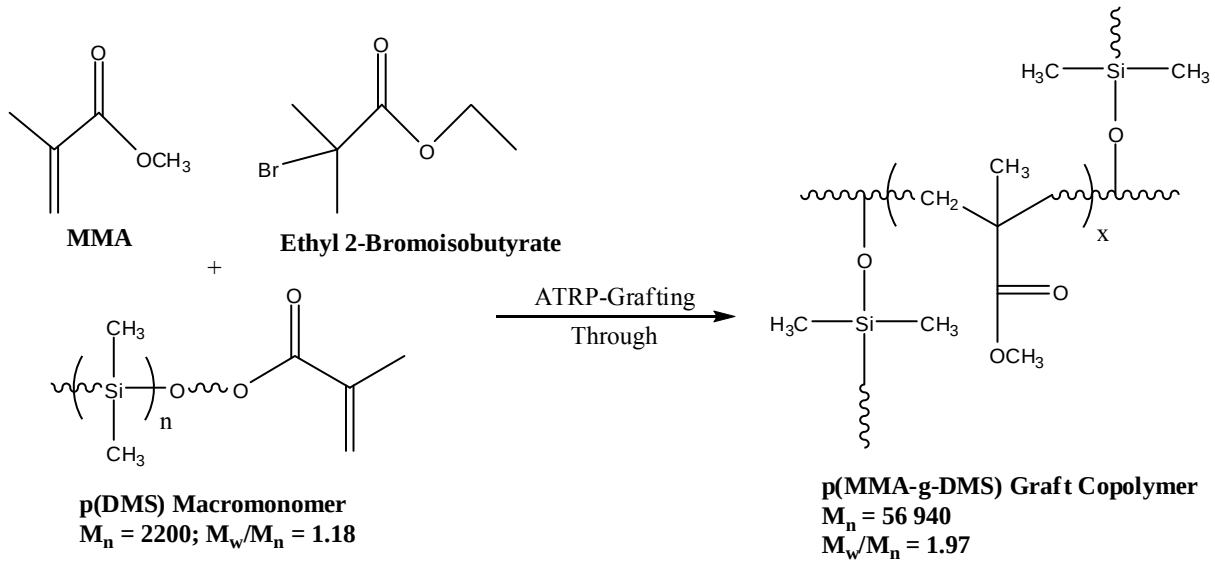

Scheme 2.3 *Synthesis of a PMMA-g-PDMS Graft Copolymer using ATRP*[2]

An important advantage of macromonomers includes control of the number of grafts per copolymer macromolecule. This can be achieved through the choice of the reaction mixture ratio of macromonomer to low molecular weight monomer.

A large number of different macromonomers are available with convenient polymerizable terminal groups, allowing access to a wide range of copolymer compositions[39].

2.4 Electrospinning

To define the term nanofiber, we split the term into two parts, namely "nano" and "fiber". Historically the term "fiber" can be defined from a geometrical standpoint – A slender, elongated, threadlike object or structure[43]. "Nano" refers to physical quantities within a scale of a billionth of the reference unit, be it length, time, weight, etc.

Nanofibers give rise to several interesting characteristics such as very large surface area to volume ratios (which can be as high as 10^3 times that of microfibers) and flexibility in surface functionalities[43]. They also show superior mechanical properties (such as stiffness or tensile strength) compared to that of microfibers, or any other form of the same material. These interesting characteristics, combined by the combination of different properties into that of a single material by making use of hybrid materials, are therefore in great demand. Several processing techniques exist for the production of nanofibers. These include drawing[44],

template synthesis[45, 46], phase separation[47], self assembly[48], electrospinning[49] etc. Drawing, a process very much like that of dry spinning, can produce very long single nanofibers one-by-one. There are, however, certain drawbacks concerned with the drawing process. Only viscoelastic materials can undergo deformation of such a magnitude while cohesive enough to support the stresses developed during pulling. Template synthesis makes use of a nanoporous membrane to make solid or hollow fibers. This method however cannot produce single one-by-one nanofibers. Phase separation and self assembly, although useful, is extremely time consuming. Therefore, the electrospinning process is the only method that is relatively simple and can be used for the production of one-by-one continuous nanofibers, as well as fiber meshes of various polymers and polymer systems.

The fundamental idea of electrospinning dates back over 60 years when Formhals published a series of patents dating from 1934 to 1944[50-54]. Herein he described an experimental setup for the production of nanofiber filaments. Making use of electrostatic force, electrospinning is a process that creates nanofibers through an electrically charged jet of polymer solution or polymer melts. In its simplest form the electrospinning process consists of a pipette (or other type of reservoir to hold the polymer solution), two electrodes and a DC voltage supply in the kV range. The drop of polymer solution that forms at the bottom of the pipette is drawn into a fiber due to the high voltage. The jet is electrically charged and this charge causes the fiber to bend in such a way that its diameter is reduced every time the fiber is looped. Collection of the fiber is done via a web of fibers on the surface of a grounded target, as seen in Figure 7.

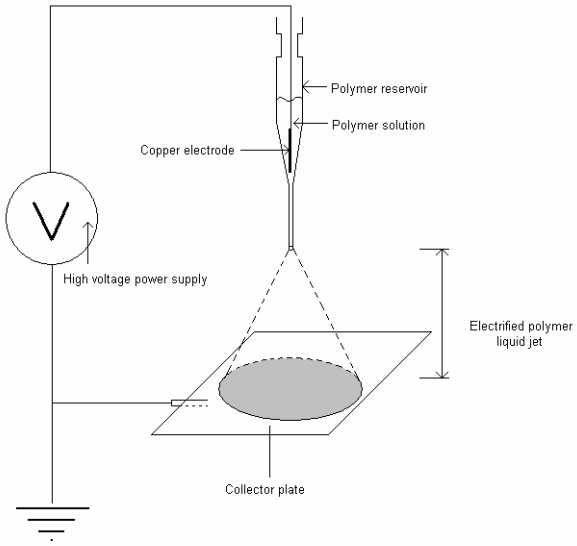

Figure 2.7 Graphic representation of an electrospinning setup

The most important features when looking at the electrospinning process include:

1) Suitable Solvent
2) Suitable vapour pressure
    - The solvent should evaporate quickly for the fiber to maintain its integrity when reaching the target (collector plate), but not too quickly, otherwise the fiber will harden before it reaches the nano-scale.
3) The viscosity and surface tension of the solvent
    - This has an effect on the polymer flow rate or feed
4) The distance between the pipette opening and the collector plate
    - This distance should be large enough to allow solvent evaporation, but not small enough to allow formation of sparks.

2.4.1 The Electrospinning Process

During electrospinning a high voltage causes charges to be induced within the fluid. At a critical amount these charges cause a fluid jet to erupt from the tip of the pipette. This results in the formation of a fluid cone. The jet will travel towards the collector plate (which is at a lower potential). Many factors influence the nanofiber morphology and these factors will be discussed in this section. Electrospinning has been carried out with molten polymer but mostly it is carried out with the polymer in solution[55-58].

The parameters that affect electrospinning may be broadly classified into polymer solution properties, processing conditions and ambient conditions. By varying these parameters, nanofibers of different morphology can be created.

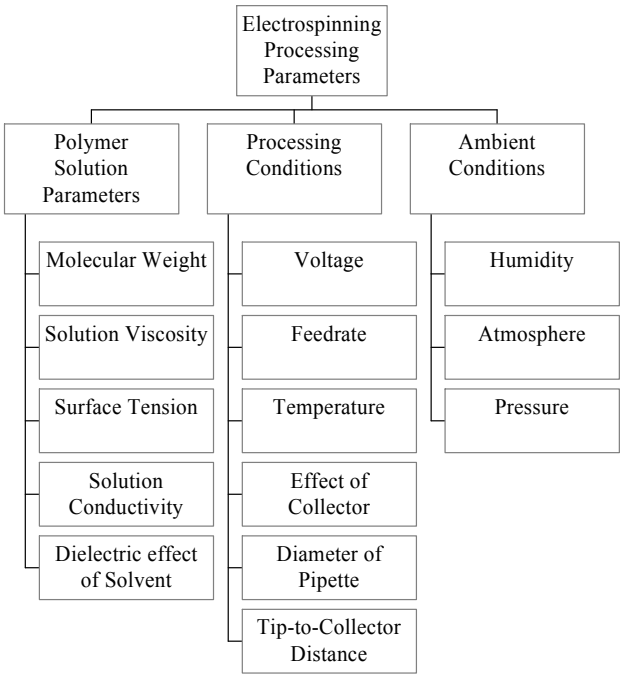

Figure 2.8 *Summary of electrospinning processing parameters*

2.4.1.1 Processing Solution Parameters

The most significant influence on the fiber morphology during electrospinning is caused by the polymer solution. Some of these factors are discussed below.

2.4.1.1.1 Molecular weight and solution viscosity

The molecular weight of a polymer has a tremendous effect on the solution viscosity. A high molecular weight polymer, when dissolved, will lead to a higher viscosity than when a lower molecular weight polymer is dissolved in the same solvent. For electrospinning to be achieved the polymer solution must be of sufficient molecular weight and viscosity. During electrospinning the polymer jet is stretched and it is the entanglements of the moleculer chains that prevent the electrically driven jet from breaking up, therefore maintaining a continuous jet.

As a result of this, monomeric polymer solutions do not form fibers when electrospun[59]. The length of the polymer chain determines the molecular weight, which in turns determines or affects the viscosity. Increasing the solution concentration can also increase the viscosity. A greater concentration will also lead to more entanglements. Table 2.1 below shows the

boundary conditions of polymer concentrations between beaded and uniform fibers for various polymer systems.

Table 2.1
The boundary condition of polymer concentration between uniform and beaded nanofibers[43]

Polymer	Molecular Weight	Solvent	Boundary Condition of Polymer Concentration	Other Spinning Parameters
Poly(ethylene oxide) **PEO** [Fong *et al* (1999)	M_w = 900 000	Water	Uniform Fibers: 3.8 ~ 4.3 wt% Beaded Fibers: 1 ~ 3 wt%	Voltage: 15kV Distance: 21.5cm
Poly(e-caprolactone) **PCL** [Lee *et al* (2003b)]	M_n = 80 000	Dichloromethane or Dimethylformamide (DMF)	Uniform Fibers: 13 wt% Beaded Fibers: 10 wt%	---------
Poly(D,L-lactic acid) **PDLA** [Zhong *et al* (2002)]	---------	Dimethylformamide (DMF)	Uniform Fibers: 35 wt% Beaded Fibers: 20 ~ 30 wt%	Voltage: 20kV Distance: 15cm Feed rate: 1.2ml/h
Poly)p-dioxane-co-L-lactide-block-poly)ethylene glycolide) [Bhattarai *et al* (2003)]	M_w = 42 000	Dichloromethane	Uniform Fibers: 20 wt% Beaded Fibers: 15 wt%	Voltage: 15kV Distance: 11cm
Bombyx mori silk [Sukigara *et al* (2003)]	---------	50% Aqueous Calcium Chloride	Uniform Fibers: 15 ~ 20 wt% Beaded Fibers: 8 ~ 12 wt%	Voltage: 28kV Distance: 7cm
Dextran [Jiang *et al* (2004)]	M_w = 64 000 ~ 76 000	Water	Uniform Fibers: 0.75 ~ 1.0 g/ml Beaded Fibers: 0.5 ~ 0.65 g/ml	Voltage: 25kV Distance: 15cm Feed rate: 1.2ml/h

M_w : Weight-average molecular weight
M_n : Number-average molecular weight

The molecular weight and chain entanglements have a significant effect on whether the jet breaks up into small droplets or whether the electrospun fibers form beads[60]. An excessively high molecular weight can have two disadvantages. The solution may dry at the pipette tip or the viscosity may be too high and the solution will not flow through the pipettes[61, 62].

2.4.1.1.2 Surface Tension

According to Ramahrisha *et al*[43] the initiation of electrospinning requires the charged solution to overcome its surface tension. Surface tension may cause the formation of beaded fibers. Surface tension decreases the surface area per unit mass of a fluid. When there is a high concentration of solvent molecules, there is a greater tendency for them to congregate and take on a spherical shape. This will happen as a result of the surface tension and will lead to the formation of a beaded structure/morphology. At higher viscosities there is a greater interaction between solvent and polymer molecules. Thus when the solution is stretched under

the influence of the charges, the solvent molecules will tend to spread over the entangled molecules of the polymer and therefore reduce the tendency for the solvent molecules to come together under the influence of surface tension to form beaded morphologies. This is shown in Figure 2.9 below.

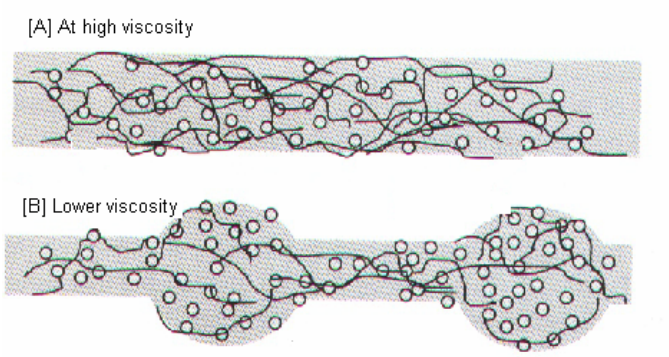

Figure 2.9 *The difference between beaded fibers and smooth fibers due to surface tension*[43]

Ethanol has a low surface tension and can therefore be added to encourage the formation of smooth fibers[63]. Adding surfactant can also reduce the surface tension.

2.4.1.1.3 Solution conductivity

If the conductivity is increased the electrospinning jet can carry more charges. Adding ions to the solution can increase conductivity of the solution. As mentioned before, bead formation will occur if the polymer solution is not stretched sufficiently. Therefore, by adding salt or a polyelectrolyte to the solution, the increased conductivity will tend to increase stretching, leading to the formation of smooth fibers. Increased stretching however will lead to fibers having a smaller diameter[62]. There is, however, a limit to the reduction of the fiber diameter. There will be greater viscoelastic force acting against the Columbic forces of the charges the more the solution is stretched[63].

Solutions prepared using higher conductivity generally yield fibers without beads, while no fibers are formed when the solution is non-conductive[64]. An ionic surfactant such as triethyl benzyl ammonium chloride can also be used and will simultaneously increase conductivity while at the same time reducing surface tension[65]. Table 2.2 below shows the boundary conditions of electrical conductivity between beaded and uniform fibers for different polymer systems.

Table 2.2
The boundary condition of electrical conductivity between uniform and beaded nanofibers[43]

Polymer	Molecular Weight	Solvent	Boundary Condition of Polymer Concentration	Other Spinning Parameters
Poly(ethylene oxide) **PEO** [Fong *et al* (1999)	M_w = 900 000	Water (NaCl addition)	Uniform Fibers: NaCl addition 0.3 ~ 1.5 wt% Solution Resistivity 1.9 ~ 0.462 Wm Beaded Fibers: NaCl addition 0.0015 ~ 0.15 wt% Solution Resistivity 83.4 ~ 3.61 Wm	Polymer Concentration: 3 wt% Voltage: 15kV Distance: 21.5cm
Poly(D,L-lactic acid) **PDLA** [*Zhong et al* (2002)]	---------	Dimethylformamide (DMF) (1 wt% KH_2PO_4 , NaH_2PO_4 and NaCl addition	Uniform Fibers: KH_2PO_4 addition (AFD 1000nm) NaH_2PO_4 (AFD 330nm) NaCl addition (AFD 210nm)	Polymer concentration: 30 wt% Voltage: 20kV Distance: 15cm Feed rate: 1.2ml/h

M_w : Weight-average molecular weight
M_n : Number-average molecular weight

2.4.1.1.4 Dielectric effect of the solvent

In general, a solution with a high dielectric property will have a reduction in bead formation as well as in fiber diameter[66]. A typical solvent that can be added to the solution to increase the dielectric property is DMF (N,N-Dimethylformamide). This also improves the fiber morphology[67].

2.4.1.2 Processing conditions

External factors that have an effect on the electrospinning jet include:

- Voltage supply
- Feedrate
- Temperature of solution
- Type of collector
- Needle/Pipette diameter

- Tip-to-Collector distance

These parameters affect fiber morphology but have a less significant effect when compared to solution parameters.

2.4.1.2.1 Voltage supply

The supplied voltage is a crucial element in electrospinning. The voltage will induce the necessary charges on the solution and together with the electric field will initiate electrospinning when the electrostatic force overcomes the surface tension. Generally a voltage of more than 6kV will induce a Taylor cone during jet initiation[68]. The amount of voltage needed to maintain a stable Taylor cone will be dependent on the feedrate. A too high voltage will cause a greater amount of solution to be drawn into the pipette tip. This will lead to a smaller and less stable Taylor cone[62]. If the drawing of the solution into the pipette tip is too fast, the Taylor cone may recede into the pipette[49].

High voltage leads to greater stretching and a greater electric field. This causes a reduced fiber diameter and encourages faster solvent evaporation. High voltage also has a great tendency to allow the formation of beaded fibers. Furthermore a high voltage affects the crystallinity. The electrostatic field causes more ordered molecules leading to greater crystallinity. However, above a certain voltage crystallinity will decrease[69].

2.4.1.2.2 Feedrate

The volume or amount of solution available at the pipette tip will be determined by the feedrate. A given voltage will determine a given rate for a stable Taylor cone. An increased feedrate will lead to increased fiber diameter or bead formation[62]. A lower feedrate is more desirable as the solvent has more time to evaporate[70].

2.4.1.2.3 Temperature of the solution

The effect of temperature on electrospinning can have an effect in two ways. Firstly on the polymer solution; When solutions are spun at a higher temperature the result is a more uniform diameter[71]. This may be due to an increase in solubility or a lower viscosity of the polymer solution. With lower viscosity the Columbic forces are able to exert greater

stretching of the solution, thus resulting in fibers of smaller diameter[72]. An increase in temperature also increases polymer mobility, which in turn allows the Columbic force to stretch the solution further. On the other hand a temperature increase will also lead to an increase in solvent evaporation while spinning takes place and hence lead to the increase in the viscosity.

2.4.1.2.4 Effect of the collector

For electrospinning to be initiated an electric field must be present. This field is established by making use of a conductive collector plate, usually aluminium foil, which is grounded to ensure a stable potential difference. When using a non-conductive material as the collector plate, charges quickly accumulate on the collector plate which results in fewer fibers being deposited[73]. Fibers will also have a much lower packing density. When using a conductive material, charges on the fibers are dissipated thus allowing more fibers to be attracted to the collector. Fibers therefore pack more closely together[74].

Non-conductive materials may result in the formation of a three dimensional honey comb structure. This is due to charge accumulation and repulsive forces between like charges[62]. However, even conductive collectors have charge accumulation, which may result in the formation of dimples on the fiber mesh. Other factors that influence fiber or fiber mesh morphology concerning the collector plate include:

- Porosity of collector (ex. Paper) - This leads to lower packing density and also influences evaporation rate of the solvent.
- Patterned collectors - This helps varying the texture of the fiber mesh

2.4.1.2.5 Pipette opening dimensions

The internal diameter of the pipette orifice affects the electrospinning process. Mo *et al*[32] found that a smaller internal diameter reduces clogging and reduces the amount of bead formation. The smaller the internal diameter is, the smaller the diameter of the spun fibers will be. Because the droplet that forms at the pipette opening will be smaller with a small diameter pipette, the surface tension will be increased. As a result, the acceleration of the jet decreases and this allows more time for the solution to be stretched and elongated before it is collected. Care should, however, be taken when choosing the diameter of the pipette, as a too small diameter will not allow a droplet of the solution to form at the pipette tip[32].

2.4.1.2.6 Tip to collector distance

The distance between the tip and the collector has an influence on electrospinning properties. Varying the distance between the tip and the collector will have a direct influence on the flight time and the electric field strength. When the distance is too small, there will not be enough time for the solvents to evaporate from the jet. This may cause the fibers to merge causing the formation of junctions in inter and intra layer bonding[59]. This is shown in Figure 10.

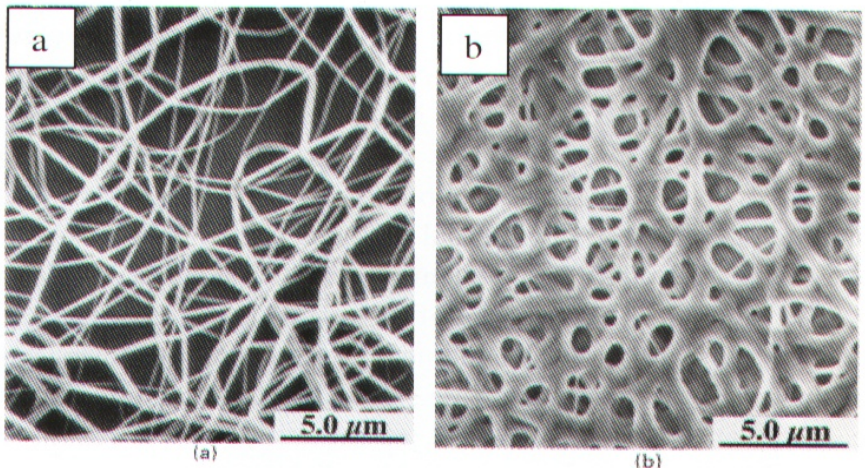

Figure 2.10 *The effect of tip to collector distance on nanofiber morphology Nylon 6,6 at (a) 2cm deposition distance and (b) 0.5cm deposition distance*[49].

Too low a distance also leads to the formation of beads. This is usually due to an increase in field strength between the tip of the pipette and the collector. Increasing the distance will also lead to a decrease in the average fiber diameter[75]. This is because the longer flight time enables the fibers to be stretched for longer periods of time before they are deposited. When the distance is too large no fiber will be deposited on the collector. There is thus an optimal electrostatic field strength below which the stretching of the solution will decrease resulting in increased fiber diameters.

2.4.1.3 Ambient Conditions

2.4.1.3.1 Humidity

If the humidity is high, water may condense on the surface of the spun fibers and by doing so affect the fiber morphology[76]. As water vapour condenses on the surface of the

electrospinning jet, pores are created when both the water and solvent eventually evaporate. Humidity will also determine the rate of solvent evaporation from the solution. For example, at very low humidity, volatile solvents dry very rapidly. The effect of humidity on electrostatic charges on non-conducting surfaces have also been widely studied. At higher relative humidity (>76%) there are usually no charges on the particles. With decreasing humidity, there is usually an increase in the amount of charges[77].

2.4.1.3.2 Type of Atmosphere

Different gasses have different behaviour under high electrostatic field. For example, Helium will break down under high electrostatic fields and electrospinning will not be possible. However, when gasses with higher breakdown voltage are used, such as Freon®-12, the fibers obtained have twice the diameter of those electrospun in air given that all the other conditions are equal[78].

2.4.1.3.3 Pressure

The effect of pressure on the electrospinning jet can be investigated when the process is carried out in an enclosed system. A reduction in pressure usually leads to a decrease in electrospinning efficiency. At very low pressures electrospinning will not be possible due to direct discharge of the electrical charges.

2.5 Surface Modification by Corona Treatment

2.5.1 Definition and Setup

By definition, corona discharge is a gas discharge where the geometry confines the gas ionising process to high field ionisation regions around the active electrodes[79]. The active electrodes determine the corona geometry. Corona treatment often results in an increase of the surface energy and thereby results in better wettability and adhesion. In its most basic form the corona treatment facility can be represented as in Figure 11 below. The geometry of the electrodes may vary from plates, discs, and needles to wire electrodes.

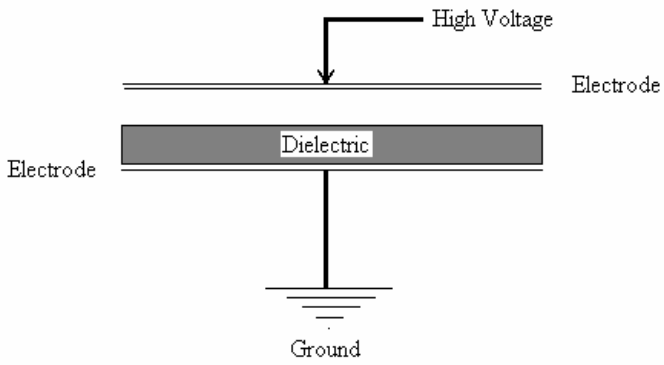

Figure 2.11 *A graphic representation of a basic corona discharge setup*[79].

A high voltage is applied to the top electrode and the bottom electrode usually acts as a ground electrode. A voltage build-up ionizes the air in the air gap, creating a corona, which will increase the surface tension of the substrate passing over the electrically grounded electrode[79].

2.5.2 PDMS treated materials

PDMS shows several interesting characteristics that make it ideal for various applications that include high voltage insulation. These characteristics include low weight, easy installation, good electrical properties, low surface energy and good resistance to withstand contamination through pollutants[80]. Furthermore, PDMS is a very thermally stable material that performs well over a wide range of temperatures

PDMS has the unique property that after its loss of hydrophobicity due to surface modification, the hydrophobic character recovers. Meincken *et al*[81] reported on the unique property of PDMS to recover its hydrophobicity after exposure to corona discharge by making use of the adhesive force determined by AFM force distance measurements. Several other researchers have studied the underlying molecular mechanisms of hydrophobic recovery. Using angle-resolved X-ray Photoelectron Spectroscopy (XPS), Owen and coworkers[82, 83] found that a thin wettable, brittle silica-like layer was formed after corona treatment of PDMS in air. Numerous researchers have identified different mechanisms for hydrophobicity recovery. According to Hillborg *et al*[84] hydrophobic recovery is usually explained as being due to a diffusion of unoxidized low molar mass PDMS through cracks in the silica-like surface layer. Toth *et al*[85] studied silicone rubber surfaces exposed to plasma or corona discharges in air. They found that the diffusion of low molecular weight PDMS played

a larger role towards hydrophobicity recovery than reorientation of polar groups in the bulk of the rubber. Morra *et al*[86] who used a combination of static secondary ion mass spectroscopy, XPS and infra-red spectroscopy on 0^{18} plasma modified PDMS proposed that the hydrophobicity recovery was due to burial of polar groups into the bulk of the polymer and to surface condensation of silanols and consequent crosslinking in the contact angle-probed layer. Hollahan and Scott *et al*[87, 88] have also discussed certain chemical reactions that occur during corona discharge.

Mallon *et al*[89] used positron annihilation spectroscopy to study the effects of corona discharge on high voltage PDMS insulators. This technique is a non-destructive technique for tracking changes in the polymer. They concluded that during the corona treatment of PDMS insulators a silica rich layer of approximately 40nm in thickness formed at the surface of the material. Evidence was also found for the diffusion of low molecular weight components back to the surface, aiding in the hydrophobicity recovery after corona treatment.

2.6 Silicone Elastomers

2.6.1 Strength of silicone elastomers

Silicone elastomers possess unique properties such as good low-temperature flexibility, excellent electrical properties, chemical inertness, water repellency and biocompatibility[90, 91]. Silicone elastomers also possess high reversible deformability that is of great industrial importance. However, initial modulus and durability of these materials are low and without additional reinforcing, are of no practical use. The low strength of unfilled silicone elastomers was initially improved by making use of "white soot" (fumed or pyrogenic silica in 1942) as a reinforcing filler and by incorporation of crosslinkable vinyl groups into the polymer. Carbon black and silica particles have also been used extensively for this purpose[92-95]. Table 2.3 shows the mechanical properties of different silicone elastomers with some sort of reinforcement filler used. It is important to note that unfilled silicone elastomers have even lower mechanical properties than illustrated in table 2.3. One component RTV elastomers, even with reinforcing fillers, exhibit mechanical properties that are so low that they are not usable for application in moulded or extruded articles[96].

Table 2.3

Mechanical properties of silicone elastomers[96]

Property	HV	LSR	RTV-2	RTV-1
Hardness, Shore A	20-90	20-70	0-90	15-25
Tensile Strength, MPa	6-12	6-10	0.5-6	1-3
Tear ASTM 624B, N/mm	10-45	15-40	10-20	3-8

HV : Hot vulcanized rubber
LSR : Liquid silicone rubber
RTV-2 : Two component Room Temperature vulcanized
RTV-1 : One component Room Temperature vulcanized

Table 2.4 shows a comparison between the mechanical strength of silicone elastomers and other rubbery polymers. It can clearly be seen that silicone elastomers possess the lowest tensile strength even when reinforced.

Table 2.4

Properties of typical thermoplastic elastomers relative to other rubbery polymers[97]

Material	Tensile Strength at break (Mpa)	Tensile Strength at break (%)
Styrene-butadiene rubber (reinforced)	15	500
Natural rubber (reinforced)	30	500
Silicone (reinforced)	5	150
Polyethylene	10	High
polyurethane	50	600

2.6.2 Nano-reinforcers and why are they useful

In the unfilled state, PDMS elastomers generally have poor mechanical properties. To improve mechanical properties, elastomeric materials are often compounded with reinforcing fillers. PDMS is traditionally reinforced with silica and the interactions between the two phases are ensured by hydrogen bonds between the silanols on the silica surface and the oxygen atoms of the polymer chains.

Usually filler characteristics determine the effectiveness of a filler. These characteristics include size and shape of the particles and, more significantly, the strength of polymer-filler interactions[98-101].

For the reinforcement to be effective there must be a strong interaction between the matrix and the stiffer phase and this can be achieved using a filler with a large surface-area-to-volume ratio. Optimally this means using small fillers with a large aspect ratio, these include, particles with nanoscale dimensions such as flakes, nanofibers or hollow nanotubes. Reinforcing fillers usually have particle diameters in the range of 10 to 100 nm.

Fillers that are often used may be present in the form of platelets of one to a few nanometers thick to hundreds to thousands of nanometers long. Depending on the polymer-layered silicate interactions, three main types of composites may be obtained when a layered clay is dispersed in a polymeric medium; (1) micro-composite or phase-separated composite, where the layered silicate acts as a conventional filler; (2) intercalated nano-composite, in which one or several polymer chains are inserted between the silicate layers leading to a regular multilayer morphology; or (3) exfoliated or delaminated nano-composite. This is shown in Figure 2.13. The dispersion in the polymer matrix of 1 nm thick layers constitutes the reinforcing phase of the exfoliated structure. This structure is of particular interest because it leads to a large polymer-filler interface and thus to the most dramatic changes in various properties of the resulting material[102-104].

As already mentioned, the aspect ratio (length/width) of the particles are also expected to affect the properties of the final materials. Acicular fillers such as fibers or nanotubes, characterized by two dimensions in the nanometer range, yield materials with exceptional mechanical properties[100].

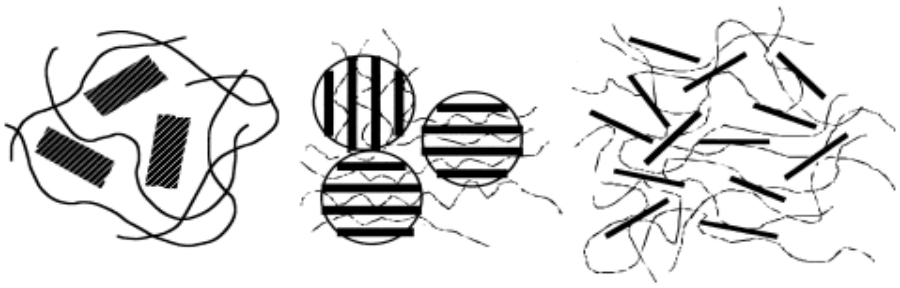

a) Conventional composite b) Intercalated nanocomposite c) Exfoliated nanocomposite.

Figure 2.12 *Schematic representation of the three types of polymer-layered silicate composites*[100].

Frogley *et al*[105] studied the reinforcement effect of single-wall carbon nanotubes or SWNT's and larger carbon nanofibrils on silicone elastomers. Figure 2.13 shows that for both SWNT's

and fibrils, the initial modulus is radically improved as the filler concentration increases. Their experimental evidence suggests that the reinforcement for SWNT and other carbon fillers are due to the high aspect ratio and low density of the nanotube bundles and that well dispersed single nanotubes should provide even better reinforcement.

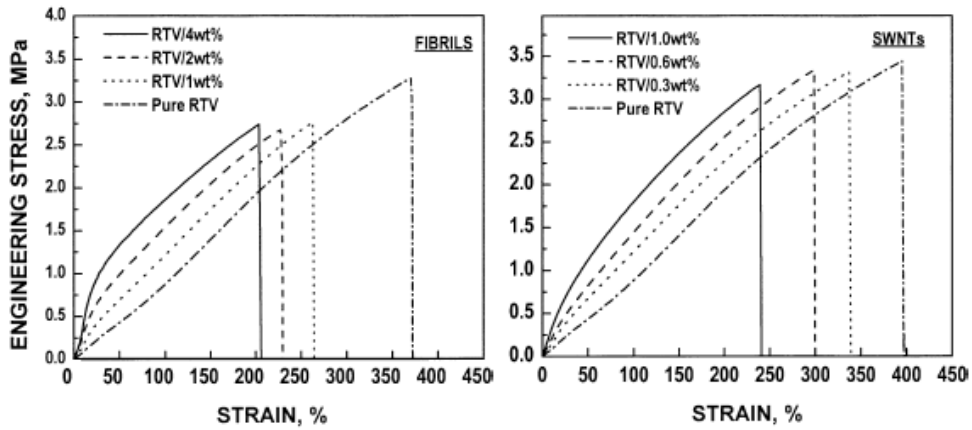

Figure 2.13 *Stress–strain curves for RTV/carbon nanofiber composites. The stress is the engineering stress (applied force divided by the unloaded cross sectional area) and the strain is the true strain*[105].

2.7 References

1. Kickelbick, G., *Hybrid Materials. Synthesis, Characterization and Application*. Wiley-VCH Verlag GmbH & Co: Germany, 2007.
2. Pyun, J.; Matyjaszewski, K. *Chem. Mater.* **2001,** 13, 3436-3448.
3. Ma, M.; Hill, R. M.; Lowery, J. L.; Fridrikh, S. V.; Rutledge, G. C. *Langmuir* **2005,** 21, 5549-5554.
4. Li, Z.; Han, W.; Kozodaev, A.; Brokken-Zijp, J. C. M.; de With, G.; Thune, P. C. *Polymer* **2006,** 47, 1150-1158.
5. Huang, H.-H.; B. Orler, B.; Wilkes, G. L. *Macromolecules* **1987,** 20, 1322.
6. Mackenzie, D.; Huang, Q.; Iwamoto, T. *J Sol–Gel Sci Technol* **1996,** 7, 151.
7. Guermeur, C.; Lambard, J.; Gerard, J.-F.; Sanchez, C. *J Mater Chem* **1999,** 9, 769.
8. Martos, C.; Fubio, F.; Rubio, J.; Oteo, J. L. *J Sol–Gel Sci Technol* **2001,** 20, 197.
9. J.T. Han; D.H. Lee; C.Y. Ryu; K. Cho. *J Am Chem Soc* **2004,** 126, 4796.
10. Shinoda, H.; Matyjaszewski, K. *Macromolecules* **2001,** 36, 4772-4778.
11. Shinoda, H.; Miller, P. J.; Matyjaszewski, K. *Macromolecules* **2001,** 34, 3186-3194.
12. Shinoda, H.; Matyjaszewski, K. *Rapid Commun.* **2001,** 22, 1176.
13. Knauss, D. M.; Tianzi, H. *Polymer Preprints, American Chemical Society* **2001**, (42), 193-202.
14. Minglin, M.; Randal M.H. *Curr. Opin. Colloid Interface Sci.* **2006**, (11), 193-202.
15. Wagner, T.; Neinhuis, C.; Barthlott, W. *Acta Zool* **1996,** 77, 213-225.
16. Neinhuis, C.; Barthlott, W. *Ann. Bot.* **1997,** 79, 667-669.
17. Jung, Y. C.; Bhushan, B. *Nanotechnol.* **2006,** 17, 4970-4980.
18. de Gennes, P. G. *Rev. Mod. Phys.* **1985,** 57, 827-863.
19. Callies, M.; Que´re´, D. *Soft Matter* **2005**.
20. Lafuma, A.; Que´re´, D. *Natural Materials* **2003,** 2, 457-460.
21. Blossey, R. *Natural Materials* **2003,** 2, 301.306.
22. Onda, T.; Shibuichi, S.; Satoh, N.; Tsujii, K. *Langmuir* **1996,** 12, 2125-2127.
23. Zhang, J. L.; Li, J. A.; Han, Y. C. *Macromol. Rapid Commun.* **2004,** 25, 1105-1108.
24. Shiu, J. Y.; Kuo, C. W. In Proceedings of SPIE - The International Society of Optical Engineering, 2005; 2005; pp 325-332.
25. Jin, M. H.; Feng, X. J.; Xi, J. M.; Zhai, J.; Cho, K. W. *Macromol. Rapid. Commun.* **2005,** 26, 1805-1809.
26. Teshima, K.; Sugimura, H.; Inoue, Y.; Takai, O.; Takano, A. *Appl. Surf. Sci.* **2005,** 244, 619-622.

27. Yabu, H.; Shimomura, M. *Chem. Mater.* **2005,** 17, 5231-5234.
28. Shi, F.; Wang, Z. Q.; Zhang, X. *Adv. Mater.* **2005,** 17, 1005-1009.
29. Xu, L.; Chen, W.; Mulchandani A; Yan, Y. *Angew. Chem. Int.* **2005**, 6009-6012.
30. Yabu, H.; Shimonura, M. *Chem. Mater.* **2005,** 17, 5231-5234.
31. Khorasani, M. T.; Mirzadeh, H.; Kermani, Z. *Appl. Surf. Sci.* **2005,** 242, 339-345.
32. Zhao, S. L.; Wu, X. H.; Wang, L. G.; Huang, Y. *J. Appl. Polym. Sci* **2004,** 91, 242-246.
33. Hadjichristidis, N.; Pitsokalis, M.; Pispas, A.; Iatrou, H. *Chem . Rev.* **2001,** 101, 3747-3792.
34. Pitsokalis, M.; Pispas, A.; Hadjichristidis, N.; Mays, J. W. *Adv. Polym. Sci.* **1998,** 135.
35. Hadjichristidis, N.; Xenidou, M. *Macromolecules* **1998,** 31, 5690.
36. Kowalczuk, M.; Adamus, G.; Jedlinksi, Z. *Macromolecules* **1994,** 27, 572.
37. Lee, C. L.; Frye, C. L.; Johansson, O. K. *Polym. Prepr.* **1969,** 10, 1361.
38. Frye, C. L.; Salinger, R. M.; Fearon, F. W. G.; Klosowski, J. M.; DeYoung, T. J. *Org. Chem.* **1970,** 35, 1308-1314.
39. Meijs, G.; Rizzardo, E. *Rev. Macromol. Chem. Phys.* **1990,** 305, (C30).
40. Belu, A. M.; DeSimone, J. M.; Linton, R. W.; Lange, G. W.; Friedman, R. M. *Am. Soc. Mass Spectrom.* **1996,** 7, 11-24.
41. Elkins, C. L.; Long, T. E. *Macromolecules* **2004,** 37, 6657-6659.
42. Schunk, T. C.; Long, T. E. *J. Chrom.* **1995,** 692, 221-232.
43. Ramahrisha, S.; Fujihara, K.; Teo, K. E.; Lim, T. C.; Ma, Z., *An introduction to Electrospinning and Nanofibers*. World Scientific Publishing Co. Pte. Ltd.: Singapore, 2005.
44. Ondarcuhu, T.; Joachim, C. *Europhys. Lett.* **1998,** 42, (2), 215-220.
45. Feng, L.; Li, S.; Li, H.; Zhai, J.; Song, Y.; Jaing, L. *Angew Chem Int Ed* **2002,** 41, (7), 1221-1223.
46. Martin, C. R. *Chem. Mater.* **1996,** 8, 1739-1746.
47. Ma, P. X.; Zhang, R. *J. Biomed. Mat. Res.* **1999,** 46, 60-72.
48. Liu, G. J.; Ding, J. F.; Qiao, L. J.; Gua, H.; Dymov, B. P.; Gleeson, J. T. *Chem-A European J* **1999,** 5, 2740-2749.
49. Deitzel, J. M.; Kleinmeyer, J. D.; Hirvonen, J. K. *Polymer* **2001,** 42, 8163-8170.
50. Formhals, A. *US Patent* **1934,** 1,975,504.
51. Formhals, A. *US Patent* **1939,** 2,160,962.
52. Formhals, A. *US Patent* **1940,** 2,187,302.
53. Formhals, A. *US Patent* **1943,** 2,323,025.

54. Formhals, A. *US Patent* **1944,** 2,349,950.
55. Larrondo, L.; Marley, R. S. J. *Poly. Sci. Pol. Phys* **1981a,** 19, 909-920.
56. Larrondo, L.; Marley, R. S. J. *Poly. Sci. Pol. Phys.* **1981b,** 19, 921-932.
57. Larrondo, L.; Marley, R. S. J. *Poly. Sci. Pol. Phys.* **1981c,** 19, (933-940).
58. Lyons, J.; Li, C.; Ko, F. *Polymer* **2004,** 45, 7595-7603.
59. Buchko, C. J.; Shen, Y.; Martin, D. C.; Chen, L. C. *Polymer* **1999,** 40 7397–7407.
60. Shenoy, S. L.; Bates, W. D.; Frisch, H. L.; Wnek, G. E. *Polymer* **2005,** 46, 3372–3384.
61. Kameoka, J.; Orth, R.; Yang, Y.; Czaplewski, D.; Mathers, R.; Caotes, G.; Cgraighead, H. G. *Nanotech.* **2003,** 14, 1124-1129.
62. Zhong, X. H.; Kim, K. S.; Fang, D. F.; Ran, S. F.; Hsiao, B. S.; Chu, B. *Polymer* **2002,** 43, 4403-4412.
63. Choi, J. S.; Lee, S. W.; Jeong, L.; Bae, S. H.; Min, B. C.; Youk, J. H.; Park, W. H. *Int. J. Biol. Macromol.* **2004,** 34, (4249-256).
64. Jarasawannapoom, T.; Hongrojjanawiwat, W.; Jitjaicham, S.; Wannatong, L.; Nithitanakul, M.; Pattanaprom, C.; Koombhongse, P.; Rangkupan, R.; Supaphol, P. *Euro. Polym.* **2005,** 41, 409-421.
65. Lin, T.; Wang, H. X.; Wang, H. M.; Wang, X. G. *Nanotech.* **2004,** 15, 1375-1381.
66. Son, W. K.; Youk, J. H.; Lee, T. H.; Park, W. H. *Polymer* **2004a,** 45, 2959-2966.
67. Lee, K. H.; Kim, H. Y.; Lee, D. R. *Polymer* **2003b,** 44, 1287-1294.
68. Taylor, G. *Proc. R. Soc. Lond. A* **1964,** 280, 383-397.
69. Deitzel, J. M.; Kleinmeyer, J.; Harris, D. *Polymer* **2001,** 42, 261-272.
70. Yuan, X.; Zhang, Y.; Dong, C.; Sheng, J. *Polym. Int. In Press* **2005**.
71. Demir, M. M.; Yilgor, I.; Yilgor, E.; Erman, B. *Polymer* **2002,** 43, 3303-3309.
72. Mit-upputhum, C.; Nithitanakul, M.; Supapol, P. *Macromol. Chem. Physic* **2004,** 205, 2327-2338.
73. Kessick R; G, T. *Appl Phys Lett* **2004,** 84, (23), 4807-4909.
74. Liu, H. Q.; Hsieh, Y. L. *J. Polymer. Sci. Pol. Phys.* **2002,** 40, 2119-2129.
75. Ayutsede, J.; Gandhi, M.; Sukigara, S.; Micklus, M.; Chen, H. E.; Ko, F. *Polymer* **2005,** 46, 1625–1634.
76. Megelski, S.; Stephens, J. S.; Chase, D. B.; Rabolt J.F. *Macromolecules* **2002,** 35, 8456-8466.
77. Nieh, S.; Nguyen, T. *J. Electrostat.* **1988,** 21, 99-114.
78. Baumgarten, P. K. *J. Colloid Interf. Sci.* **1971,** 36, 75-79.

79. Markgraf, D. A. In *Corona Treatment: An Overview*, Coextrusion Conference Proceedings, Atlanta, 1984; Enercon Industries Corporation: Atlanta, 1984; p 85.
80. Kikuchi, T.; Nishimura, S.; Nagao, M.; Izumi, K.; Kubota, Y.; Sakata, M. *IEEE Trans. Elect. Insul.* **1999,** 6, 548-556.
81. Meincken, M.; Berhane, T. A.; Mallon, P. E. *Polymer* **2005,** 46, 203-208.
82. Owen, M. J.; Gentle, M.; Orbeck, T.; Williams, D. E., *Polymer Surface Dynamics*. Plenum Press: New York, 1988.
83. Smith, P.; Owen, M. J. *J. Conf. Electr. lnsul. Diel. Phen.* **1992**, 829.
84. Hillbong, H.; Gedde, U. W. *Polymer* **1997,** 39, (10), 1991-1998.
85. Toth, A.; Bertoti, I.; Blazso, M.; Banhegyi, G.; Bognar, A.; Szaplonczay, X. *Appl. Polym. Sci* **1994,** 52, 1293.
86. Morra, M.; Occhiello, E.; Marola, R.; Garbassi, F.; Humphrey, P.; Johnson, D. *J. Coll. Int. Sci.* **1990,** 11, 137.
87. Hollahan, J. R. *J. Appl. Polym. Sci.* **1970,** 14, 2499.
88. Scott, R.; Gaboury, S. R.; Urban, M. W., *Structure Property Relations in Polymers*. American Chemical Society: Washington, DC,, 1993.
89. Mallon, P. E.; Greyling, C. J.; Vosloo, W.; Jean, Y. C. *Rad. Phys. and Chem.* **2003** 68, 453–456.
90. Noshav, A.; McGrath, J. E., *Block Copolymers Overview and Criteria Survey. Academic*. New York, 1977.
91. Warrick, E. L.; Pierce, O. R.; Polmanteer, K. E.; Saam, J. C. *Rubber Chem. Technol.* **1979,** 52, 437.
92. Guth, E. *J. Appl. Phys.* **1944**, 16-20.
93. Kurian, T.; De, P. P.; Khastgir, D.; Tripathy, D. K.; De, S. K.; Peiffer, D. G. *Polymer* **1995,** 36, 3875.
94. Yatsuyanagi, F.; Suzuki, N.; Ito, M.; Kaidou, H. *Polymer* **2001,** 42, 9523.
95. Alberola, N. D.; Benzarti, K.; Bas, C.; Bomal, Y. *Polym. Comp. Sci. Technol.* **2001,** 22, 312.
96. *Ullmann's Encyclopedia of Industrial Chemistry*. 7th ed.; John Wiley & Sons, Inc.: 2007.
97. Mark, J. E.; Erman, B.; Eirich, F. R., *Science and technology of rubber*. 2nd ed.; Academic press, Inc.: Sab Diego, 1994.
98. Bokobza, L. *Macromol. Symp.* **2001,** 169, 243.
99. Bokobza, L. *Macromol. Symp.* **2001,** 171, 163.
100. Bokobza, L. *J. Appl. Polym. Sci.* **2004,** 93, 2095-2104.

101. Bokobza, L.; Rapoport, O. *J Appl Polym Sci* **2002,** 85, 2301.

102. Pinnavaia, T. J.; Lan, T.; Wang, Z.; Shi, H.; Kaviratna, P. D. In *Nanotechnology: Molecularly Designed Materials*, ACS Symposium Series 622, Washingtom, 1996; Chow, G.-M.; Gonsalves, K. E., Eds. American Chemical Society: Washingtom, 1996; p 250.

103. Alexandre, M.; Dubois, P. *Mater. Sci. Eng.* **2000,** 28, 1.

104. Biswas, M.; Sinha, R. *S. Adv. Polym. Sci.* **2001,** 155, 167.

105. Frogley, M. D.; Ravich, D.; Wagner, H. D. *Comp. Sci. Technol.* **2003,** 63, 1647-1654.

Experimental

This chapter gives an overview of the materials and equipment used during the synthesis and characterization of the organic-inorganic hybrid polymers. It further discusses the preparation of chemicals for the polymerization and subsequent analysis as well as the method of synthesizing the hybrid polymer.

3.1. Synthesis of Organic-Inorganic Hybrid Copolymer

3.1.1. Apparatus

The polymer was synthesized using conventional free radical polymerization and therefore did not require an extensive setup. The apparatus thus used consisted out of a heating mantel equipped with a magnetic stirrer and temperature control probe. The reaction vessel was simply a round-bottom flask sealed with a rubber septum.

3.1.2. Raw Materials

The raw materials, except for MMA (as discussed in section 3.2.3), were used as received from the supplier. With the exception of AIBN, all materials were of high grade.

- Monomethacryloxypropyl Terminated polydimethylsiloxane — GELEST, INC (Morrisville, USA)
- Methyl methacrylate monomer — Plascon (South Africa)
- Tetrahydrofurane — Sigma-Aldrich (Johannesburg, South Africa)
- Hexane — Sigma-Aldrich (Johannesburg, South Africa)
- Acetonitrile — Sigma-Aldrich (Johannesburg, South Africa)
- N,N Dimethylformamide — Burdick & Jackson (Muskegon, USA)
- Ethanol — Sigma-Aldrich (Johannesburg, South Africa)

HPLC (High Performance Liquid Chromatography) mobile phases were prepared using HPLC grade (Chromasolv) ethanol, cyclohexane and THF supplied by Sigma-Aldrich, South Africa. All other solvents such as toluene, methanol and chloroform were of analytical grade.

3.1.3. Purification of Monomers

MMA monomer was purified using conventional distillation. MMA was washed using 1:1 volume ratio KOH (0.3M) to remove any inhibitor present and then separated using a separation funnel. Thereafter it was decanted into a round-bottom flask containing glass beads and connected to a condenser and fraction collector and left to distill at 41^{o}C under vacuum using a water aspirator. This helped to prevent thermal auto-polymerization of the MMA monomer. The MMA monomer was then left to cool to room temperature before it was used for polymerization. The first 10ml fraction was discarded to ensure the purity of the MMA

used in the end. The distilled monomer was used directly after purification. A diagram of the setup is shown in the Figure below.

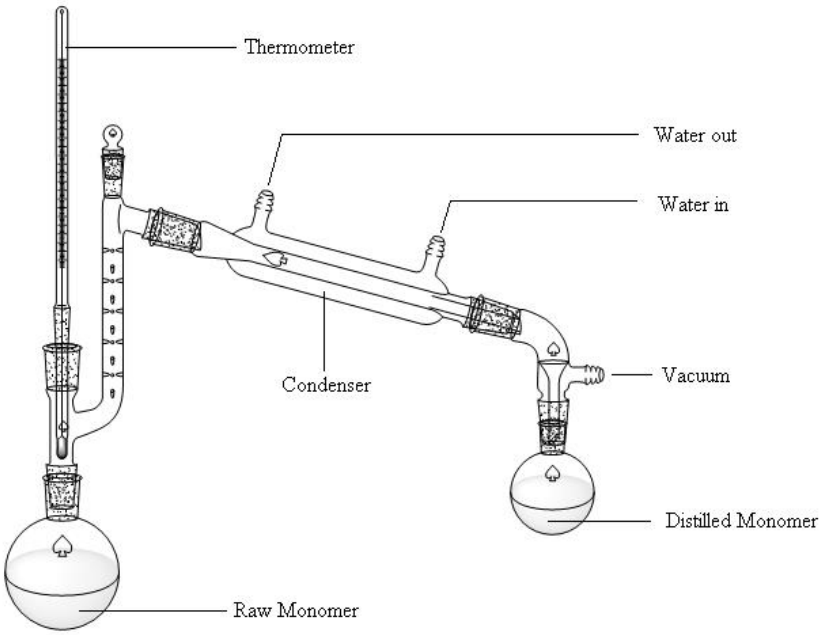

Figure 3.1 *Distillation setup used for purifying monomer*

3.1.4. Polymerization

The free radical copolymerizations of varying amounts of isopropyl terminated monomethacryloxy poly(dimethylsiloxane) macromonomer with MMA were performed in degassed toluene at 70^{o}C for 42 hours using 0.1 wt% (based on MMA) azobis(isobutyronitrile) (AIBN) as initiator. The copolymerizations were carried out at 20 wt% solids (based on MMA). The PMMA-g-PDMS polymer was then precipitated in Methanol and the isolated copolymer was then extracted with n-hexane to remove excess PDMS macromonomer. It was then dried under vacuum at 40^{o}C.

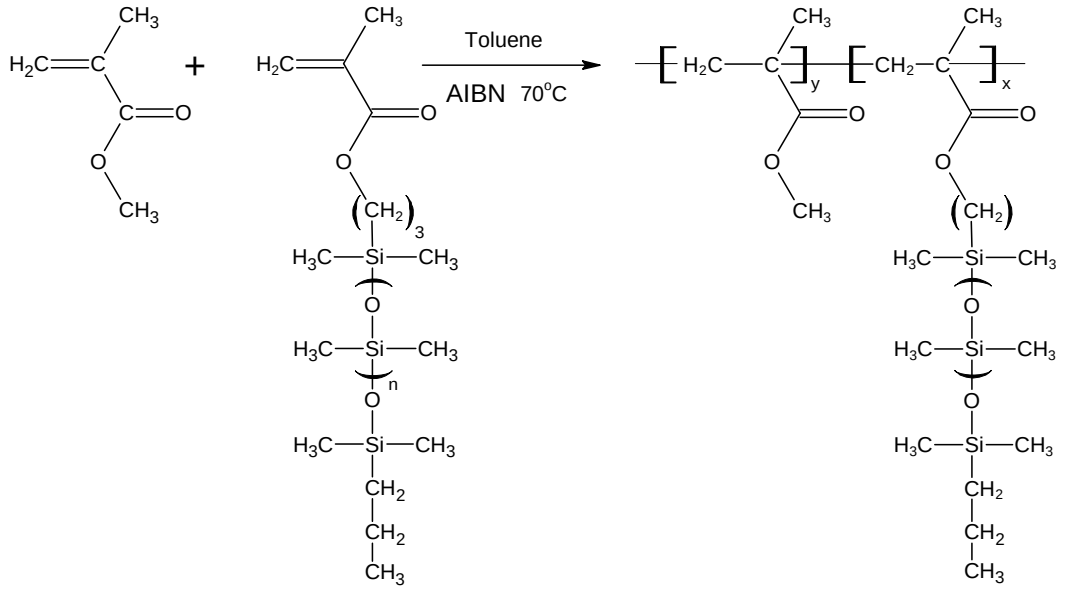

Scheme 3.1 *Scheme showing the reaction of MMA with PDMS macromonomer to give the graft copolymer*

3.1.5. Extraction of Unreacted Macromonomer

Unreacted PDMS macromonomer was extracted by placing the polymer in excess n-hexane. The solution was stirred for 4 hours. The polymer was then filtered using a water aspirator and left to dry over night. To ensure that all solvents evaporated the polymer was then placed in a vacuum oven to dry for a further 12 hours.

3.2. Electrospinning

3.2.1. Apparatus

A 25 kV, 400 micro Amps (10 Watt) output high voltage supply was used for the electrospinning process. The solution reservoirs consisted out of syringes and glass pipettes.

3.2.2. Solution Preparation

Different solution concentrations were used throughout the study. The polymer was dissolved in a bulk solution consisting out of 40% chloroform and 60% dimethylformamide (DMF). The polymer was left to dissolve for 24 hours.

3.2.3. General Electrospinning Setup and Procedure

The electrospinning setup consists of a high voltage supply between two electrodes (one of which acts as a grounded electrode) and a polymer reservoir. The polymer solution was placed in a glass pipette (that acted as the reservoir) and gravity-fed through the tip. All samples were spun using a pipette with a capillary tip opening of approximately 0.5mm. A copper wire electrode was inserted into the solution and a grounded electrode was attached to an aluminium foil pan filled with water, which acted as the collector plate. The supplied voltage is a crucial element in electrospinning. The voltage will induce the necessary charges in the solution and together with the electric field will initiate electrospinning when the electrostatic force overcomes the surface tension[1]. A voltage range of between 8kV to 25kV was applied to electrospin a range of different samples. Other factors influencing the morphology and characteristics of the resultant nanofibers that were varied included: Tip-to-Collector distance, concentration and type of collector.

Another crucial factor influencing electrospinning is the field created as a result of the high applied voltage. Any conducting materials (such as stands, clamps, lab-jacks, etc.) used during spinning influences the electromagnetic field and hence the morphology of the produced nanofibers. Furthermore, these conductors build up static electricity that can be very dangerous. For this reason great care was taken to ensure safety and non-conductors were used as far as possible. PVC piping was used to build a rig to hold the glass pipette that acted as a solution reservoir and polystyrene was used to insulate all other conducting materials.

3.2.4. Collection of Electrospun Nanofiber Mats

As stated above, the nanofibers were spun onto a grounded aluminium pan filled with water. Due to the hydrophobic nature of the hybrid polymer it was easy to lift the entire non-woven nanofiber mat as a whole off the water. The mat was then left to dry for 12 hours to ensure that all solvent traces were removed. It was then cut to size and stored for further analysis.

3.3. Surface Modification via High Voltage Corona Discharge

Corona modification was done using a BD-20C laboratory corona discharger, supplied by Electro-Technic Products. The discharge unit was fitted with a needle for treatment,

electrospun samples were exposed to high voltage corona discharge. The tip of the needle was placed approximately 10mm from the surface of the sample. Samples were treated for varying times from as short as 1min to 60+ minutes. The resultant effects on surface morphology, crosslink density and hydrophobic character were analyzed thereafter.

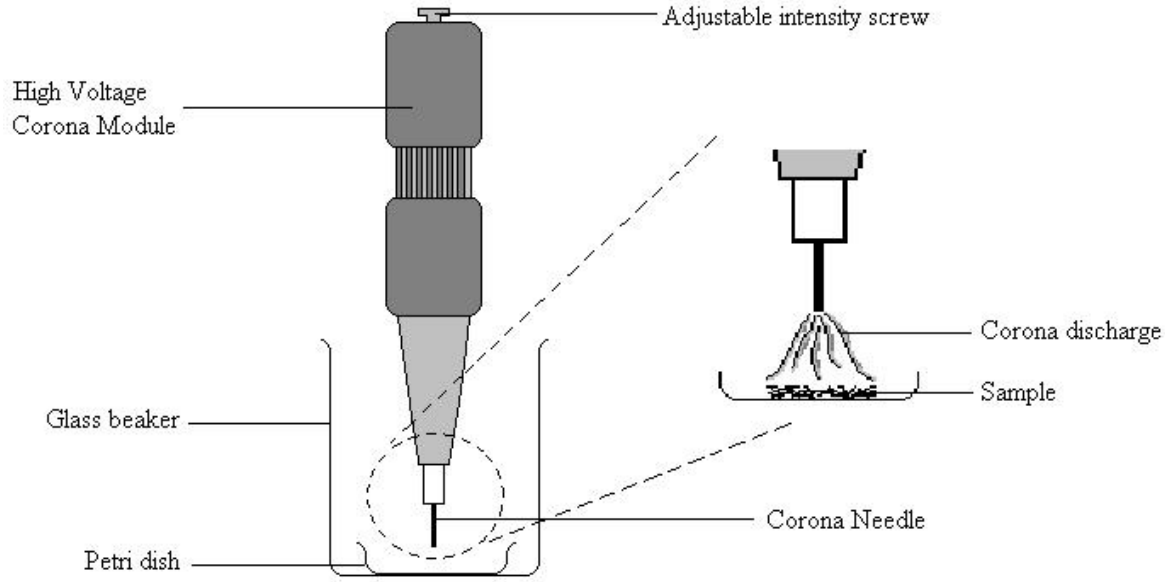

Figure 3.2 *Corona treatment setup*

3.4 Characterization

3.4.1. Scanning Electron Microscopy (SEM)

SEM analyses were performed on a Leo 1430VP Scanning Electron Microscope fitted with a backscatter, cathodoluminescence, variable pressure and energy dispersive detectors, as well as a Link EDS system and software for microanalysis and qualitative work. The SEM system was designed to do high-resolution imaging and quantitative analysis. The system had an error range of 0.5 to 0.2wt% on the major elements.

3.4.2. Transmission Electron Microscopy (TEM)

A JEOL CX200 transmission electron microscope at an accelerating voltage of 200 kV was used. Nanofibers were carefully selected and sandwiched between two TEM grids. TEM was used to obtain high-resolution images for quantitative analysis. Images were obtained to a resolution of 0.86nm.

3.4.3. Nuclear Magnetic Resonance

A Varian VXR 300MHz and Varian *Unity* Inova 600MHz NMR Spectrometer was used to do polymer characterization. The 600 MHz instrument is equipped with three channels, Z gradients, and the following probes:

5mm 1H{15N-31P} indirect detection PFG
5mm 15N-31P broadband
5mm 1H{13C/15N} triple resonance PFG
10mm 103Rh-15N broadband
10mm 15N-31P broadband

Whereas the 300MHz instrument is equipped with two channels and the following probes:

5mm 1H/19F/13C/31P four-nucleus
5mm 15N-31P broadband

3.4.4. SEC-Coupled to FTIR using a LC-Transform

The LC transform technique works on the principle that separation is first achieved according to molecular mass or chemical composition (depending on the mode of operation of the chromatograph). All fractions are then deposited on a germanium disk. The germanium disk was then inserted into a FTIR spectrometer and the FTIR spectra at each point in the elution profile ware obtained. This allows the chemical composition to be determined at each point.

The technique worked as follows and is illustrated in Figure 3.3.

Firstly the polymer solution ($5mg.ml^{-1}$ in THF) is injected into the HPLC and undergoes separation via SEC. The fractionated sample then enters the LC transform unit. The LC transform consists out of a sealed chamber that can be put under vacuum. A heated nebulizing nozzle and a rotating heated stage whereupon the germanium disc, which collects the polymer fractions, is placed.

The polymer exits' the nozzle in the form of a spray. Heating the nozzle helps the THF mobile solvent to evaporate. The heated stage ensures that any residual solvent evaporates.

Because the chamber is under vacuum, the evaporated solvent can leave the chamber and is collected in a liquid nitrogen trap. Only the dry polymer is therefore left behind and deposited on the germanium disc. The stage can be rotated at various speeds (5^o to 20^o per minute) and the polymer is deposited along the edge of the disc in a thin track.

The disc containing the separated fractions is then removed and placed in the IR spectrometer. In side the IR spectrometer the stage can be rotated at the same speed that was used in the LC transform. This allows the accumulation of individual spectra of each collected fraction (as can be seen in the so called waterfall plot in Figure 3.3). This data can then be used to draw up Gram Schmidt plots and chemigrams which provide valuable data concerning the chemical composition of each fraction. A Lab-Connections 303 LC transform and a Perkin Elmer FTIR Spectrometer Paragon 1000 with Perkin Elmer Time-Base and Spectra software was used for analysis. The conditions used in the LC transform step were as follows:

- Nozzle temperature: 32^oC
- Rotating stage: 85^oC
- Vacuum: 7-16 Torr

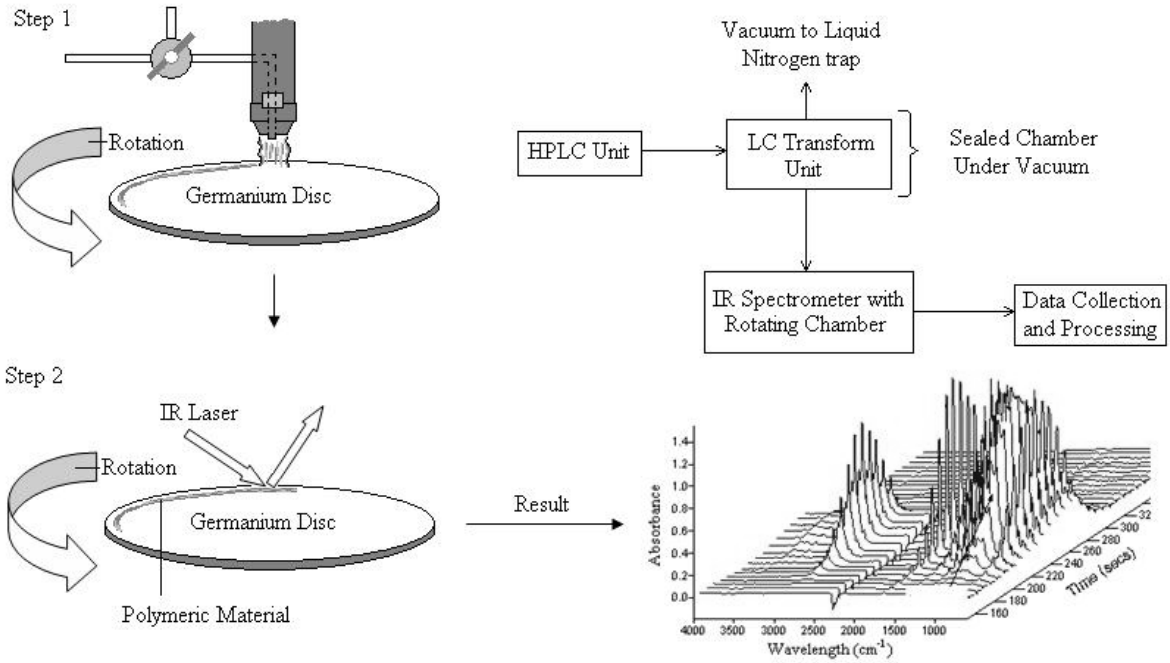

Figure 3.3 *Procedure used during SEC coupled LC Transform FTIR*

3.4.5. Photo Acoustic Spectroscopy

In this technique a modulated radiation is absorbed by the sample. This causes periodic temperature fluctuations within the optical absorption depth. This enables periodic heat transfer to an ambient gas. The PAS signal is a result of the periodic pressure fluctuations in the gas that are associated with the temperature modulation produced by the heat coming from the sample. A Fourier transform infrared spectrophotometer (Perkin Elmer) with photo-acoustic cell (MTec) was used for these studies

3.4.6. Attenuated Total Reflectance Spectroscopy

A Nexus FT-IR (provided by Nicolet Thermo) equipped with a FTIR gas analyzer was used for ATR studies. The spectrometer was fitted with a diamond crystal and measurements were taken in the 600 to 4000cm^{-1} infrared range at a resolution of 4cm^{-1}. Spectra were based on a total of 32 scans per sample.

3.4.7. Static Contact Angle Measurements

For the contact angle measurements a Nikon SMZ-2T light microscope with a 6V, 20W lamp was used. Real time images were taken that were subsequently analyzed to obtain the contact angle. Images were analyzed using Able Image Analyzer™ version 3.6.

Contact angles are used to determine the hydrophobicity or hydrophylicity of the electrospun nanofibers. This was done by placing 1µl water drops on the surface of the material and using a real time Nikon SMZ-2T light microscope still images were taken of the water drops on the surface. These images were analyzed using computer software and the contact angle was determined as follows.

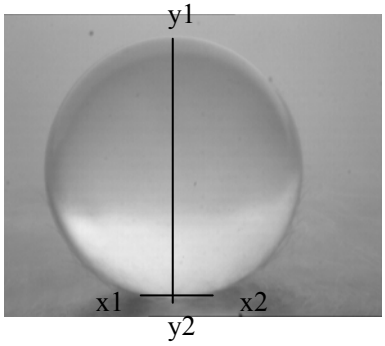

- The contact angle can be classified as the angle tangent line and the solid surface when drawing a tangent line from the drop to the solid surface, therefore,
- Four points were taken, x_1, x_2, y_1, y_2 as can be seen when looking at Figure 2.1.

- These points were used to determine Δx and Δy

The contact angle was then calculated with the following equation:

$$\tan\theta = 2\frac{\Delta y}{\Delta x}$$

Where θ is the contact angle. The mean of ten drops were taken in each case to establish the average contact angle.

3.4.8. Gradient Elution High Performance Liquid Chromatography

Gradient elution studies are well known in literature[2, 3]. By varying the composition of the mobile phase, this technique allows for the separation of graft- or block copolymers from their respective homopolymers.

For the HPLC studies a Waters 2690 Separation Module "Alliance" was used, fitted with a Waters 2487 Dual Wavelength Absorption Detector and a Polymer Laboratories PL-ELS 1000 Evaporative Light Scattering Detector (ELSD) with heated transfer line. Chromatograms were recorded and analyzed using Peak Simple Software (PSS). The system was also equipped with a K5 Column Oven, a Kontron HPLC 560 Autosampler, Kontron Biotek 522 Dual Solvent Pump and a Kontron 3493 Degasser

The flow rate for the mobile phase was kept constant at 1ml.min^{-1}. The composition of the mobile phase, the rate at which the mobile phase was changed as well as other parameters concerning the HPLC gradient profile is discussed in Chapter 4 in Section 4.1.4 under "*Development of HPLC Gradient Profile"*.

3.4.9. Confocal Raman Spectroscopy

Confocal Raman studies were done at the Royal Institute of Technology (KTH), Sweden. A high resolution Raman instrument, LabRAM HR-UV from Jobin Yvon, was used. It was equipped with three lasers (244nm, 514nm and 785nm). This allowed the measurement of Raman scattering in the UV, Visual and NIR range. Integrated in the instrument is an Olympus microscope equipped with a motorized xy-stage. On the xy-stage a

tensile/compression stage or a vertical three-point bending stage can be mounted

3.4.10. Determination of Crosslink Density

Electrospun nanofibers treated with high voltage corona discharge were placed in THF in a concentration of 5mg.ml^{-1}. They were allowed to swell and reach equilibrium at room temperature for approximately 24h. Thereafter the samples were removed from the THF solvent and weighed to determine its mass in the swollen state. It was then let to dry in a fume hood for 24h and then placed in a vacuum oven for an additional 2h to remove any residual solvent left. The mass of the dry sample was then determined. The following equation was used to determine the volume fraction in the swollen state at equilibrium, V_r:

$$V_r = \frac{m_r p_r^{-1}}{m_r p_r^{-1} + m_s p_s^{-1}}$$

Where m_r is the residual mass (in grams) of the polymer after deswelling,

m_s is the solvent mass (in grams) at equilibrium swelling,

p_r is the density of PMMA-g-PDMS,

p_s is the density of THF

The crosslink densities were then calculated with the aid of the Flory-Rehner equation:

$$\frac{1}{M_c} = \frac{\left\{\ln(1 - V_r) + \chi V_r^2 + V_r\right\}}{p_r V_{m,s}\left(V_r^{\frac{1}{3}} - \frac{V_r}{2}\right)}$$

Where M_c is the average molecular mass of the network chains between adjacent crosslinks (g.mol^{-1})

χ is the solvent interaction parameter

$V_{m,s}$ is the molar volume of THF

3.4.11. Slow Positron Beam

Positron analysis allows depth profiling of the polymer sample, which in turn can be used to track changes as a function of depth from the surface[4-7]. In Doppler Broadening of Energy Spectra (DBES) the momentum distribution around the 511keV energy peak is used.

The principle of the method relies on the fact that positrons can become localized in free volume regions and the emission of gamma rays (formed during annihilation) can escape the system without any interaction. These gamma rays contain information about the environment around the site where annihilation took place[8]. The most common source of positrons emitted in the process is ^{22}Na, which contain a maximum energy of 0.54MeV. This enables sufficient penetration depth to probe the bulk of the sample. Positrons slow down, thermilize in the solid (within picoseconds) and diffuse around the lattice, whereupon the positrons annihilate with electrons and form two gamma quanta of equal energies (511keV). The two quanta are emitted in approximately opposite directions. The deviation from 180° is caused by the momentum of the electron, since the momentum of the positron is negligible due to thermalization[9]. This allows detailed analyses of the polymer bulk and surface. In this study the positron beam results are reported in the form of the S parameter (also known as the defect parameter). The S parameter is calculated from the Doppler broadening energy spectra. Figure 3.4 below explains how the S parameter is calculated. The S parameter can be defined as the ratio of the central area to the total area of the annihilation peak after backwards subtraction.

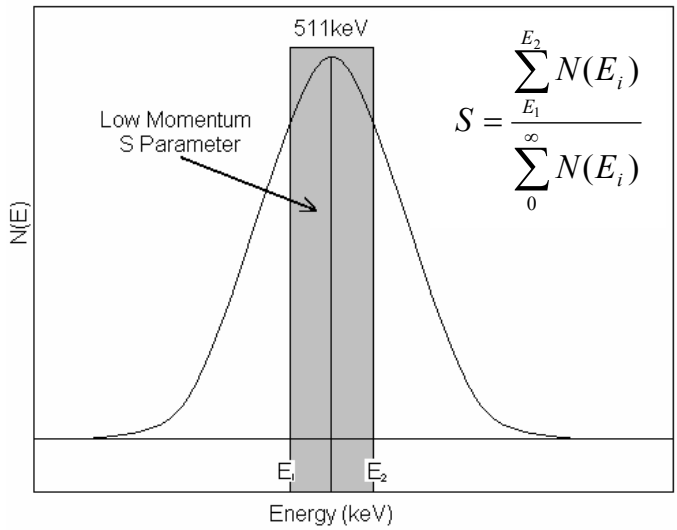

Figure 3.4 *Illustration of the Doppler broadening energy distribution of annihilation radiation and the definition of the S parameter.*

Therefore, the S parameter is related to the free volume hole sizes present in the material. The depth of penetration can be varied by varying the incident energy of the positrons. This depth can be calculated by making use of the following equation:

$$Z(E_+) = (400/\rho)E_+^{1.6} \quad 4.1$$

Z is the depth penetrated (nm), ρ is the density of the sample (kg/m^3) and E_+ is the incident energy (keV). By varying the depth of penetration slow positron beam analysis can be used to perform depth profiling. Information on the free volume of the material can thus be obtained from the very surface (<1μm) to deep into the bulk material (>9μm).

The positron beam measurements were performed on a variable mono-energetic positron beam. These measurements were done at the University of Missouri in Kansas City, USA. A detailed description of the beam can be found in Zhang *et al*. (2000)[7].

3.5. Precautions

Due to the carcinogenic and dangerous natures of most of the solvent used, all experiments were conducted in a well ventilated fume hood. The electrospinning process also makes use of a high voltage supply (as high as 30kV). Therefore great care was taken to ensure safety.

3.6. References

1. Taylor, G. *Proc. R. Soc. Lond. A* **1964,** 280, 383-397.
2. Kawai, T.; Akashima, M.; Teramachi, S. *Polymer* **1995,** 36, (14), 2851-2852.
3. Park, I.; Park, S.; Cho, D.; Chang, T.; Kim, E.; Lee, K.; Kim, Y. J. *Macromolecules* **2003,** 36, 8539-8543.
4. Cao, H.; Yuan, J. P.; Zhang, R.; Huang, C. M.; He, Y.; Sandreczki, T. C.; Jean, Y. C.; Nielsen, B.; Suzuki, R.; Ohdaira, T. *Macromolecules* **1999,** 32, 5925-5933.
5. Mallon, P. E.; Greyling, C. J.; Vosloo, W.; Jean, Y. C. *Rad. Phys. and Chem.* **2003** 68, 453–456.
6. Wu, Y. C.; Huang, C. M.; Li, Y., Z; Hang, R.; Chen, H.; Mallon, P. E.; Zhang, J.; Sandreczki, T. C.; Zhu, T. M.; Jean, Y. C.; Suzuki, R.; Ohdaira, T. *J. Polym. Sci. Polym. Phys.* **2001,** 39, (19), 2290-2301.
7. Zhang, R.; Cao, H.; Chen, H. M.; Mallon, P.; Sandreczki, T. C.; Richardson, J. R.; Jean, Y. C.; Nielson, B.; Suzuki, R.; Ohdaita, T. *J. Radiat. Phys. Chem* **2000,** 58, 639-644.
8. Puska, M. J.; Nieminen, R. M. *Rev. Mod. Phys.* **1994,** 66, 841.
9. Harrich, A.; Jagsch, S.; Riedler, S.; Rosinger, W. *Am. J. Underg. Res.* **2003,** 2, (3).

Results and Discussion

This chapter takes a closer look at the results obtained for the various techniques used to analyze the prepared PMMA-g-PDMS hybrid copolymer as well as the morphology and characteristics of the subsequently electrospun nanofibers. These results are then also discussed to give more insight into the characteristics of the graft copolymer. The preparation and evaluation of composites based on the nanofibers are also discussed.

4.1. Copolymer Synthesis

4.1.1. Introduction

As stated earlier, hybrid copolymers enable us to combine various properties of different materials into that of a single material. In the section to follow, it is described how the synthesized PMMA-g-PDMS hybrid copolymer was characterized using Nuclear Magnetic Resonance (NMR), Size Exclusion Chromatography (SEC), Gradient Elution HPLC and Size Exclusion Chromatography (SEC) coupled to Transmission Electron Microscopy (TEM) via LC Transform.

4.1.2. Determination of Molar Mass with SEC

One of the objectives in this study was to use the synthesized bulk copolymer to electrospin nanofibers. A crucial element needed to achieve electrospinning is that the polymer must have a sufficiently high molar mass and that the solution must have sufficient viscosity. When the polymer solution leaves the needle (or pipette in this case) it is stretched as it travels towards the collector (or lower potential). During this stretching process it is the entanglements of the polymer chains that prevent the jet from breaking up and thereby maintains the continuous solution jet. For this reason monomeric materials do not undergo electrospinning[1]. When the molar mass is too high, which in turn results in too high a viscosity, the solution can dry at the pipette tip and initiation of electrospinning can not occur[2].

The molar mass data for all samples are summarized in Table 4.1 below. Two different PDMS macromonomers were used during synthesis. A macromonomer with a shorter molecular weight of 800 to 1200g/mol was used as well as a macromonomer with a longer chain length of 4000 to 6000g/mol. The wt% PDMS charged was also varied. In the short series the wt% PDMS was increased step wise to yield different copolymer compositions. The short series was therefore charged with 5, 8.6, 10, 15, 23 and 34wt% PDMS respectively. Three compositions, 5, 10 and 23wt% PDMS, were studied with the longer, medium series.

Table 4.1

Molar mass of various prepared copolymer samples showing the effect of increasing the wt% PDMS charged.

Sample	M_n	M_w	M_n/M_w
(1) PMMA	89 689	174 616	1.95
(2) Short[a] 5 wt% PDMS	78 172	130 190	1.67
(3) Short[a] 8.6 wt% PDMS	83 547	178 624	2.14
(4) Short[a] 10 wt% PDMS	146 255	268 360	2.08
(5) Short[a] 15 wt% PDMS	69 983	154 331	2.2
(6) Short[a] 23 wt% PDMS	95 654	284 623	2.98
(7) Short[a] 34 wt% PDMS	101 405	354 527	3.5
(8) Medium[b] 5 wt% PDMS	71 120	126 572	2.02
(9) Medium[b] 10 wt% PDMS	67 925	129 446	1.9
(10) Medium[b] 23 wt% PDMS	79 237	142 776	1.8

[a] 800-1200g/mol

[b] 4000-6000g/mol

Looking at the above data it can be seen that all samples generally showed good polydispersity for conventional free radical polymerization, ranging from between 1.5 and 3. For the short series polydispersity, however, increases with increasing wt% PDMS charged. This is most likely due to the randomness of incorporation of the graft chains characteristic of the conventional free radical polymerization mechanism, where some chains will have more side chains than others. For the short series the molecular weight increases with increasing wt% PDMS charged. This increase in molecular weight is not seen for the medium series and molecular weights are much lower than for the short series.

4.1.3. Characterization with NMR after PDMS macromonomer extraction

All samples were analyzed using ^{1}H NMR and ^{13}C NMR. Integration of the chemical shift on the ^{1}H NMR spectra was then done to determine the amount of PDMS incorporated into the graft copolymer after extraction of unreacted macromonomer. Below in Figures 4.1 and 4.2 one can view a typical ^{1}H NMR spectra obtained for pure PMMA (Figure 4.1) and a PMMA-g-PDMS hybrid copolymer (Figure 4.2). Integration of the chemical shift at δ 4.07ppm (c in Figure 4.1 and e in Figure 4.2) for the methyl protons of the O-CH_3 peak of PMMA was compared to the proton integrations of the Si-CH_3 peak on the silicone backbone at a chemical shift at δ 0.5ppm (a in Figure 4.2). These peaks were identified using NMR prediction software. By doing so, the mol% PDMS incorporated into the graft copolymer was determined. Figure 4.2 also shows the terminating methyl protons on the silicone backbone at a chemical shift of δ 0.9ppm. Table 4.2 below shows a summary of the copolymers synthesized and the corresponding mol% PDMS incorporated into the graft polymer.

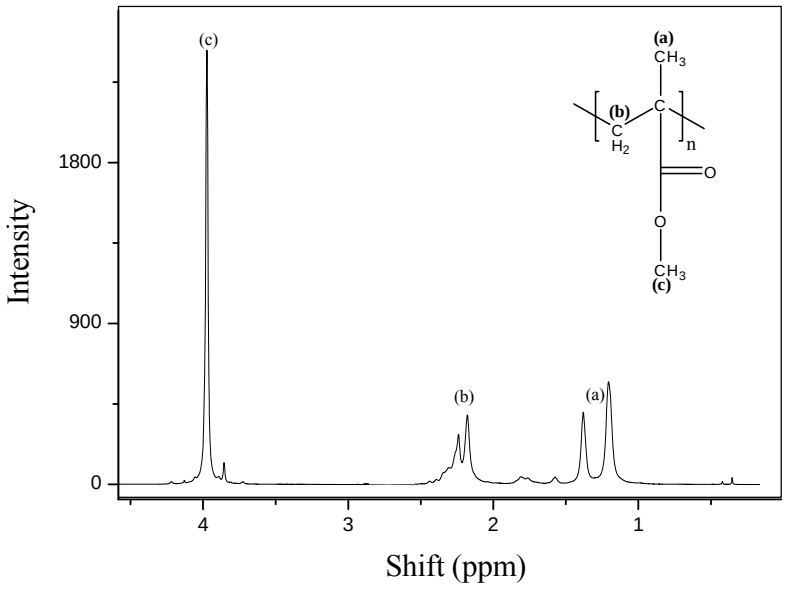

Figure 4.1 *A typical ^{1}H NMR spectra of pure PMMA showing the O-CH_3 peak of PMMA (c) integrated at 4.07ppm.*

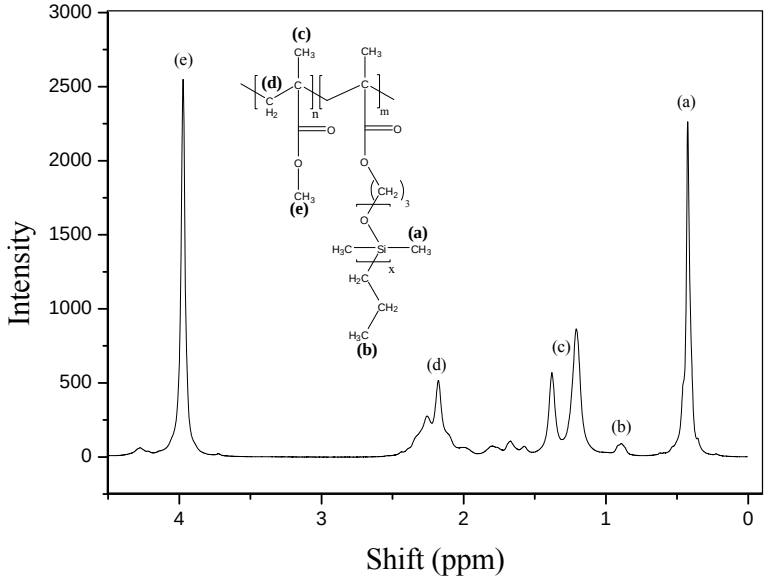

Figure 4.2 *A typical ^{1}H NMR spectra of a PMMA-g-PDMS graft copolymer after extraction of the PDMS macromonomer*

Table 4.2
Summary of PMMA-g-PDMS copolymers

Sample ID	wt% Charged	mol% Charged	mol% Incorporated via NMR	% Incorporated (mol via NMR/ mol charged)
"Short" 800-1200g.mol^{-1} PDMS Macromonomer				
PMMA	0.0	0.000	0	0
MS05	5.0	0.657	0.294	44.80
MS09	8.6	1.163	0.5348	45.98
MS10	10.1	1.387	0.5685	40.98
MS15	15.1	2.174	1.1447	52.66
MS23	23.1	3.618	1.9133	52.88
MS34	34.1	6.076	3.8829	63.90
"Medium" 4000-6000g.mol^{-1} PDMS Macromonomer				
MMS05	5.1	0.134	0.061	45.69
MMS10	9.9	0.276	0.127	46.10
MMS23	23.2	0.752	0.1919	25.52

Samples charged with 0.657mol% (5wt%) of the “short” macromonomer yielded copolymers with 0.294mol% PDMS incorporated. Increasing the wt%, however, led to a higher incorporation of PDMS relative to the amount of PDMS charged. For example, comparing the mol% incorporated to the mol% charged for each sample (mol %/mol %) it can be seen that sample MS05 yielded a 44.8% incorporation, whereas MS34 yielded a 63.9% incorporation. Table 4.2 shows that incorporation of the longer PDMS chains yielded the opposite. Initially the incorporation was approximately 45% for a low amount of PDMS charged. Increasing the wt% PDMS charged, however, lead to a decrease in the incorporation. The reason for this is most likely due to the size of the longer PDMS macromonomer. More of the “longer” bulkier chains decreases the mobility of the growing chains and leads to less incorporation. The smaller MMA molecules, compared to the “longer” macromonomer, have much more mobility. When more of the bulky macromonomer is added, they almost impede each other and allow the smaller more mobile MMA molecules to be added more easily to the growing chain. This causes less of the PDMS chains to be incorporated and thus lower % incorporation. When less macromonomer is charged, less of the bulky chains impede on each other and more are added to the growing chain leading to a higher incorporation.

4.1.4. Gradient Elution HPLC

It is well known that graft copolymers synthesized using a low-molecular weight monomer and macromonomer by radical polymerization display heterogeneity in molecular mass as well as chemical composition. Therefore, the characterization of these materials by a single

technique (like Size Exclusion Chromatography, SEC) is made difficult by the effects of both molecular mass and chemical composition on the separation mechanism. Techniques such as SEC with selective detection cannot be used to completely characterize copolymers due to the fact that the hydrodynamic volume, necessary for characterization, is dependant on the chemical composition. Gradient Elution High Performance Liquid Chromatography also known as Gradient Polymer Elution Chromatography (GPEC) is a good technique for separating via chemical composition[3].

Graft copolymers may contain ungrafted homopolymer and side chain homopolymers, as well as copolymers varying in composition. In this project Gradient Elution Chromatography was used to analyze the copolymers and monitor the extraction of unreacted macromonomer as well as to determine the chemical composition distribution[4]

HPLC analysis was performed with a combination of precipitation HPLC and adsorption or retention HPLC. By starting with a non-solvent and increasing the percentage of a good solvent on a stationary phase possessing strong adsorption interactions with small-pore column packings, copolymer retention was achieved that resulted in compositional separations. In this case a Nucleosil 100 Si-5µm (25 x 0.46) column was used. A compromise between copolymer solubility and chromatographic solvent strength was used to ensure copolymer separation over a broad chemical composition distribution.

The premise on which the separation works can be explained as follows: PDMS homopolymer is completely soluble in toluene, ethanol and cyclohexane, and is therefore unretained on the silica packing. The graft copolymer however is insoluble in the starting solvent mixture of 40% toluene/ethanol (90:10) and 60% cyclohexane. The mode of retention is therefore the governing factor in determining the actual separation. The retention process in this case (PMMA-g-PDMS copolymer) for the cyclohexane-toluene/ethanol solvent system on silica relies on initial precipitation, followed by adsorption retention after redissolution in the solvent gradient of the graft copolymer.

It was also found by Timothy C. Schunk *et al*[3]. that PDMS only displays weak adsorption interactions with the silica packing and that PMMA cannot elute with toluene as a strong solvent[5]. It was for this reason that a low percentage of ethanol was added as a hydrogen-bond displacer, despite the fact that ethanol is a non-solvent for both graft copolymer components.

Development of the gradient elution profile

Several gradients were tested before obtaining optimal separation. Variables that were investigated include the rate at which the percentage of non-solvent to good solvent was changed, the way in which it changes, as well as the amount of sample injected. Both linear and non-linear gradients were tested. Below are illustrations of some of the gradients tested but not used. The reason for this is that they either resulted in bad separation or variable separation. Profile #1, for example, yielded good separation but results were not consistent and therefore unusable. For all profiles the amount of sample injected was varied from 20µl to 100µl. Profile #7 (shown in Figure 4.4) yielded good separation between unreacted PDMS macromonomer, PMMA-g-PDMS copolymer and PMMA homopolymers and more importantly, results were consistent for multiple runs. In this profile it was also found that a sample injection volume of 60µl provided optimal results. Throughout the development of the gradient profile a sample flow rate of 1mL/min was used.

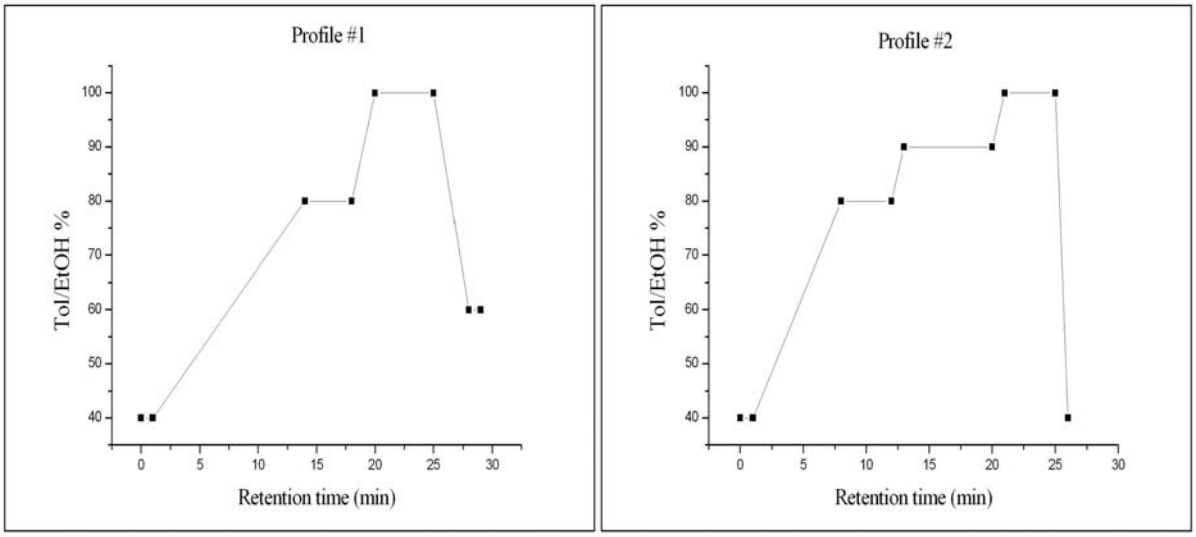

Figure 4.3(a) *Gradient elution profiles used for chemical composition separation; stationary phase: Nucleosil 100 Si-5µm, eluent: cyclohexane/(toluene + 10% ethanol)*

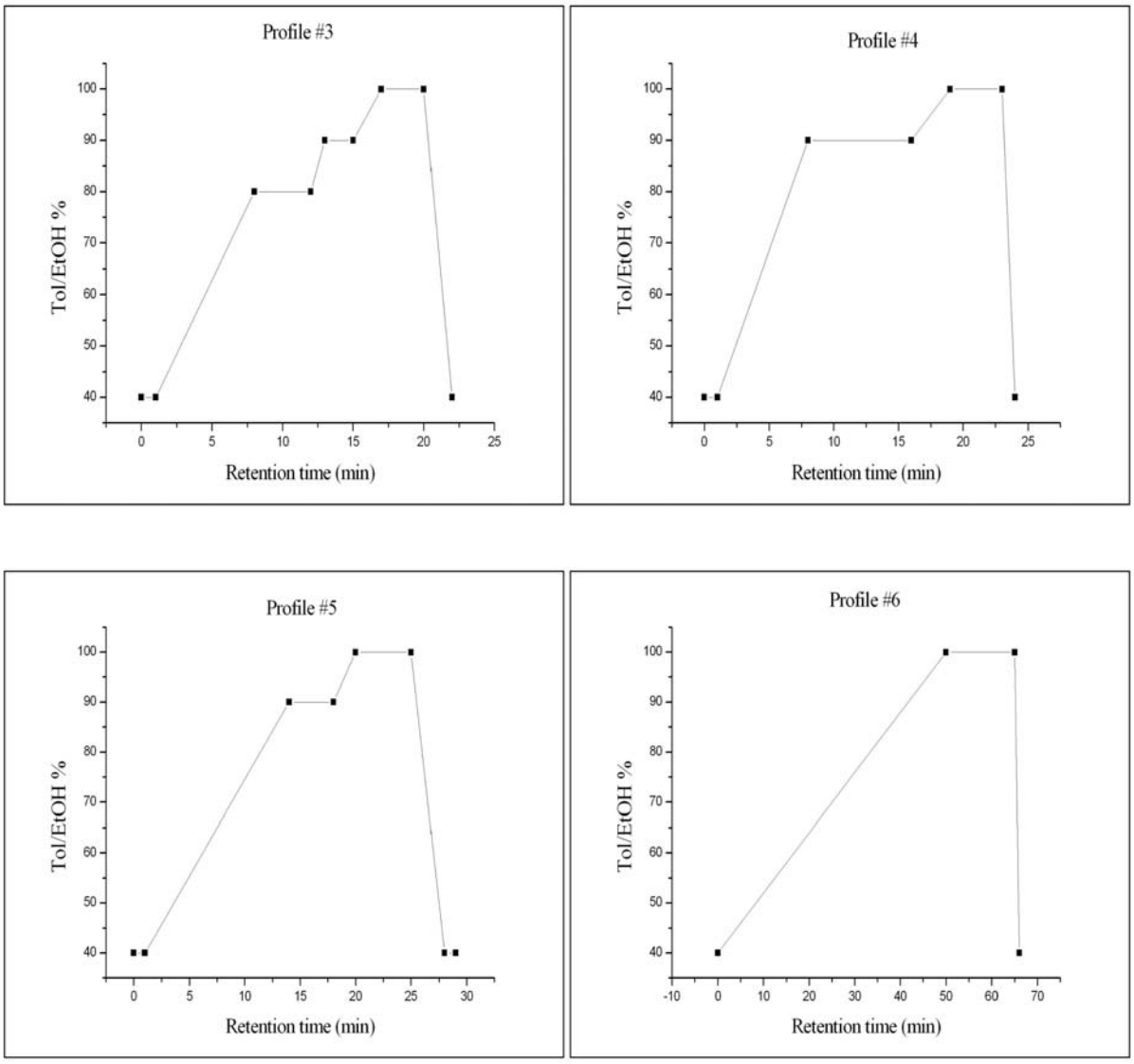

Figure 4.3 (b) *Gradient elution profiles used for chemical composition separation; stationary phase: Nucleosil 100 Si-5µm, eluent: cyclohexane/(toluene + 10% ethanol)*

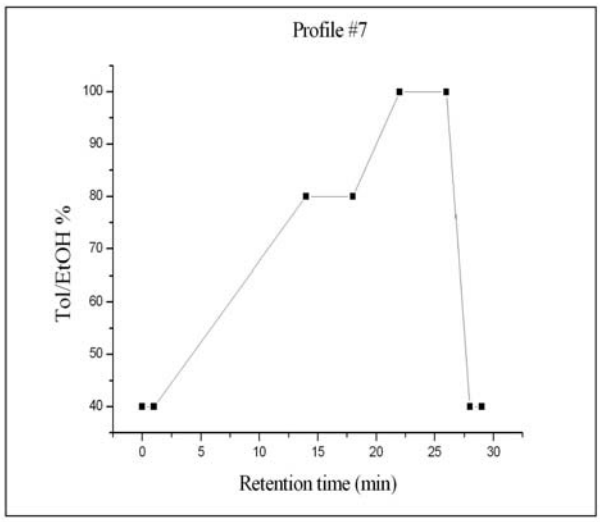

Figure 4.4 *Gradient elution profiles used for chemical composition separation; stationary phase: Nucleosil 100 Si-5µm, eluent: cyclohexane/(toluene + 10% ethanol)*

PMMA and PDMS standards of different molecular weights were used to identify their retention times in the elution profile. Figure 4.5 shows the retention times of these components. PDMS elutes between 2 and 3 minutes whereas PMMA homopolymers elute between 24 and 25 minutes.

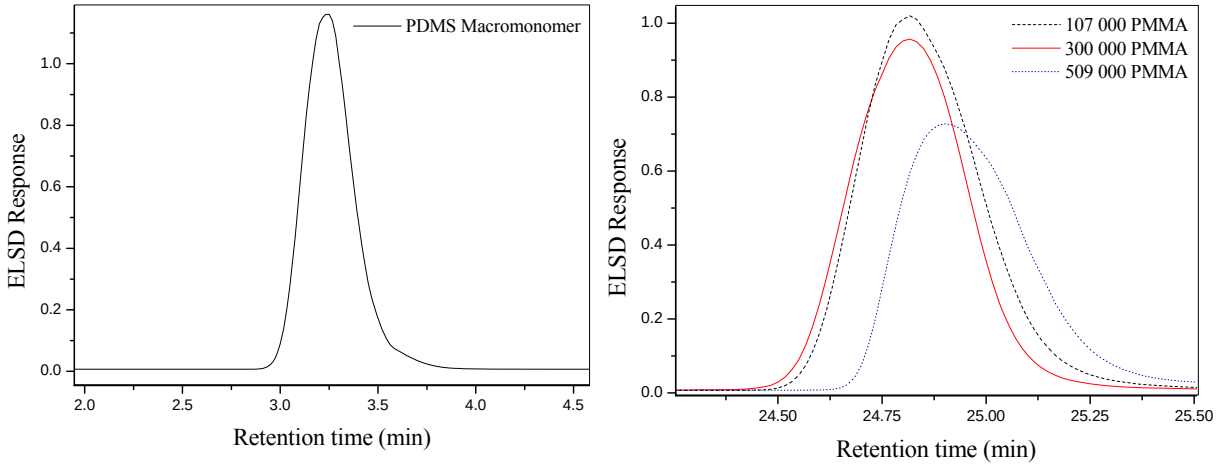

Figure 4.5 *HPLC elution plots of PDMS and PMMA Standards*

Figure 4.6 shows a typical gradient elution analysis of a graft copolymer before extraction of the unreacted PDMS macromonomer. Here it can be seen that the PDMS homopolymer elutes at approximately 3 minutes followed by the graft copolymer between 15 and 20min and lastly the PMMA homopolymer at 22 minutes.

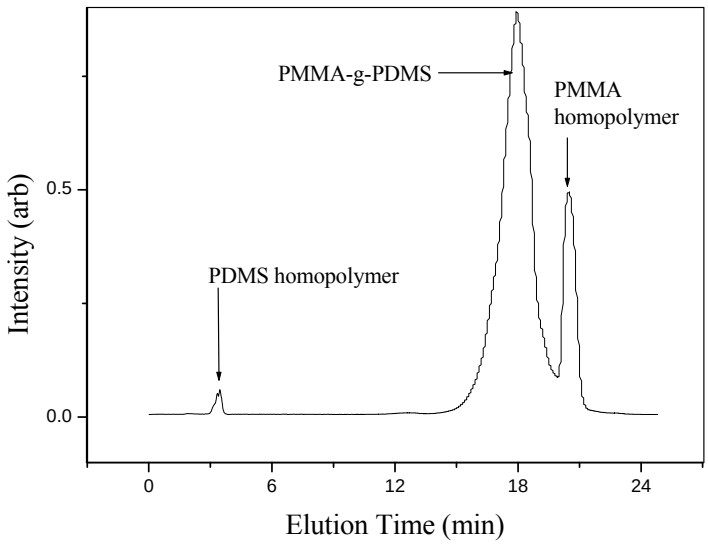

Figure 4.6 *Gradient HPLC chromatogram of a 23wt% PDMS "short" graft copolymer sample.*

Figure 4.7 shows the results of three different graft copolymer compositions after separation via gradient elution HPLC. It was noticed that with increasing wt% PDMS there was a shift in the time at which they eluted, namely to lower retention times. This is due to the fact that separation occurs according to the chemical composition. Higher wt% PDMS samples have a higher % PDMS. PDMS is not retained on the column as well as PMMA, and therefore, with a higher PDMS density the higher wt% samples elute earlier. All graft copolymer samples investigated showed similar gradient profiles.

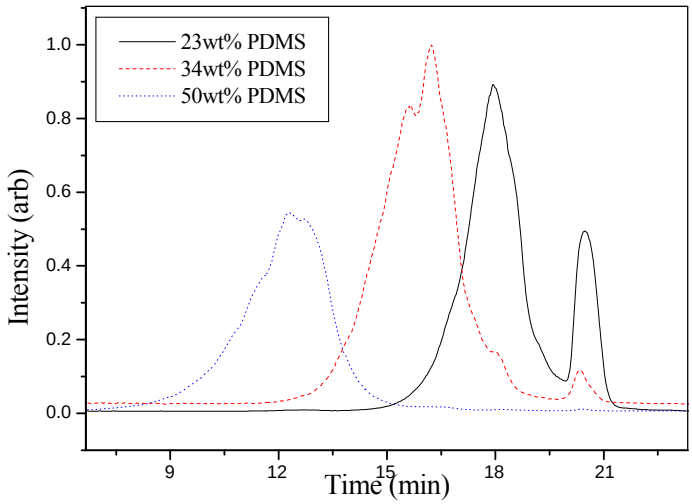

Figure 4.7 *Gradient elution HPLC chromatogram of graft copolymers with different graft densities.*

4.1.5 SEC coupled to TEM via LC Transform

As mentioned previously the incompatibility of the PDMS and PMMA will lead to phase separated morphologies. In this section a technique that has recently been developed in our group was applied to study both the chemical composition of the graft copolymers as a function of the molar mass and to study changes in the solid state morphology as a function of molar mass and chemical composition. This is achieved by using an LC transform device coupled to SEC. Firstly a conventional deposition is done on a Ge disk which is then taken and analyzed via Fourier Transform Infra-Red. This allows for the determination of the chemical composition at each point along the molar mass distribution curve by analysis of the FTIR spectra at each point. The second step involves a novel technique developed in our group which allows the LC transform device to collect fractions that are then taken to TEM which allows for morphological analysis of each fraction. The bulk polymer is dissolved in THF (5mg/ml) and injected into a HPLC machine where separation occurs via the size exclusion mode. Using a LC transform device the polymer then exits the machine and is deposited on silica chips that were fastened to the germanium disc (this is depicted in Figure 4.8 below)[6]. After deposition the silica chips are removed and transferred to 2ml vials and rinsed off with THF. The solution is then placed in a Petri dish filled with water. Because the polymer is hydrophobic it will form a thin film at the surface of the water whereas the THF will diffuse into the water. This thin film at the top of the surface is then carefully placed on top of TEM grids, which are then transferred to a vacuum oven where they are annealed at 120^{o}C for 48 hours. This method allows for the polymers to be deposited as thin films which can then easily undergo TEM analysis. The results obtained from this study are shown below.

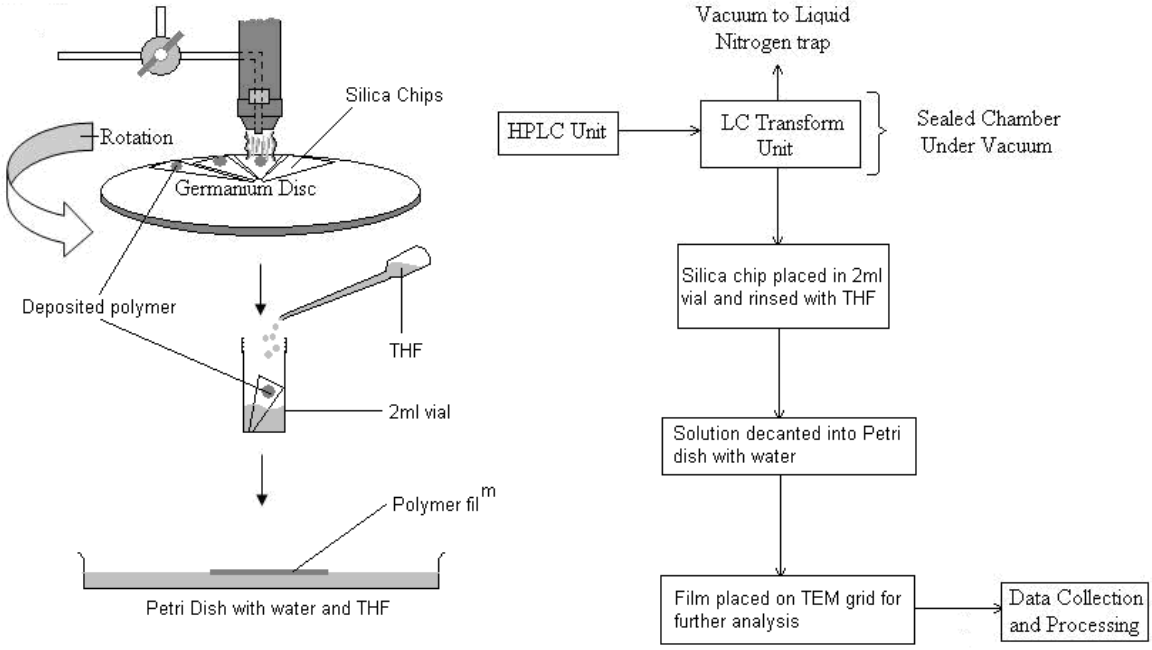

Figure 4.8 *Procedure used during SEC coupled TEM via LC transform*[6].

The Graham Schmidt plot shown in Figures 4.9 and 4.10 represents the data collected for a 23wt% and 34wt% sample respectively, separated via SEC. This was obtained by analyzing the polymer deposited onto the germanium disc in a Perkin Elmer FTIR spectrometer using Timebase software. By doing so chemical composition could be determined at specific points as the polymer eluted. This provided crucial information regarding the chemical composition and enabled the determination of the SiO/CCH_3 ratio (seen as the red line overlaid on the Graham Schmidt plot in Figures 4.9 and 4.10). This was done by taking the heights of the SiO peak at $1088cm^{-1}$ and the $C\text{-}CH_3$ peak at $1729cm^{-1}$. The chemigram of the SiO/CCH_3 ratio shows that there is a relatively good and even distribution of the PDMS grafts in the copolymer. In the TEM images the PDMS domains appear as dark regions and the PMMA as lighter regions. Figures 4.9 and 4.10 also show that three regions were analyzed further via TEM. Deposited polymer was taken in the first, middle and end sections.

The TEM images in Figure 4.9 show phase segregated morphology of the graft copolymers due to the incompatibility of the components. The largely spherical PDMS domains are distributed in the PMMA matrix. In the first fraction the average size of the PDMS domains are approximately 280nm in diameter. In the end fraction the domain size decreases to 140nm in diameter and it is shown in Figure 4.9 that these PDMS regions have smaller PMMA

domain inclusions of an average diameter of 20nm. The TEM image of the central fraction does not show clear boundaries for this separated domain structure.

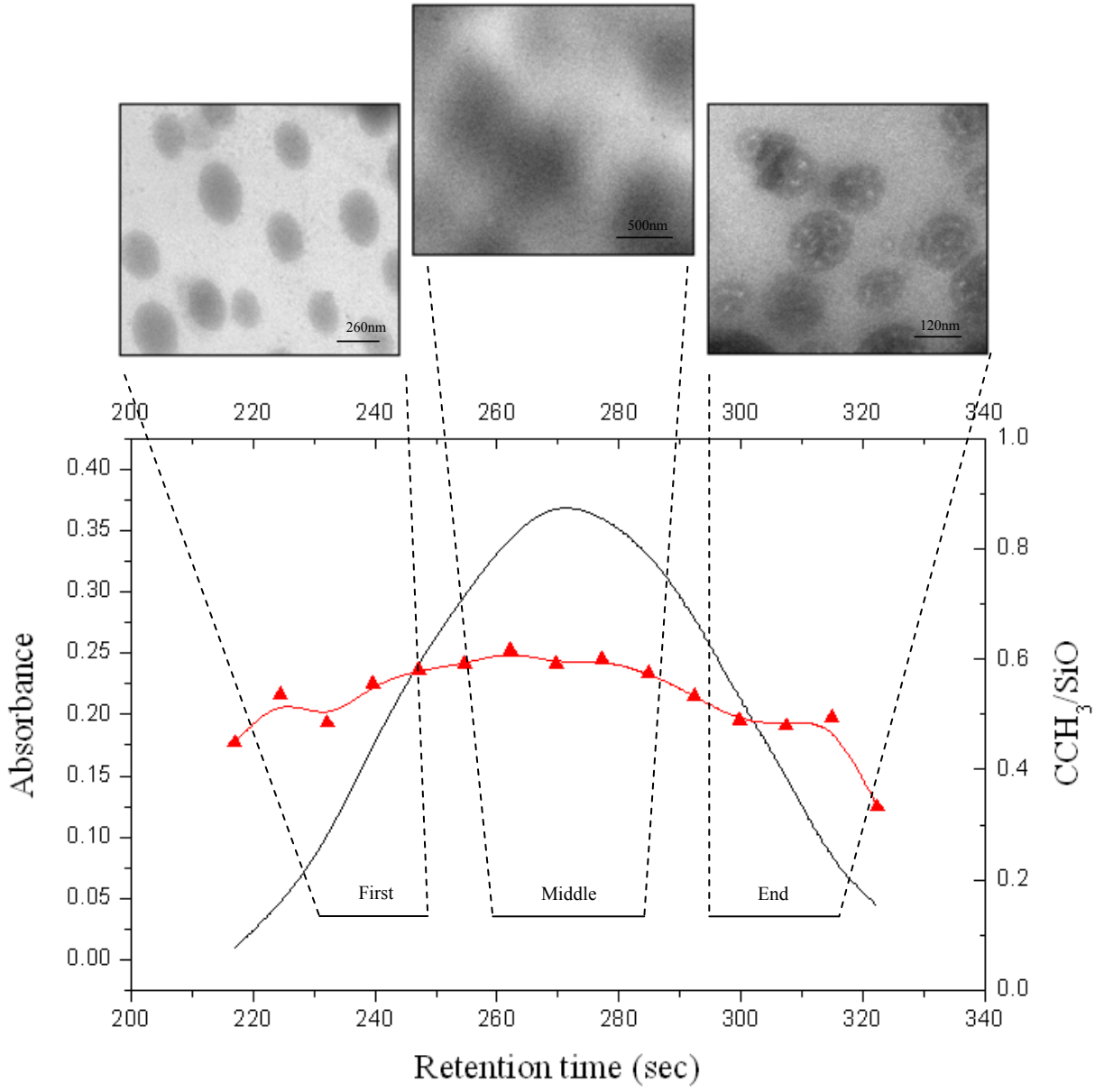

Figure 4.9 *Graham Schmidt plot and the SiO/CCH_3 ratio as well as the TEM images for a 23wt% PDMS sample.*

The TEM images for the 34wt% PDMS sample in Figure 4.10 show a similar phase segregation morphology as the lower PDMS content copolymer. The middle fraction shows a novel vesicular and acorn vesicular structured image. The end fraction image shows a completely different morphology with a much more ordered smaller domain size. This is very similar to the morphology observed by Smith *et al*[7]. for high PDMS content grafts. They ascribed this as being an end-on view of a cylindrical type morphology, but it could also be a well defined micellar structure.

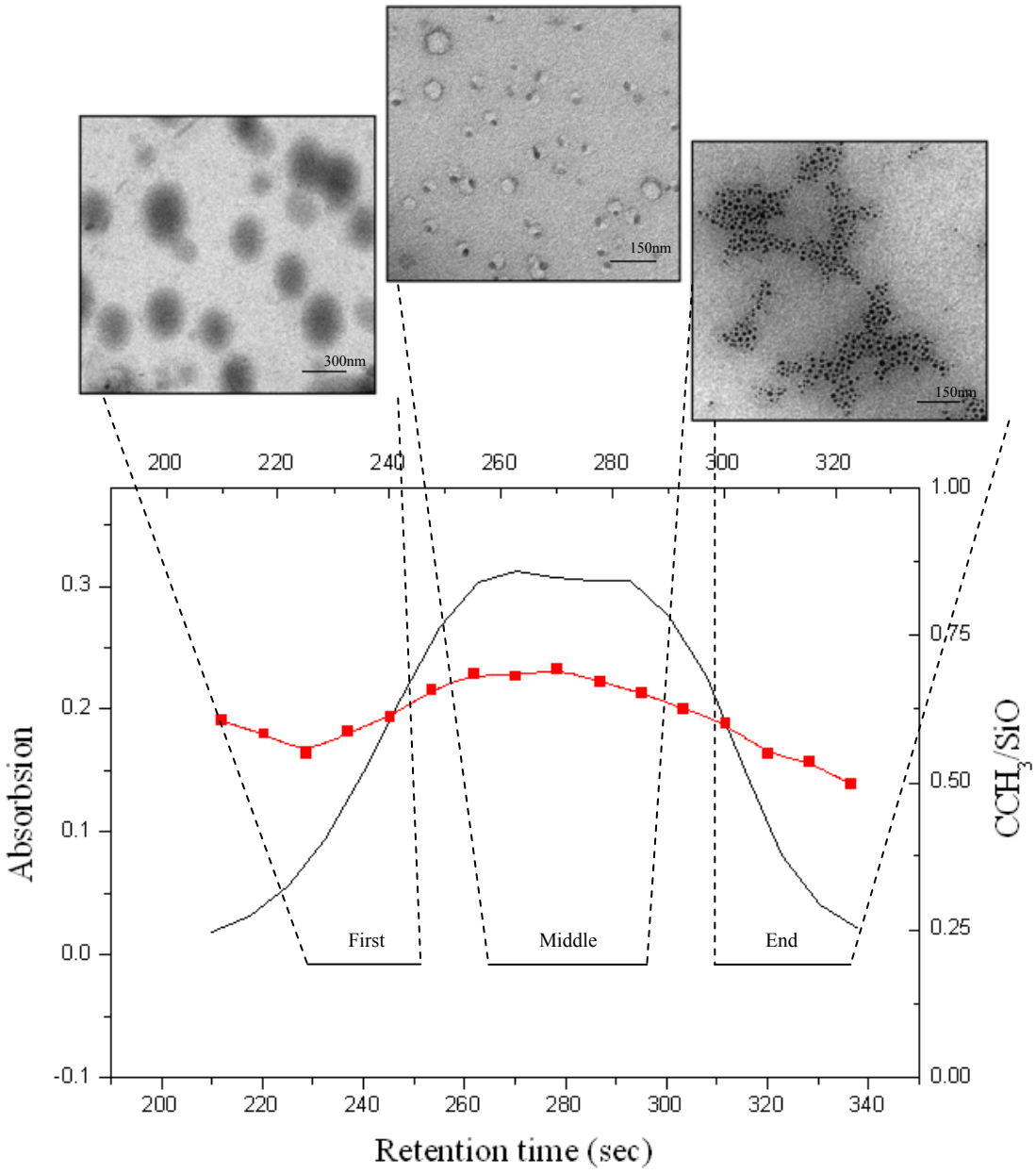

Figure 4.10 *This image shows a Graham Schmidt plot overlaid with a PMMA/PDMS band and the TEM images taken from a 34wt% PDMS sample*

S.D. Smith *et al*[7] established that the degree of phase separation becomes greater with increasing PDMS molecular weight. In the case of the lower wt% PDMS sample the morphology was a more spherical domain type texture. This however changed to a more ordered cylindrical texture as seen at the end of the 34wt% sample. When looking at the PMMA/PDMS band ratio for both samples it must be noted that when the ratio decreases (indicating more of the PDMS component) that the morphology tends to take on a more ordered, and in the case of the higher wt% PDMS sample, a more cylindrical structure.

This preliminary study has shown that the coupling of SEC to TEM can be a useful analytical tool to study the morphology of the copolymers. Future work could investigate coupling of gradient elution chromatography to TEM to determine the morphology as a function of the chemical composition.

4.2. Electrospun Nanofibers

4.2.1. Introduction

Surface morphology is one of the most important properties affecting material characteristics such as hydrophobicity. It is for that reason that an in depth surface morphology study was done using Scanning Electron Microscopy (SEM) as well as Transmission Electron Microscopy (TEM). Using these techniques any changes in surface morphology due to different spinning parameters like voltage, solution concentration, tip-to-collector spinning distance etc. could be studied.

4.2.2. Fiber Surface Morphology

4.2.2.1. Scanning Electron Microscopy

Figure 4.11 shows representative SEM images of the different organic-inorganic PMMA-g-PDMS hybrid polymers that have been electrospun to form non-woven nanofiber surfaces. These images are the first reported example of the ability of PDMS based graft hybrid materials to be electrospun to form nanofibers. The series of images show the fibers for increasing weight percentage of PDMS incorporation and for different graft lengths. All samples were spun under the same conditions. These conditions included a Tip-to-Collector distance of 15cm, supplied voltage of 8 to 10kV and a solution concentration of 10% (w/w). Figure 4.11 shows that a variety of different fiber morphologies are obtained for the graft copolymers. Since all the spinning parameters are the same (voltage, TCD, solution concentration etc.) the difference in morphology must be as a result of the copolymer composition or viscosity. In some cases “beaded” structures are observed while in other cases a smooth fiber morphology is seen. The nature of the fibers in terms of the fiber diameter also differs for the various samples.

Changing the spinning parameters and the conditions of electrospinning inevitably led to changes in the surface morphology. The various spinning parameters and their effect on fiber morphology are discussed in section 4.2.3.

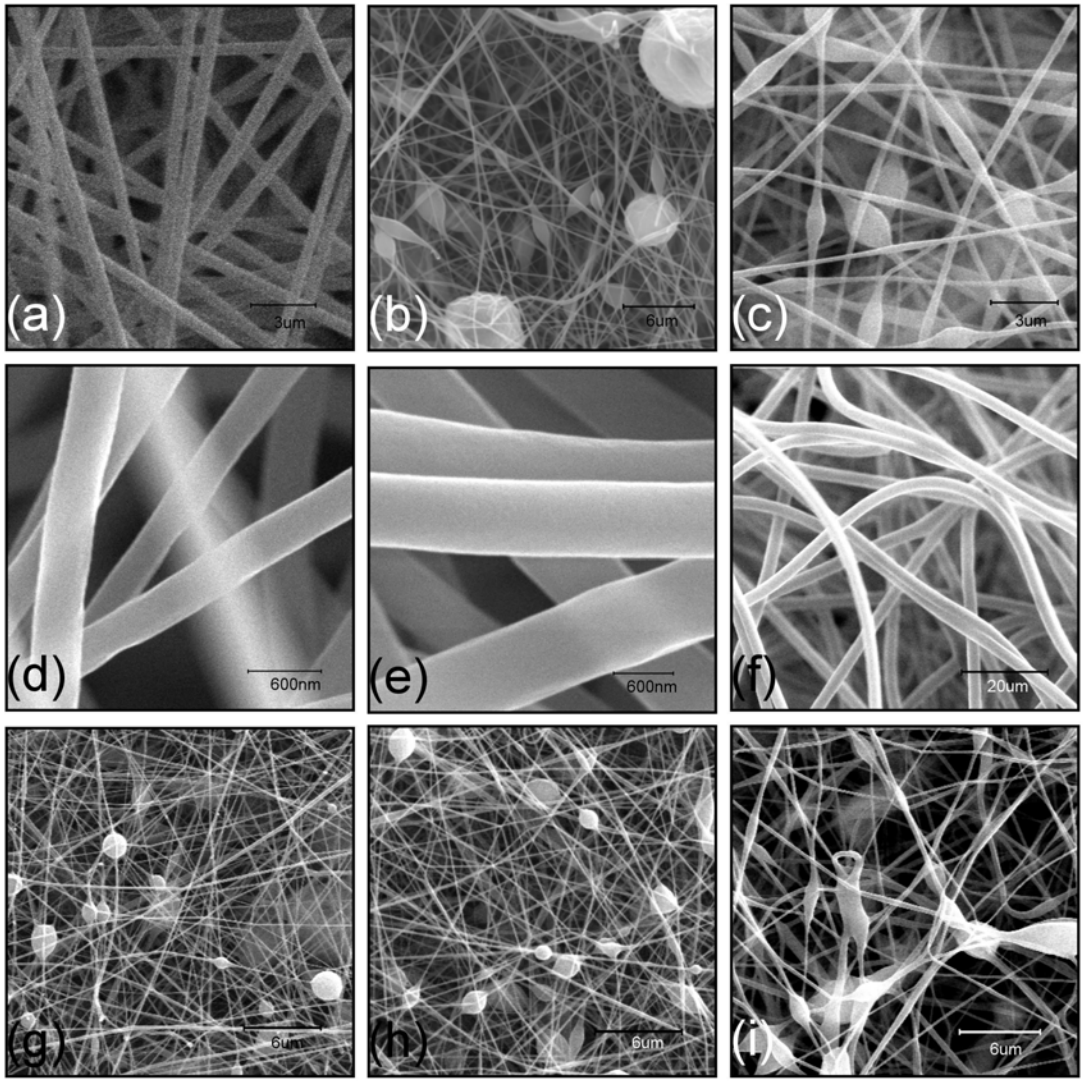

Figure 4.11 *SEM images illustrating the different surface morphologies with respect to the wt% PDMS charged. (a) PMMA, (b) 5wt% PDMS short, (c) 8.6wt% PDMS short, (d) 10wt% PDMS short, (e) 23wt% PDMS short, (f) 34wt% PDMS short, (g) 5wt% PDMS medium, (h) 10wt% PDMS medium and (i) 23wt% PDMS medium. Where short and medium indicates the average molecular mass of the PDMS macromonomer used. Short equals 800 to 1200g/mol and medium equals 4000 to 6000g/mol.*

4.2.3. Parameters influencing fiber morphology

4.2.3.1. Tip-to-Collector Distance (TCD)

Two arbitrary distances (15cm and 20cm) were chosen to establish the effect of spinning distance on the fiber morphology. These two distances were chosen because all polymer samples electrospun readily at these TCD's. As can be seen in the SEM images (a in Figure 4.12 and d in Figure 4.14), other distances were also tested but not all polymers were able to undergo electrospinning to form uniform nanofibers at these TCD's and they could not be used for comparative studies. Figure 4.12 below shows the images of a 10wt% PDMS sample at various spinnnig distances. Similar images of the fibers at different spinning distances are shown in Figure 4.13 and Figure 4.14 for the 23wt% and 34wt% PDMS copolymers respectively. A complete set of samples were however tested and the data obtained from these images are summarized in table 4.3.

Figure 4.12 (a) shows the 10wt% PDMS nanofibers spun at a TCD of 10cm which has an elongated beaded morphology. This is due to insufficient flight time which leads to an increase in field strength, which in turn causes jet instability leading to the formation of beaded structures. Figure 4.12 (b) shows a much more uniform fiber morphology. These fibers were spun at a TCD of 15cm. At this distance enough time is given for all solvent to evaporate before the fibers reach the collector plate and results in a smooth uniform fiber morphology. Figures 4.12 (c) and (d) represent nanofibers spun at a TCD of 20cm. The nanofibers again take on a beaded morphology. The reason for this is due to the fact that increasing the TCD can also lead to a decrease in the field strength, resulting in less stretching of the fibers. Insufficient stretching can lead to the formation of beads.

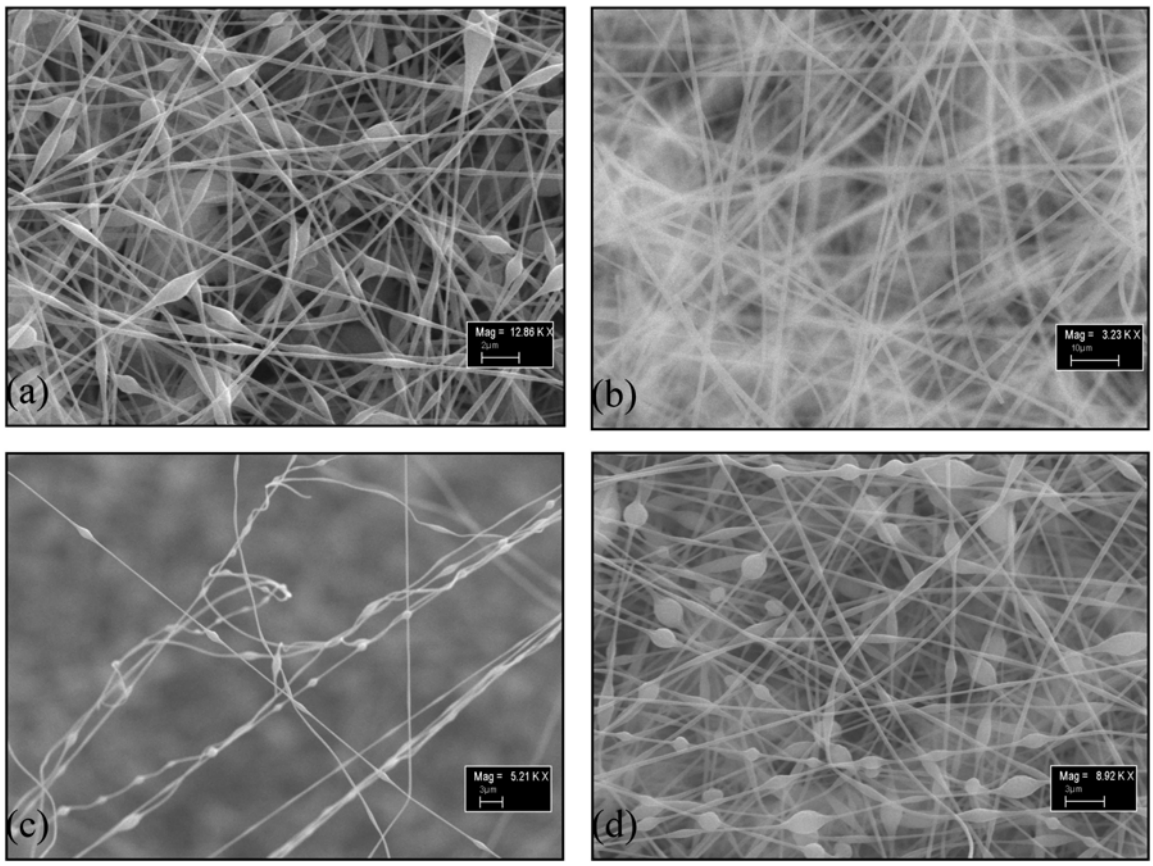

Figure 4.12 SEM images of a 10wt% PDMS copolymer sample showing the effect of different spinning distances on the fiber morphology. (a) 10cm, (b) 15cm, (c) 20 cm and (d) 20cm.

Figure 4.13 shows a 23wt% PDMS copolymer spun at a TCD of 15 and 20cm respectively. Again, elongated beaded structures (a in Figure 4.13) are observed at a TCD of 15cm and smooth uniform fibers at a TCD of 20cm.

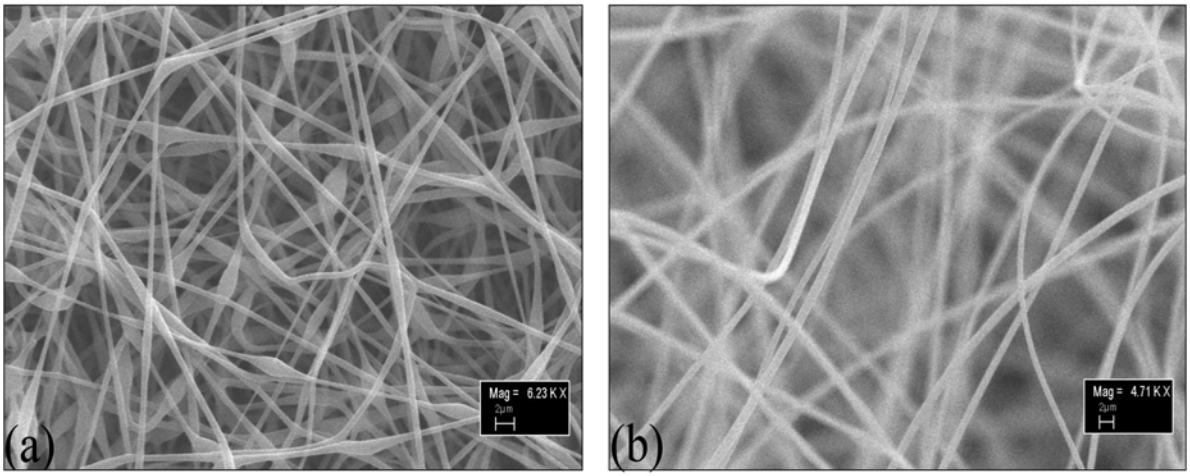

Figure 4.13 *SEM micrographs of 23wt% PDMS sample (a) 15cm and (b) 20cm*

Figure 4.14 shows the electrospun nanofibers of a 34wt% PDMS sample spun at a TCD of 15cm (a and b in Figure 4.14), 20cm (c in Figure 4.14) and 25cm (d in Figure 4.14). All fibers are smooth and uniform; however, fibers spun at TCD's of 15cm show numerous branching points in the fiber morphology. Branched structures are caused by the separation of the primary jet into two smaller jets. The elongation of the jet and evaporation of the solvent alter the shape and the charge per unit area carried by the jet. This shift in the charge per unit area leads to an unstable jet and the formation of branched fibers[8].

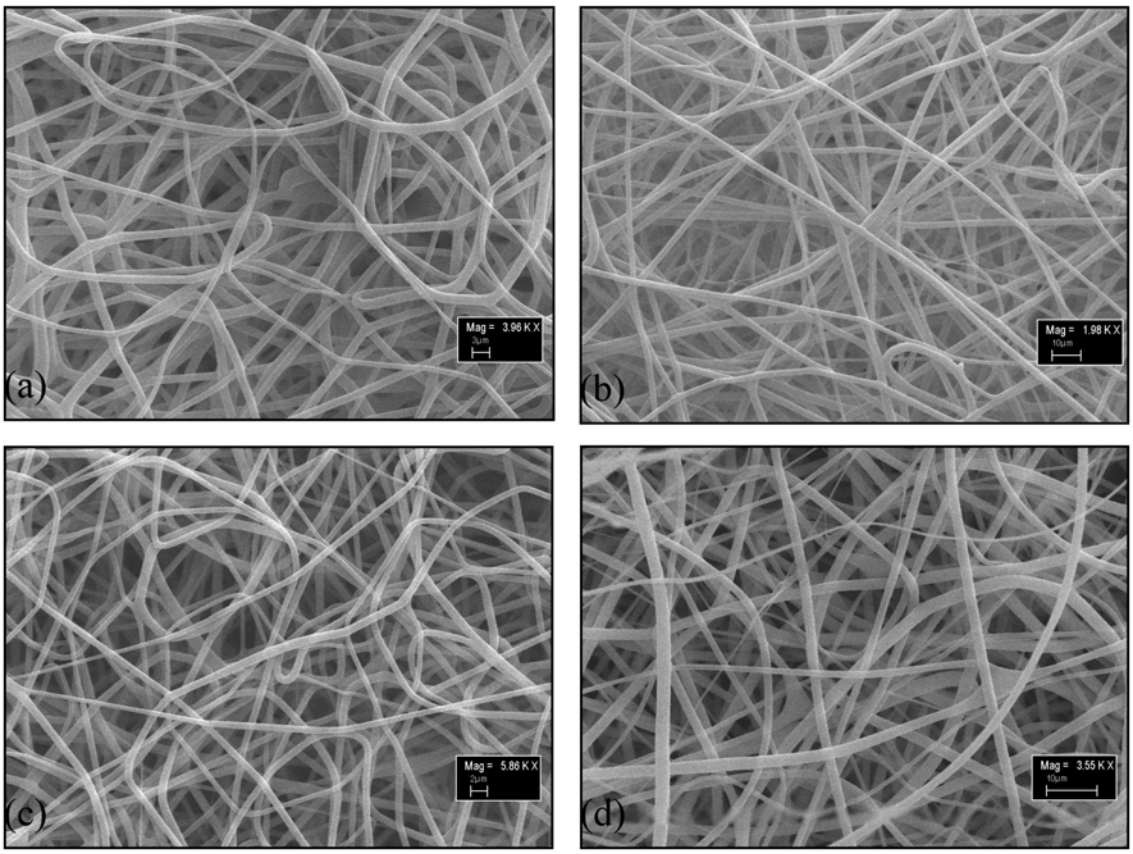

Figure 4.14 *SEM images of 34wt% PDMS sample (a) 15cm, (b) 15cm, (c) 20cm and (d) 25cm*

Table 4.3 shows a summary of the data collected for the complete series of samples spun at a TCD of 15cm and 20cm. This includes average fiber diameter and fiber appearance. Also shown is the Si/C ratio as determined by EDS analysis. EDS measures the elemental composition of the surface. This enabled the determination of the Si/C ratio in the nanofibers. As expected there is an increase in this ratio for the higher content PDMS samples.

Table 4.3 shows that the average fiber diameter decreases when the TCD is increased from 15 to 20cm. The decrease in the fiber diameter varies from as little as 10nm to as much as 300nm. The reason for this is that with an increase in the TCD there is an increase in the flight time resulting in more time for the fibers to be stretched and solvent to evaporate hence leading to smaller fiber diameters. The shorter TCD also results in more beaded fiber morphologies, whereas the higher TCD gives a much smoother fiber morphology.

Table 4.3

The influence of spinning distance on the average fiber diameter and appearance for various graft samples

Sample	15cm Tip-to-Collector Distance (TCD)		20cm Tip-to-Collector Distance (TCD)		Si/C Ratio
	Avg. Fiber diameter (nm)	Appearance	Avg. Fiber diameter (nm)	Appearance	(15cm TCD)
PMMA	950 - 1200	Smooth	900-1000	Smooth	-
Short[a] 5 wt% PDMS	Uneven	Highly Beaded	Uneven	Slightly Beaded	0.0108
Short[a] 8.6 wt% PDMS	Uneven	Beaded	Uneven	Smooth	-
Short[a] 10 wt% PDMS	580 - 610	Smooth	550-650	Beaded	0.0201
Short[a] 15 wt% PDMS	600 - 750	Smooth	500 - 600	Smooth	-
Short[a] 23 wt% PDMS	1000-1250	Slightly Beaded	800-1000	Smooth	0.0793
Short[a] 34 wt% PDMS	800-1500	Smooth	600-1000	Smooth	0.1
Medium[b] 5 wt% PDMS	195 - 205	Beaded	150-200	Beaded	0.0198
Medium[b] 10 wt% PDMS	180 - 210	Beaded	140-180	Beaded	0.0477
Medium[b] 23 wt% PDMS	60 - 200	Highly Beaded	100-180	Beaded	0.1662

[a]Short: 800-1200g/mol

[b]Medium: 4000-6000g/mol

Flight time as well as electric field strength affects electrospinning. In turn, varying the tip-to-collector distance (TCD) directly affects both flight time and electric field strength. As already stated earlier, all solvent needs to evaporate for individual fibers to form. By reducing the TCD the jet now has less distance to travel and the flight time is not long enough to allow sufficient solvent evaporation. Shortening the TCD also increases the electric field, which causes the jet to be accelerated more leading to a shortened flight time and thus not enough time for solvent evaporation. Insufficient evaporation leads to the fact that fibers may become merged together and lead to inter and intra layer bonding[1]. Another phenomenon observed when the TCD was decreased is the formation of beads. Megelski *et al*[9] stated that the reason for this is the increase in the field strength between the needle (or pipette) and the collector plate. Small distances result in insufficient stretching and hence the formation of beads. When looking at the data obtained it can clearly be seen that the samples indeed followed the same trend as stated in literature. A shorter TCD leads to the formation of beaded structures in most samples with lower wt% PDMS concentrations and when increasing the TCD the result was a much smoother fiber morphology. Only in the 5 and 10wt% medium PDMS samples did the morphology of the fibers stay beaded. This may indicate that the flight time was insufficient or the field strength was too strong, but other factors like viscosity and concentration also influences bead formation and it cannot be concluded to a certainty that this is indeed the case.

4.2.3.2. Concentration Study

As discussed earlier, the polymer needs to be in solution for it to undergo electrospinning. In this study the affect on fiber morphology due to different concentrations of the polymer in solution was studied. The graft copolymer with a 34wt% PDMS component was selected to be studied. Three solutions with different polymer concentrations were prepared. This included a 5% (w/w), a 10% (w/w) and a 15% (w/w) sample. The polymer was dissolved in a 60% Dimethylformamide and 40% Chloroform solvent.

Figure 4.15 shows the different surface and fiber morphologies resulting from an increase in the polymer solution concentration. Figure 4.15 (a) and (b) show the SEM images of a 5% w/w sample. Here fiber branching with varying fiber diameters is shown as well as various elongated beaded morphologies. Figure 4.15 (c) and (d) show a 10% w/w sample. Here the electrospun fibers take on a much smoother, uniform fiber morphology with no beaded structures. Figure 4.15 (c) and (d) show a 15% w/w sample with clear ribbon like morphologies that vary in diameter.

From literature it is known that solutions with too low concentrations do not have enough chain entanglements to withstand both electrostatic and Coulombic repulsion forces. This results in the fact that the solution jet breaks up into smaller charged entities, where surface tension then acts to minimize the surface area of the broken jet and hence leads to the formation of discrete spheres[10]. Sickle-shaped structures may also form as a result of the evaporation of the solvent within the droplets. Increasing the solution concentration gradually leads to the formation of combinations between smooth and beaded fibers. This is due to the fact that with higher concentration more chain entanglements can occur which prevent the solution jet from breaking up into smaller discrete spheres. When the solution concentration becomes high enough to completely prevent the solution jet from breaking up, smooth uniform fibers can be seen. This was indeed the case with the 10 w/w% sample. Increasing the concentration further led to the formation of ribbon like fibers. The formation of flat, ribbon-like fibers could be a result of the rapid evaporation of the solvent. Koombhongse *et al*[11] attributed this to the fact that due to the small size of the ejected, charged jet, the outer surface of the jet could "dry" much faster than its inner core. If the time which the jet travels to the collector plate is too short, the inner core will not have enough time to "dry" completely. After the jet deposited on the target, evaporation of the residual solvent continued. Since the outer surface of the depositing jets is "dry" already, the evaporation of

the solvent from the inner core could result in the collapse of the jets. This leads to the formation of flat ribbon-like fibers. Alternatively the ribbon like structure could be triggered by the need of the hybrid copolymer to phase segregate into lamellar structures forcing surface enrichment of PDMS.

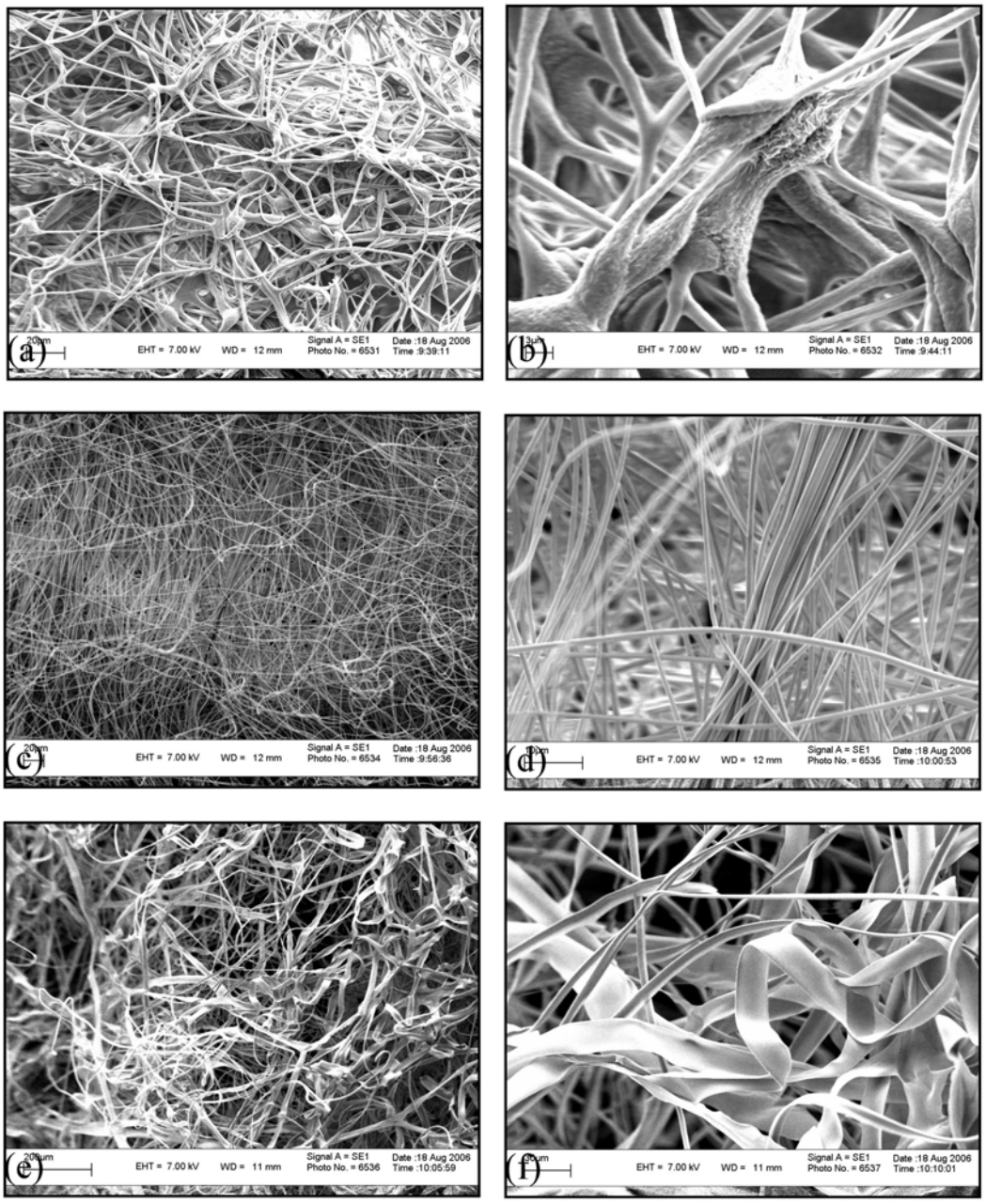

Figure 4.15 *SEM images illustrating the change in fiber morphology for an increase in the polymer solution concentration. (a, b) 5% w/w, (c, d) 10% w/w and (e, f) 15% w/w. (34wt% PDMS copolymer)*

4.2.4. Transmission Electron Microscopy (TEM)

One of the interesting features of these unique organic-inorganic nanofibers is that we could expect phase segregated morphologies in the nanofibers. TEM was done on the samples in order to attempt to see this phase segregation in the fibers. This proved to be extremely difficult for two main reasons. Firstly, the diameter of the fibers was generally too large to allow for transmission images and secondly the shape (cylindrical nature) of the fibers gives misleading images. Nevertheless it was possible to obtain some TEM images which show evidence of phase segregated morphologies on very thin fibers. These images are shown in Figure 4.16 below. In the images the difference in the electron densities of the PMMA and PDMS components in the graft copolymer allow the various components to be distinguished by TEM.

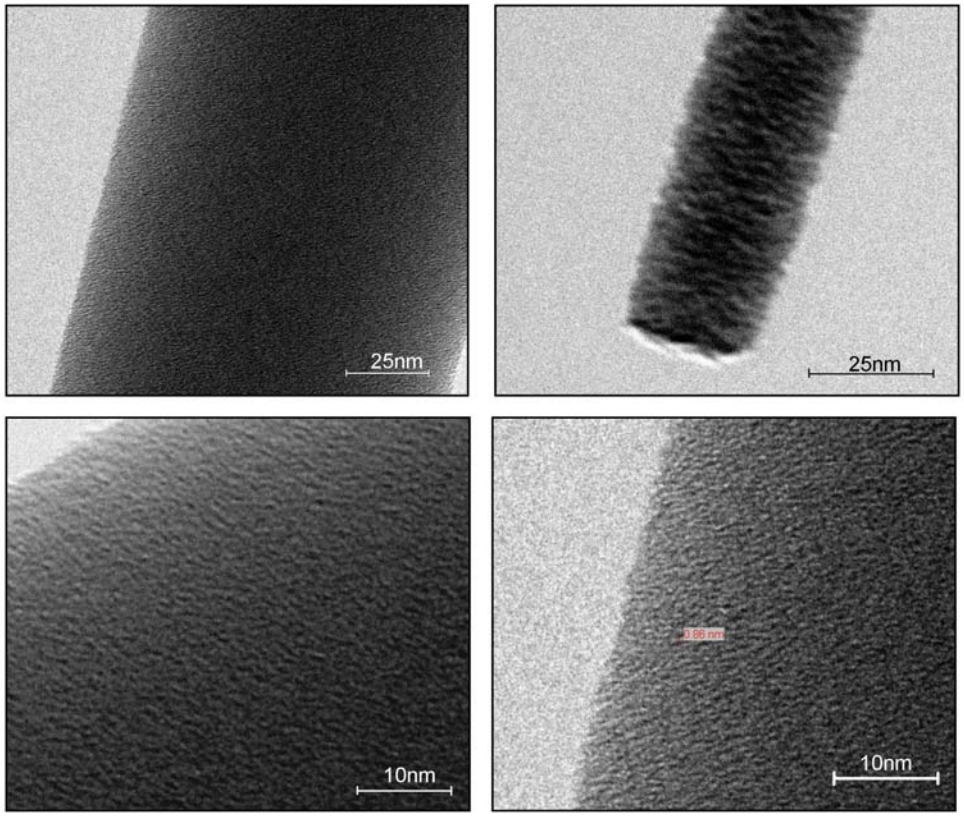

Figure 4.16 *TEM images showing the difference between the PMMA and PDMS components in the graft copolymer.*

PDMS is more electro dense due to the Si-O backbone and will tend to show darker regions on the TEM image. PMMA is less electro dense and shows lighter on the image. The images

in Figure 4.16 show some evidence of darker and lighter regions, but the darker areas are extremely small (about 0.86nm) which would suggest this is not a result of phase segregation.

An attempt was made to highlight the fiber morphology by selective degradation of the various components in the nanofibers. To do this the nanofibers were subjected to high temperatures in an oxygen atmosphere. The goal of this annealing process was to see how the nanofibers will react to severe conditions and also how the morphology and especially the surface morphology will change under these conditions. The fiber morphology was then investigated via TEM. The key to this study was to carefully control the conditions under which the annealing procedure takes place and to be extremely precise in the controlling of the atmospheric conditions. For this reason the study was performed using a TGA instrument as an oven for the annealing. By doing so the temperature, rate at which the temperature was changed, as well as the atmosphere in which the annealing took place could be carefully controlled. Great care was taken in handling the chosen nanofibers. The procedure for annealing the fibers were as follows. A carbon coated TEM grid was placed in the bottom of a ceramic TGA pan. Fibers were carefully selected and placed on top of the TEM grid. The pan was then placed in a TGA instrument under an oxygen atmosphere. The temperature was increased rapidly to 285^{o}C and kept isothermally there for 2 hours. Thereafter the TEM grid was removed for further analysis. The 285^{o}C temperature was chosen because TGA measurements done on these hybrid nanofibers show a dramatic weight loss at this particular temperature (thought to be that of the PMMA part of the hybrid nanofiber). Another weight loss was seen at approximately 390^{o}C which is thought to be that of the smaller PDMS part. The TGA as well as the TEM results are shown below in Figures 4.17 and 4.18

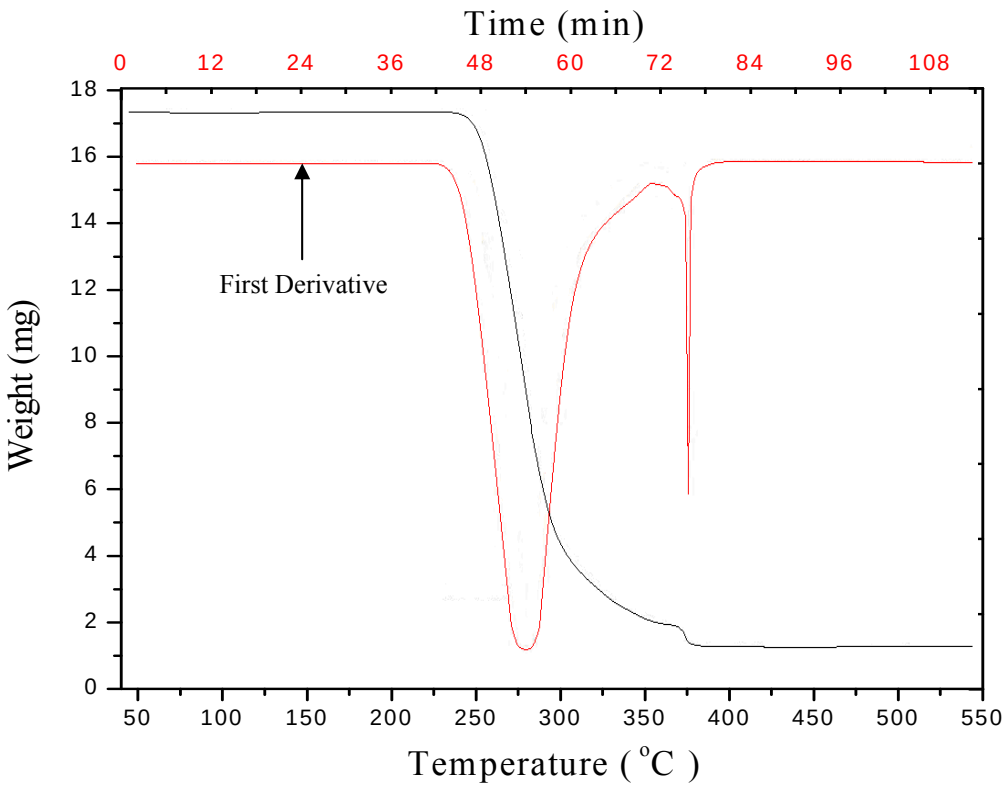

Figure 4.17 *TGA and the first derivative curve showing weight loss associated with the PMMA and PMDS components of the hybrid nanofibers as well as the first derivative curve.*

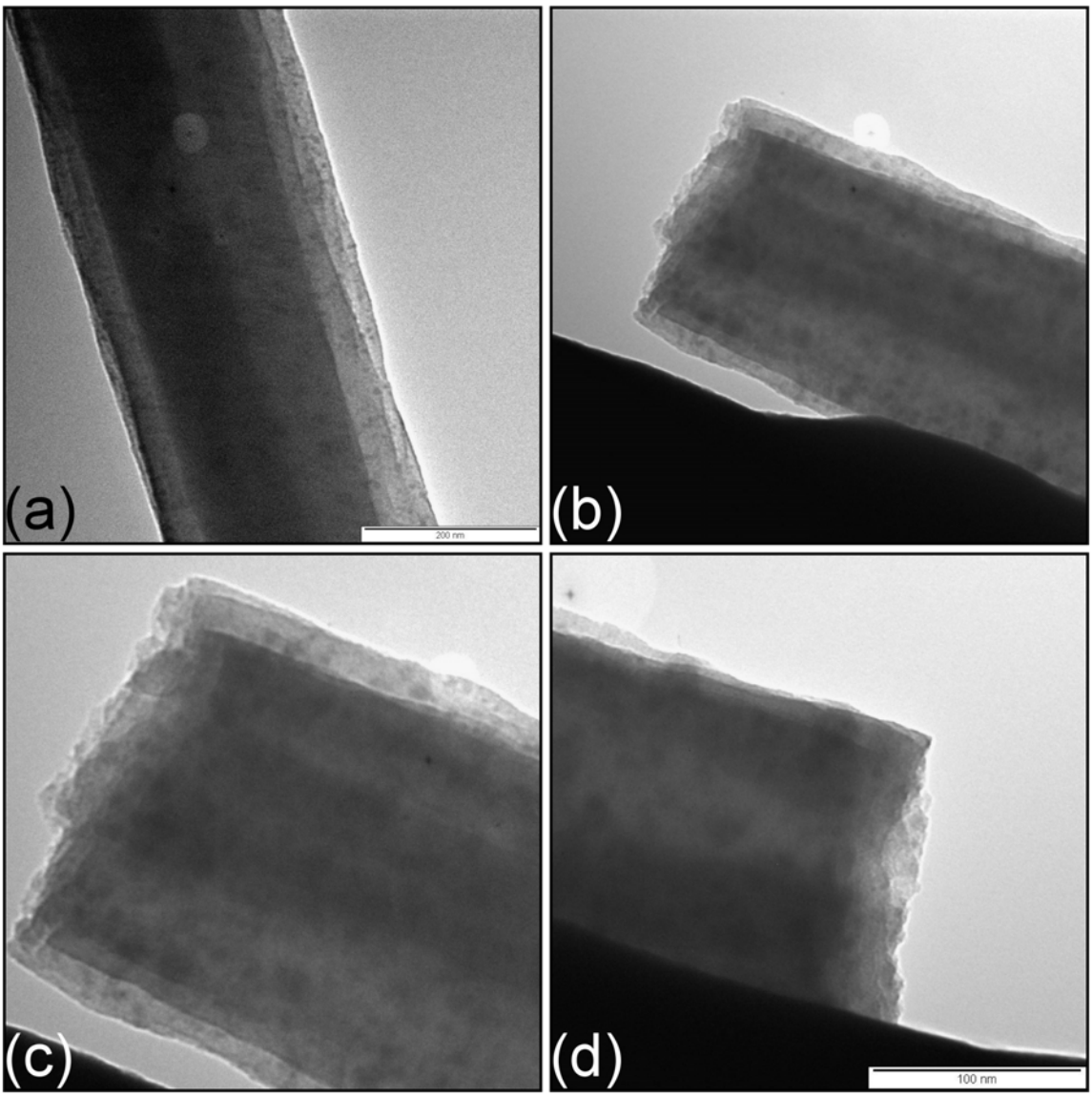

Figure 4.18 *TEM images taken of a 34 wt% PDMS sample after subjecting it to temperatures in excess of 250^{o}C for longer than 2 hours.*

The changes in the morphology of the nanofibers are fairly extreme. This is to be expected as a result of the harsh conditions the fibers had to endure. It can clearly be seen when looking at the Figure above that several morphological changes occur. Firstly, there seems to be the formation of spherical artifacts throughout the fiber. These darker shapes can be attributed to the PDMS domains of the hybrid nanofiber because PDMS is more electro-negative and will therefore show darker regions on the TEM image. The sizes of these spheres vary from 50nm to about 6nm but the average diameter seems to be approximately 12nm. The second change in morphology that can be seen is that the overall surface of the fiber takes on a flaky appearance and the surface of the fibers tends to form folds. The shape of the fiber, however, still holds it cylindrical shape.

4.3. Surface Properties

4.3.1. Introduction

Nanofiber fabrics have several potentially attractive features. These include; the potential of acting as a barrier against microrganisms and fine particulates; a potentially good strength per unit weight; a relatively high surface energy that indicates a potentially good moisture vapor transmission rate; the potential of being fabricated at room temperature with robust, simple capital equipment and a potentially low energy requirement for production[12]. Nanofibers however also bring with them certain problems. For instance, they may not be sufficiently wettable, fibers are generally very weak, they are not possible to color because they are seen by diffraction and not by reflection (fiber diameters are often less than the wavelength of light) and many engineering problems exist in making large quantities[12]. In this section we concentrate on the characterization of the surface of a PMMA-g-PDMS hybrid copolymer by making use of confocal Raman Spectroscopy and Doppler Broadening of Energy Spectra using Slow Positron Beam techniques. We also look at the effect on the surface properties after the surface was modified via exposure to corona discharge.

4.3.2. Confocal Raman Spectroscopy

Confocal Raman Spectroscopy is a very versatile technique that enabled us to identify specific chemical groups on the electrospun nanofibers. Figure 4.19 shows that the instrument enabled us to pinpoint a specific spot on individual nanofibers with an area of less than $1\mu m^2$. The instrument was fitted with an optical microscope that allows for the focusing of the beam on an individual 50wt% PDMS nanofiber at a 100X magnification. Table 4.4 shows a summary of the peak assignments for the Raman spectra. Figure 4.20 and 4.21 show the Raman spectra for the Si-O and $Si-CH_3$ regions of the various nanofibers respectively. The peaks at approximately $510cm^{-1}$, $725cm^{-1}$ and $2920cm^{-1}$ are characteristic of the PDMS in the copolymers and can be seen to increase in intensity with increasing wt% PDMS. This is in agreement with the NMR analysis of the copolymers.

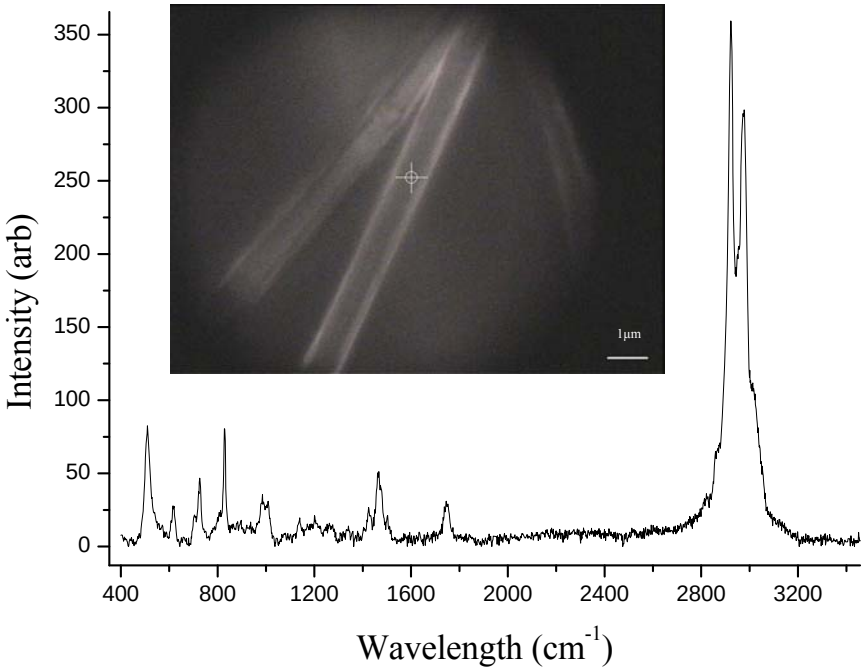

Figure 4.19 *A typical Confocal Raman spectrum of a 50wt% PDMS hybrid nanofiber. The inlay shows the point on the individual nanofiber where the spectrum was determined.*

Table 4.4
Peak identification for different Raman absorption peaks

Group	Region (cm^{-1})	Type
CH_3	2960	Asymmetric Stretching
CH_3 stretching of Si-CH_3	2925	Symmetric
C=O	1820-1680	~
CH_3	1450	Asymmetric Bending
CH_3	1200	Symmetric Bending
C-O-C	1150-1060	Antisymmetric vibration
Si-O-Si	1110-1000	Antisymmetric vibration
C-O	1124	Stretching
Mainchain C-C	991-960	~
Si-C	725	Symmetric Stretching
Si-O-Si	550-450	Symmetric vibration

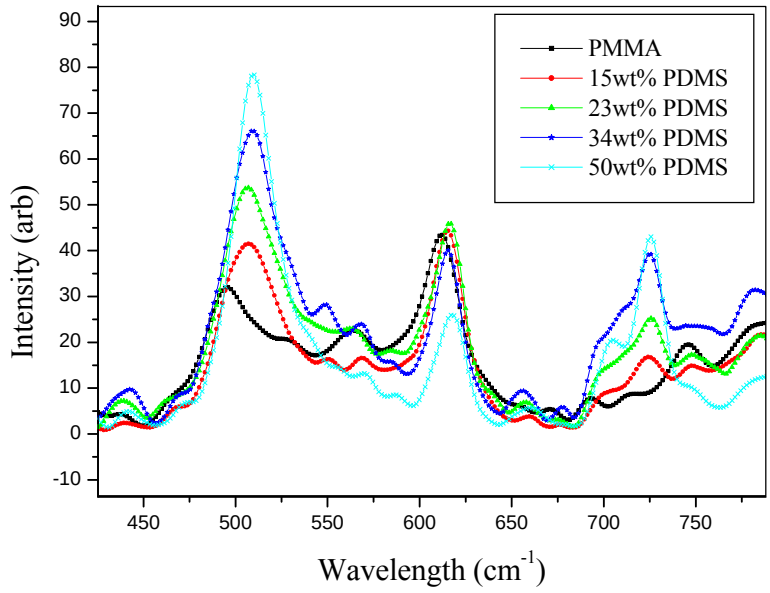

Figure 4.20 *Confocal Raman Spectra of the Si-O region at 510cm^{-1}as well as the Si-C peaks at 725cm^{-1}for increasing amounts of wt% PDMS.*

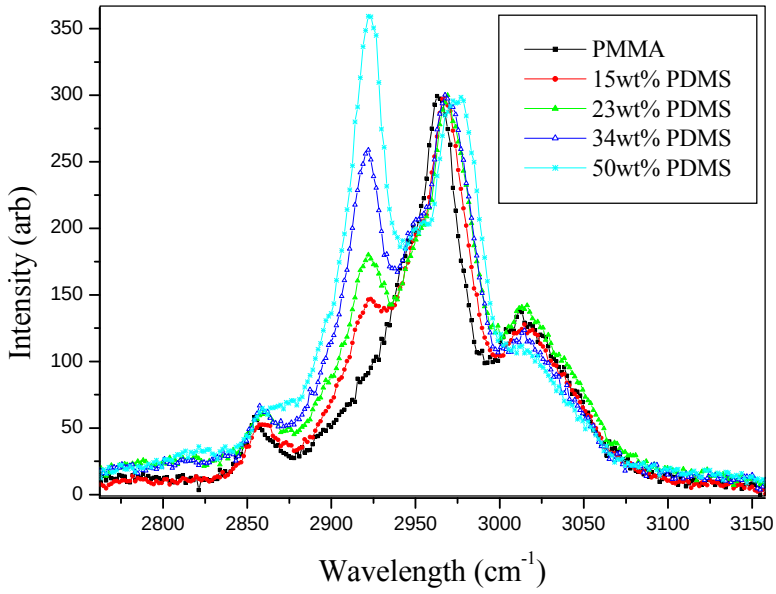

Figure 4.21 *Confocal Raman spectra indicating the characteristic Si-CH_3 peak at approximately 2925cm^{-1} that and the CH_3 asymmetric stretching band attached to the mainchain at approximately 2960cm^{-1}.*

4.3.3 Slow Positron Beam

Slow positron beam analysis of the polymer films and the electrospun polymer nanofibers was done. Slow positron beam techniques allow for the depth profiling of the free volume properties of the polymer surfaces. The data in this section is the first example of the measurement of the surface properties of electrospun polymer nanofiber surface using positron beam techniques.

The data in the Figures is reported as the S-parameter which is a measure of the Doppler Broadening of the annihilation Energy Spectra (DBES). In DBES data three main factors contribute to the S parameter: (1) free volume content, (2) free volume hole-size and (3) chemical composition. Larger free volume content relates to a larger S parameter value. Secondly, the S parameter is a direct measurement of the quantity of momentum distribution. This is due to the fact that the momentum has distributed according to the Heisenberg uncertainty principle.

$$\Delta x \Delta p \geq h/4\pi \qquad 4.2$$

Therefore, a larger hole size will result in a larger S parameter due to a smaller momentum uncertainty. The S parameter is a qualitative measure of the defect size and defect concentration in materials that consist of defects or voids like polymers. Lastly, the S parameter depends on the electron momentum of the elements present in the material. As the atomic number increases, the momentum increases and the S parameter decreases[13].

Figure 4.22 shows the S parameter profiles for the bulk polymer films. The initial increase in the S parameter at low positron implantation energy can be attributed to the fraction of both positrons and positronium annihilating in the polymer and at the polymer surface as well as the back diffusion of positrons and positronium into the vacuum prior to annihilation. This increase of the S parameter near the surface is typical of amorphous polymers which contain large fractions of sub-nanometer defects. After this initial increase there is a decrease in the S parameter at higher implantation depths in some cases. This is because at these higher implantation depths positrons travel through the polymer films and annihilate on the glass substrate. The point at which this decrease occurs corresponds to the thickness of the polymer film. The smaller S parameter is due to the fact that solid materials do not contain a large amount of defects[14-16].

Figure 4.22 shows that all the samples (with the exception of the 10wt% medium sample) show a larger S-parameter at the surface than that for pure PMMA. The higher measured S parameter at the surface can be attributed to the presence and preferential surface segregation of the PDMS component in the copolymers. A similar effect was found by Bayley *et al*[17] for PDMS-block-polystyrene copolymers.

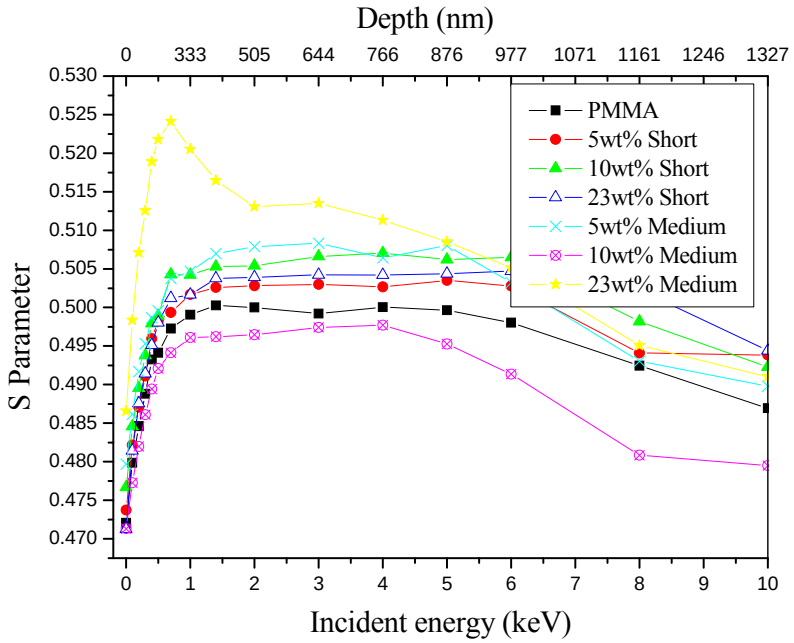

Figure 4.22 *S-Parameter profiles of bulk graft copolymer films*

Figure 4.23 shows the S parameter profiles for the electrospun polymer samples. It is interesting to note that the measurements at the very low positron implantation energies proved to be extremely difficult. In the case of some of the nano-fibers (for example the 10wt% PDMS short) the very low S-parameter at the surface is an anomaly as a result of the surface morphology. In all the electrospun samples with the very low S parameters at the surface, the "fluffiness" of the surface results in the positrons implanted with very low energies annihilating at a greater distance from the detector. This results in a very low count-rate and results in the anomalously low S parameters in these samples. This is further illustrated in Figure 4.24 where the S parameter profiles of the polymer films and the electrospun fibers are compared. In the case of Figure 4.24 a), c) and f) the low values at the surface are a result of this anomaly.

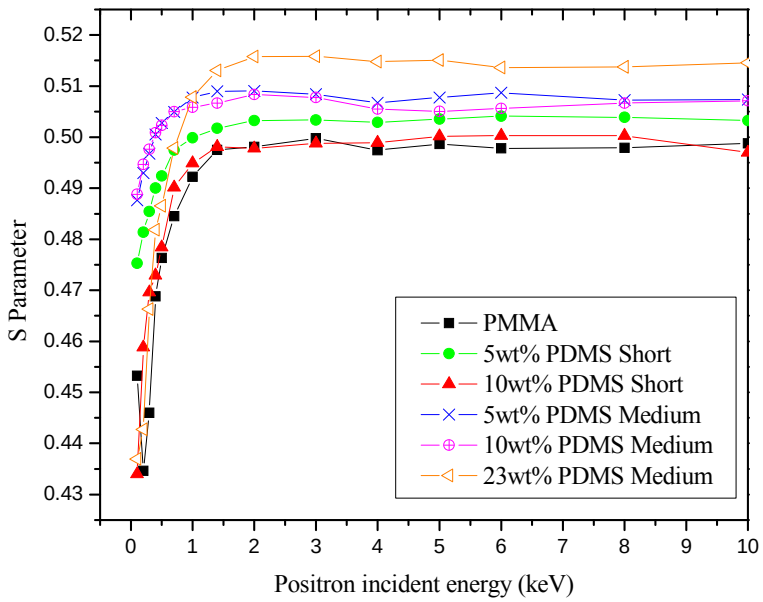

Figure 4.23 *S-Parameter profiles of electrospun PMMA-g-PDMS hybrid copolymer nanofibers.*

The slow positron beam results indicate that while the technique is useful and provides unique depth profiling information on the copolymer films, there are practical problems in using the technique to examine nano-fiber surfaces. It is clear that in order to get useful and reliable information on nano-fiber surfaces using slow positron beam techniques, methods will have to be developed to ensure that the samples do not "fluff" during the pumping down of the chamber to vacuum. Bulk positron lifetime measurements on nano-fiber samples would provide more reliable results since in this case the problems associated with "fluffing" would be eliminated.

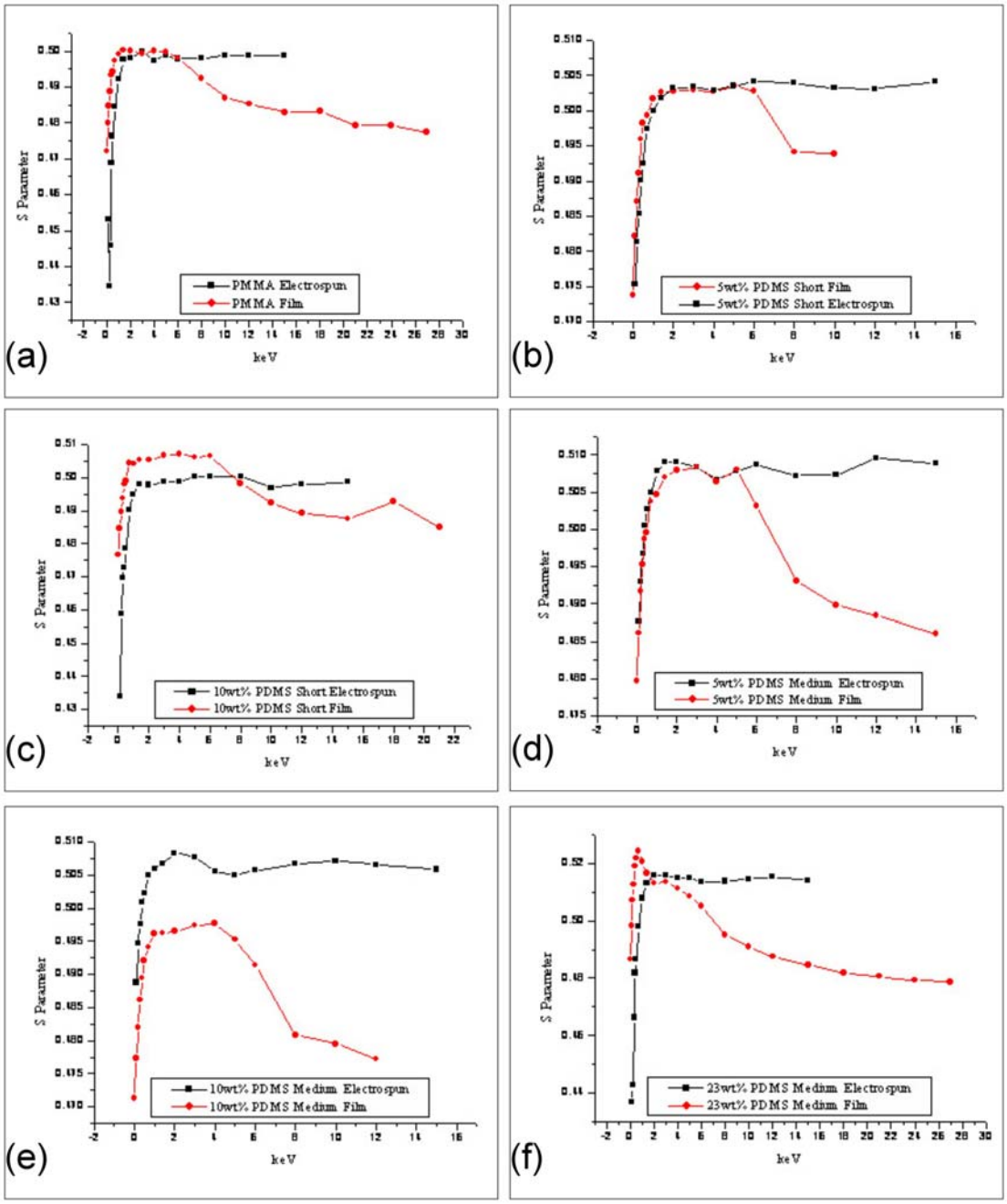

Figure 4.24 *Slow positron beam graphs comparing S parameter values of normal bulk films to that of electrospun fiber mats for a series of increasing wt% PDMS samples.*

4.3.4. Exploring Hydrophobicity

Static contact angle measurements were performed on the polymer films and on the electrospun samples to establish the hydrophobic character of the samples. The contact angles of normal spin coated films were also taken to help determine the effect of surface roughness on the contact angle. Table 4.5 shows the SCA measurements for a series of electrospun graft

copolymers and bulk polymer films. The results show a definite trend between the contact angle obtained and the wt% PDMS incorporated into the electrospun nanofibers. Also, there is a clear distinction between electrospun nanofibers and bulk polymer films, indicating that the effect of surface roughness plays a large role in the hydrophobic character of the graft copolymers. The electrospun samples show contact angles in excess of 150^{o} which classifies these surfaces as superhydrophobic. All contact angles are represented as an average value (the mean of ten drop measurements). The study was also performed to look at the effect of TCD on the superhydrophobic character of the surfaces. Figure 4.25 shows SCA images of water droplets on normal spin coated surfaces. The wt% PDMS charged increases from zero ((a) in Figure 4.25) to 34wt% ((h) in Figure 4.25). Contact angles only show a slight increase with an increase in the amount of PDMS incorporated into the copolymer, indicating the hydrophobic nature of PDMS. However, the SCA values of the bulk polymer films do not nearly approach superhydrophobicity ranges. A series of images illustrating the phenomenon of superhydrophobicity is also shown in appendix A.

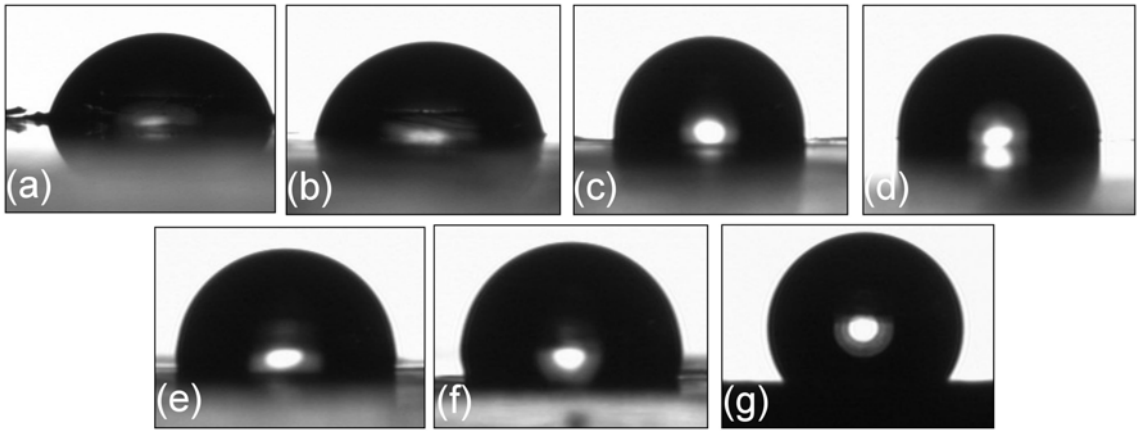

Figure 4.25 *Contact angle images of normal spin coated PMMA-g-PDMS bulk polymer films with increasing PDMS content. (a) PMMA, (b) 5wt% PDMS, (c) 8.6wt% PDMS, (d) 10wt% PDMS, (e) 15wt% PDMS, (f) 23wt% and (g) 34wt% PDMS.*

Table 4.5

Series of PMMA-g-PDMS samples used in a contact angle study and the average contact angle of each electrospun sample in relation to the two Tip-to-Collector Distance

Graft Copolymer Sample (wt% PDMS incorp.)	Electrospun Nanofibers		Bulk polymer films
	Average Contact Angle (15cm)	Average Contact Angle (20cm)	
0	123.2	124.93	75.6
5	130.62	153.01	92.7
8.6	135.48	160.91	94.7
10	140.32	157.76	97.6
15	148.94	165.07	97.1
23	159.8	166.09	95.1
34	163.07	169.65	104.8

Figure 4.26 shows SCA images of electrospun nanofibers at a TCD of 15cm. With these samples the change in the contact angle with an increase in the amount of PDMS incorporated is dramatic. The contact angle of pure PMMA ((a) in Figure 4.26) is approximately 123.2^{o}. The contact angle, however, increases to superhydrophobic ranges of 163^{o} for a 34wt% PDMS sample ((g) in Figure 4.26). Figure 4.27 shows SCA images for electrospun nanofibers at a TCD of 20cm. Here the change in hydrophobicity is even more dramatic, were the 34wt% PDMS sample shows a contact angle of 169.65^{o}. Figure 4.28 shows that TCD has a definite effect on the contact angle and hence the hydrophobicity of the surfaces. Also, comparing this to the maximum contact angle of 104.8^{o} achieved by the normal spin coated films, it is evident that there are additional factors contributing to the hydrophobicity of the material.

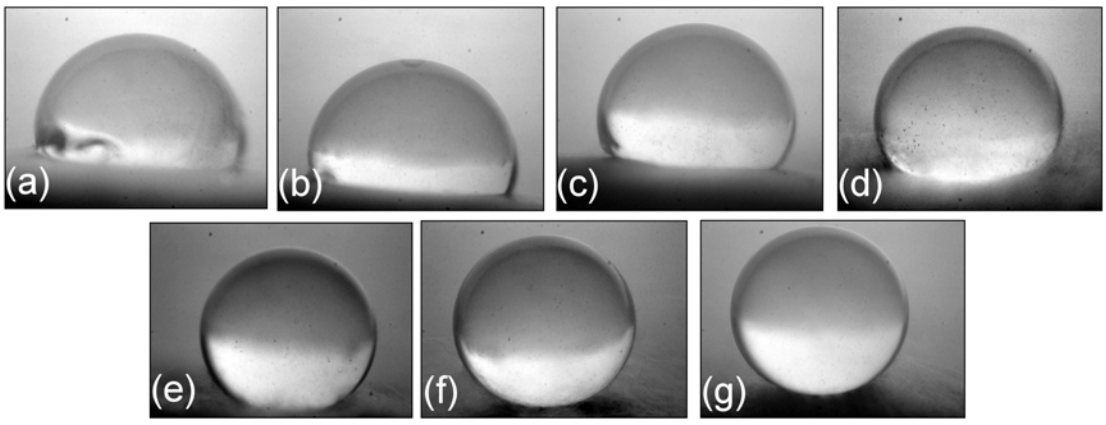

Figure 4.26 *Series of contact angle images on surfaces spun with a TCD of 15cm illustrating the change in hydrophobicity due to an increase in PDMS content. (a) PMMA, (b) 5wt% PDMS, (c) 8.6wt% PDMS, (d) 10wt% PDMS, (e) 15wt% PDMS, (f) 23wt% and (g) 34wt% PDMS.*

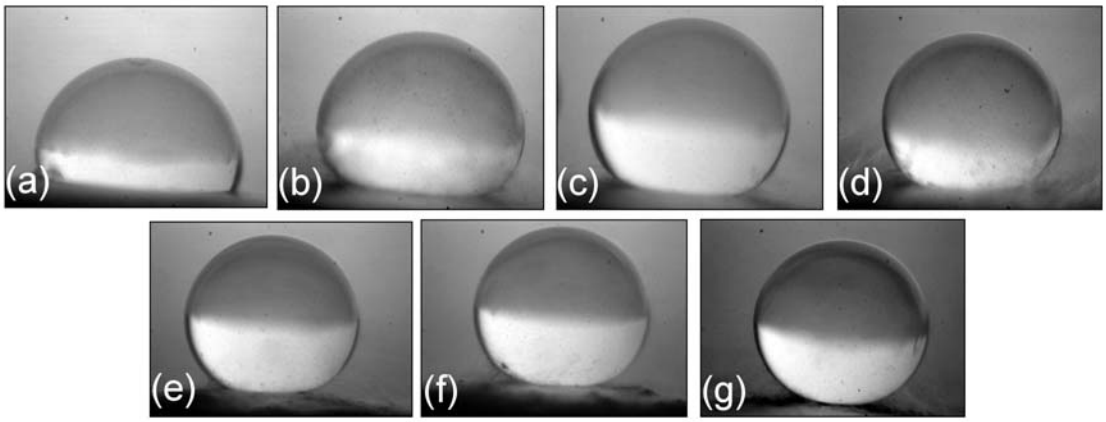

Figure 4.27 *Series of contact angle images on surfaces spun with a TCD of 20cm illustrating the change in hydrophobicity due to an increase in PDMS content. (a) PMMA, (b) 5wt% PDMS, (c) 8.6wt% PDMS, (d) 10wt% PDMS, (e) 15wt% PDMS, (f) 23wt% and (g) 34wt% PDMS.*

Figure 4.28 illustrates the relationship between contact angle and wt% PDMS incorporated for both the bulk polymer films and the electrospun fibers for the short series produced using two different tip-to-collectors distances. There is an increase in the contact angle as the wt% PDMS increases for both the polymer films and the nanofiber series. The increase in the contact angle for PDMS based copolymer films is a well known phenomena and the surface contact angle generally increases with the amount of PDMS since the PDMS component preferentially surface segregates. The surface segregation phenomena of PMDS is well documented in literature[18-20]. There is a remarkable increase in the SCA measurement of the nanofiber surfaces relative to the copolymer films. Both the nanofiber series show the property of superhydrophobicity with SCA greater than 150° especially for the higher content PDMS copolymers. It is also noted that the 20cm TCD series has higher overall SCA for a given wt% PDMS. This can be correlated to the overall smaller nanofiber diameters observed for the larger spinning distance.

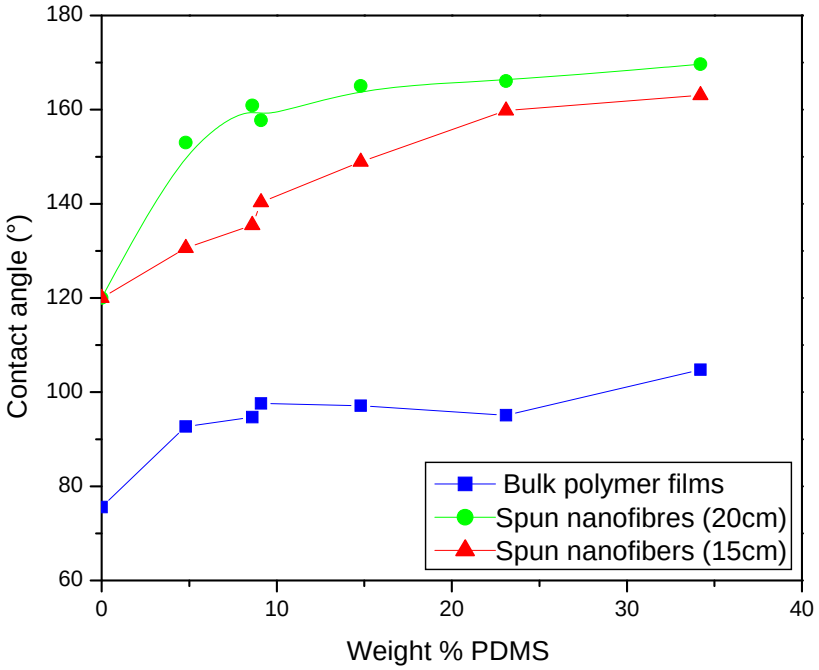

Figure 4.28 *Graph showing the difference in contact angle due to wt% PDMS and TCD*

Water repellency on solid materials has a chemical origin and is also influenced by the microtexture of the material. There are two possible origins for the effect of superhydrophobicity. Either the liquid follows the solid surface, or it leaves air inside the texture[21]. This additional influence of the air left inside the texture increases the contact angle and hence increases the hydrophobicity. In order to illustrate the effect of the "roughness" factor on the measured SCA, the following equation was used[22]:

$$\cos\theta_a = r\cos\theta_b \qquad (4.3)$$

where θ_a is the SCA of the nanofiber surface and θ_b is the SCA of the corresponding copolymer film, r is the "roughness factor".

Figure 4.29 shows the calculated "roughness factors" for each of the TCD series determined using Equation 4.3. This clearly illustrates the difference between the two TCD series. It is interesting to note that the calculated "roughness factor" appears to be larger for the higher wt% PDMS copolymer (meaning there is a higher difference between the SCA of the nanofibers and the corresponding polymer film with an increased PDMS wt%). This is also observed in Figure 4.28 where there is a stronger dependence on the PDMS wt% for the

nanofiber series than for the copolymer films. When the average fiber diameters of a given series are considered, there does not seem to be a direct correlation between the calculated roughness factor and the average fiber diameters. This implies that the observed "roughness factors" may not entirely be due to the fiber morphologies. When the copolymers are electrospun to form the nanofibers, the effective increase in the surface area magnifies the contribution of the PDMS components (which preferentially surface segregate) beyond that of copolymer films. This indicates that the electrospinning process is an effective means of producing "surfaces" of a progressively lower surface energy by variation of the PDMS wt%, whereas in the bulk films, the SCA reached a maximum more or less constant value at relatively lower PDMS content.

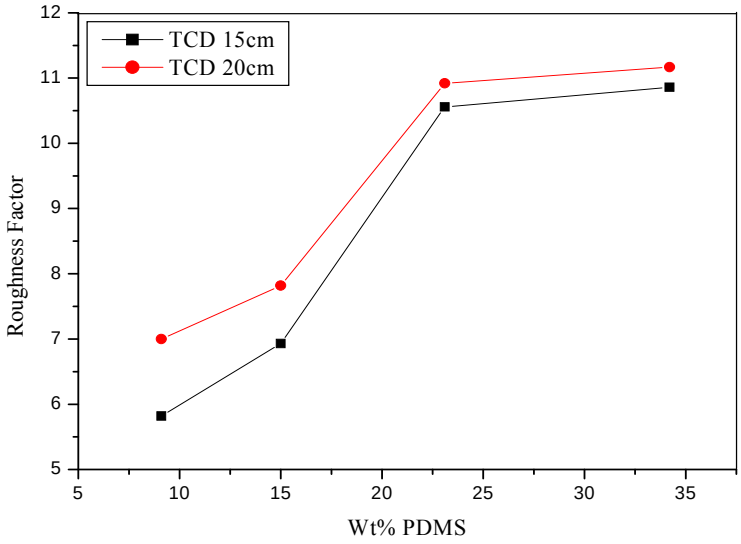

Figure 4.29 *Influence of Roughness factor on Contact Angles*

4.3.5. Surface modification by corona discharge

Several analytical methods were used to establish the effect as well as the extent to which high voltage corona discharge affected the degradation of the electrospun nanofibers. These techniques included Static Contact Angle measurements (SCA), SEM, TEM, Photo Acoustic Spectroscopy (PAS), ATR and Confocal Raman Spectroscopy. It was noticed early on that exposing the fibers to corona caused a dramatic decrease in hydrophobicity. This loss in hydrophobicity occurred as early as after just one minute of corona exposure. Hydrophobicity was, however, seen to increase with time after exposure in most samples, but this recovery was never 100%.

Figure 4.30 shows a series of images for a water drop in contact with a nanofiber surface directly after 30min of corona treatment. This series of images clearly shows the dramatic impact of the corona treatment on the surface properties. When the drop comes into contact with the surface, it immediately wets the surface within 3.5 seconds. This is in stark contrast to Figure 4.26 (g) which showed a superhydrophobic surface. Directly after corona treatment all the samples showed this phenomenon. These surfaces can be classified as superhydrophilic.

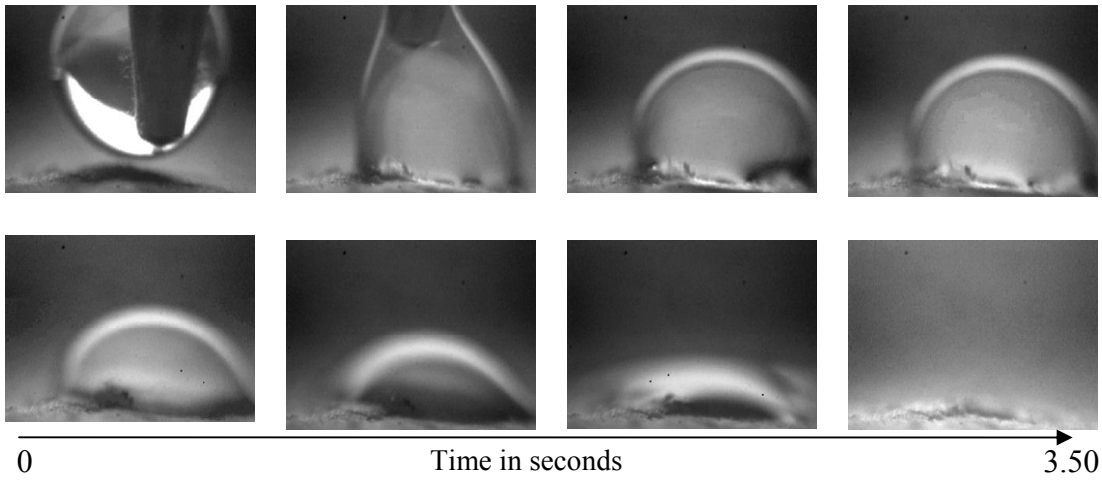

Figure 4.30 *Illustration of superhydrophillic nature of a 34wt% PDMS copolymer sample directly after 30min of exposure to corona discharge.*

Figures 4.31(a) and 4.31(b) show the SCA measurement of the surface as a function of the recovery time after corona exposure for different treatment times. It can be seen that samples show the phenomena of "hydrophobicity recovery" which is typically observed in pure cross-linked PDMS compounds after corona treatment. The data shows that the exposure time has a dramatic effect on the recovery rate. For the 34wt% PDMS sample exposed to 2-10min of corona there is a rapid recovery in the first minutes after treatment. Recovery continues for approximately 2h30min until the maximum SCA values is reached. This maximum value does not however return to 100% of the initial SCA value before treatment, and these surfaces cannot be considered to be superhydrophobic (SCA $<150^{o}$). With an increasingly longer corona treatment time, the rate of recovery is considerably slower. The 30 min corona treated samples shows no hydrophobicity recovery in any of the samples. The sample exposed to corona discharge for 20min takes approximately 12hours to recover to its maximum value vs. the 2h30min for other samples. Studies were also done on samples with a much lower 8.6wt% PDMS. These samples show the same general recovery trend, but over a much longer

time period. This is most probably due to the lower PDMS content which would result in the generation of fewer low molecular weight PDMS species which are most likely responsible for the hydrophobicity recovery. The change from superhydrophobic (contact angle of more than 150^{o}) to superhydrophillic (complete absorption of the liquid) was seen in all copolymer samples after exposure to high voltage corona discharge.

Although the hydrophobicity recovery of PDMS materials is well documented, this is one of the first examples of hydrophobicity recovery in PDMS containing organic-inorganic hybrid materials.

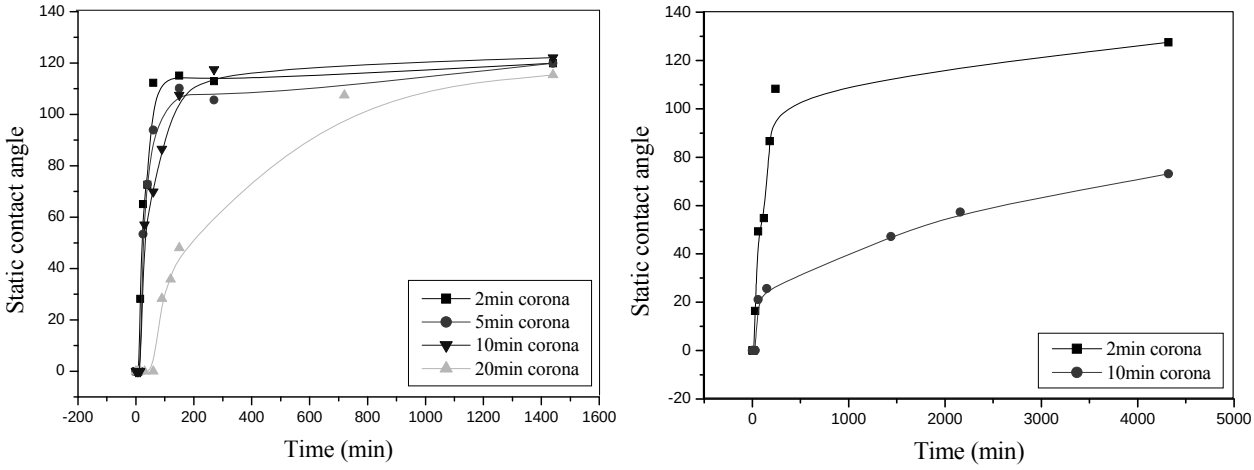

Figure 4.31 H*ydrophobicity recovery of a 34wt% PDMS sample (a) and hydrophobicity recovery of a 8.6wt% PDMS sample (b).*

The recovery of hydrophobicity in pure PDMS materials is well documented in literature and the main mechanism for this can be explained when looking at the migration of low molecular mass molecules within the polymer matrix[23-26]. These low molecular weight components are present due to incomplete curing, the addition of silicone liquids as processing aids and ultra-violet (UV) and partial discharge induced[24, 27]. In the case of the electrospun nanofibers the low molecular weight species are produced *"in situ"* during the corona treatment. It was found that in pure PDMS compounds prolonged exposure to corona discharge results in the formation of a thin wettable and brittle silica layer on the surface[28]. It was also found that stresses induced thermally or mechanically lead to the cracking of the brittle silica-rich layer. This enables the transport of low molecular mass PDMS components to migrate to the surface and thereby leading to more rapid hydrophobicity recovery.

Figure 4.32 (a-f) shows examples of the SEM images of the nanofiber surfaces after 30min of corona exposure. It is clear that the exposure to corona discharge has a dramatic effect on the overall surface morphology as well as the morphology of individual fibers (as illustrated by Figure c and e). It can be seen that the breakage of fibers is a common occurrence, and in severe cases (like that of prolonged exposure) breakage of fibers is so extreme that holes form within the fiber mesh. In certain cases fibers are also fused together, thereby decreasing the overall surface roughness. These effects are permanent and are a possible cause for the incomplete recovery in hydrophobicity. It was shown earlier that the surface roughness plays a large role in the formation of superhydrophobic surfaces and this loss in surface roughness due to the fusion or melting together of fibers is a further reason for the loss in hydrophobicity. Another phenomenon that can be seen in the SEM images is the roughness of the individual fibers after corona treatment. This may be due to the cracking of the silica rich layer that forms after exposure. This is clearly seen in Figure 4.32 (c) and (e).

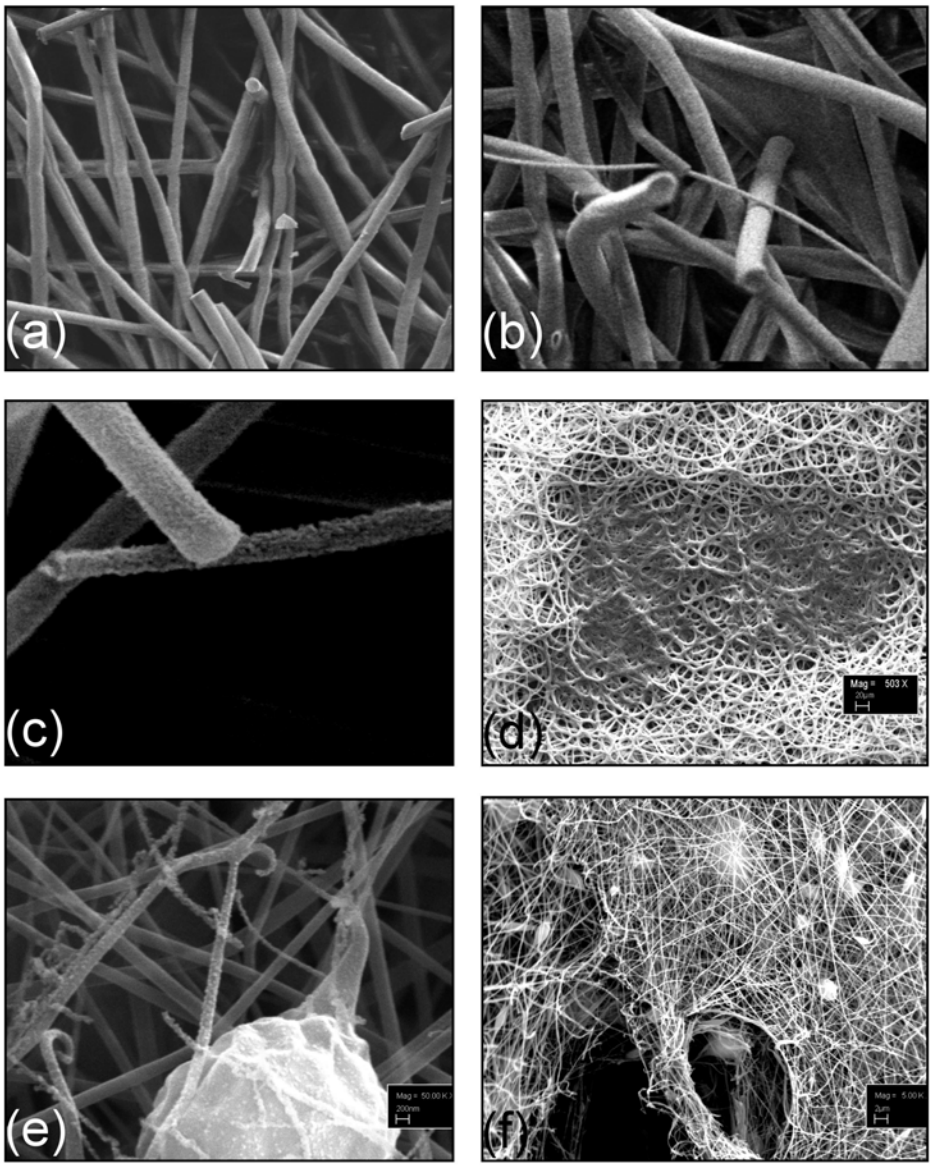

Figure 4.32 *SEM images illustrating the different effects of corona treatment on fiber morphology. Images (a), (b), (c) and (f) show permanent fiber breakage and the formation of holes in the fiber mesh. Image (d) shows the fusion of fibers leading to an overall decrease in surface roughness and image (c) and (e) show the rough nature of individual fibers not seen prior to corona treatment.*

Photo Acoustic Spectroscopy (PAS-FTIR) and Attenuated Total Reflectance (ATR-FTIR) analysis was done on the modified fibers to further examine any changes in the fibers after corona exposure. Figure 4.33 shows the PAS-FTIR spectra of the 34wt% PDMS nanofibers before and after corona treatment.

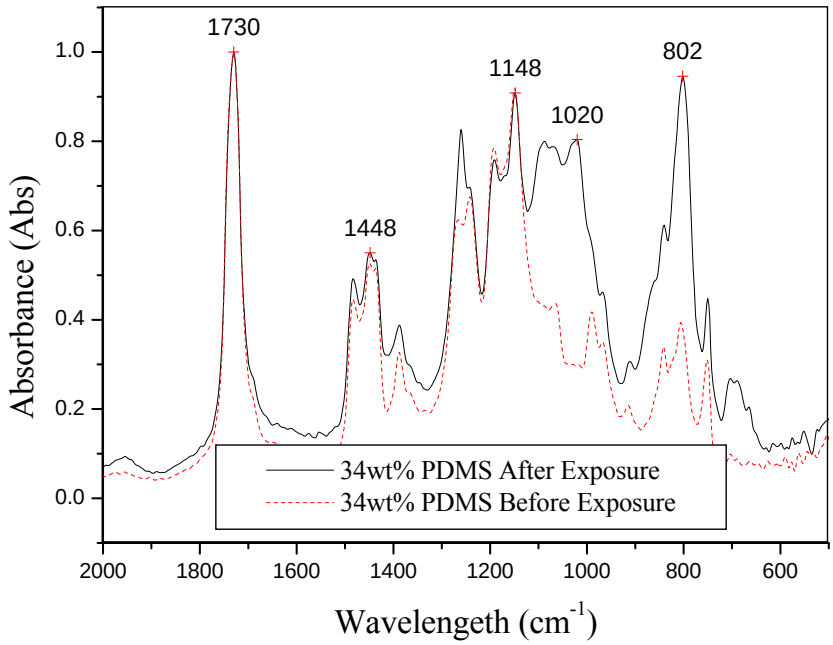

Figure 4.33 *PAS-FTIR Spectra of PMMA-g-PDMS (34wt% PDMS) nanofibers before and after exposure to corona.*

According to literature the peaks found at 1000 to 1100cm^{-1} and ~800cm^{-1} corresponds to Si-O-Si component of the graft copolymer. It can also be seen then that these peaks increase directly after exposure to corona. This is most likely due to the formation of a silica rich layer very close to the surface. This phenomenon can also be seen by looking at the Si-O-Si peaks on the ATR-FTIR spectra seen below for a 23wt% PDMS sample in Figure 4.34

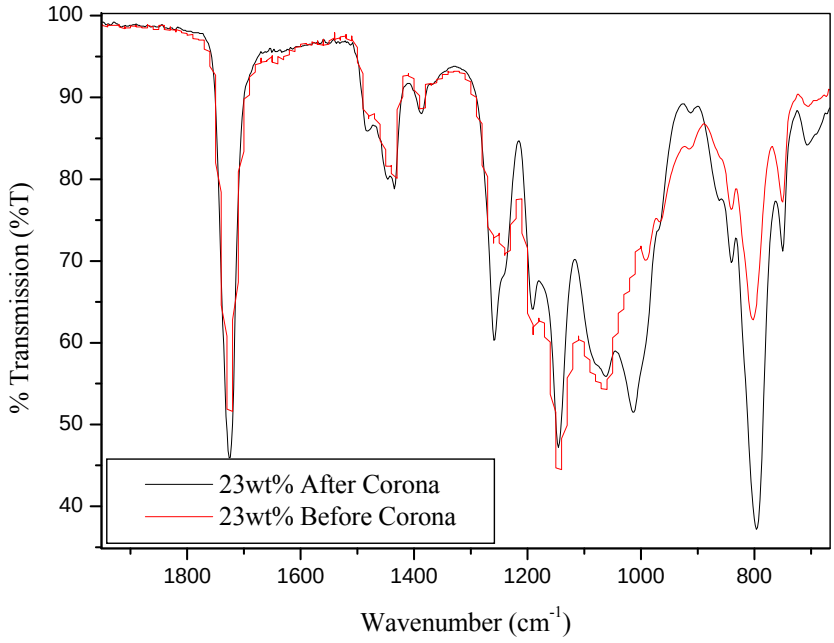

Figure 4.34 *ATR Spectra before and after exposure to corona of a 23wt% PDMS sample*

The effect of exposure to corona discharge was further investigated by making use of Confocal Raman Spectroscopy on the individual fibers. The Si-O peak at 550 to 450cm^{-1} and the symmetric CH_3 stretching peak at 2960cm^{-1} was used to determine the ratio of Si-O to C-CH_3 prior to exposure and then again after exposure. Figure 4.35 shows the Raman spectrum of the Si-O and CH_3 stretching region of the spectra for the 34wt% sample before and after corona treatment (30 minutes).

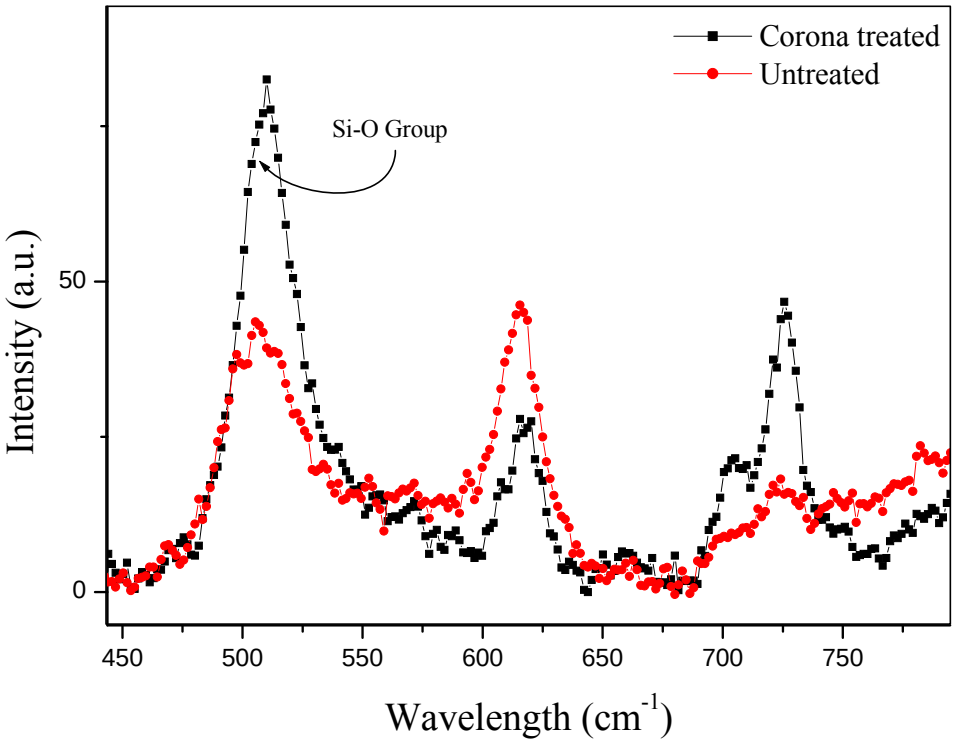

Figure 4.35 *Confocal Raman Spectra showing the difference in a 34wt% PDMS corona treated and untreated sample.*

Figure 4.36 shows the Si-O/CCH_3 ratio vs. the wt% PDMS of nanofiber samples. In all cases the samples show an increase in the Si-O/C-CH_3 ratio after corona exposure. This is consistent with the formation of a brittle silica like layer that is observed in the SEM images and is similar to the degradation layer that is formed in pure PDMS compounds after corona exposure.

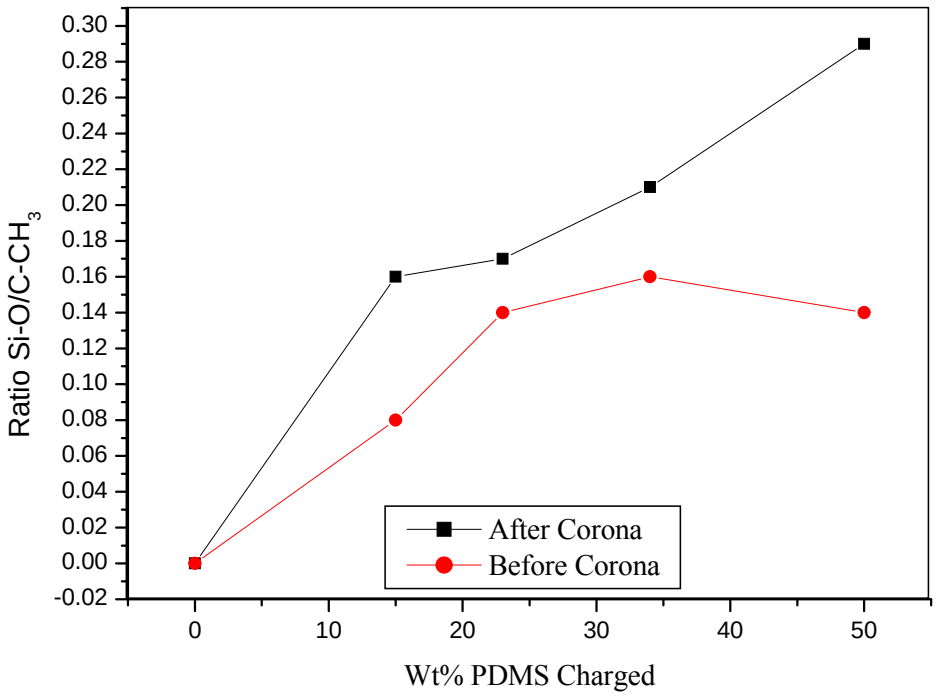

Figure 4.36 *Confocal Raman Spectroscopy showing the increase in the Si-O content after exposure to corona discharge. This indicates the formation of a silica layer at the surface of the nanofibers. The samples used were all spun at 10kV and at 15cm*

In order to study the effects of corona treatment further, the corona treated nanofibers where dissolved in THF. It was noted that after corona treatment the samples where insoluble, indicating that a crosslinking reaction had taken place. Figure 4.37 shows the relationship between the volume fraction polymer in the swollen state (or Vr) and the corona treatment time. There is an initial increase in the crosslinking density at shorter treatment times and then a progressive decrease at higher treatment times.

The results of the crosslink density experiments and the SCA recovery data indicate that after prolonged exposure to corona (>30min) degradation of the polymer has occurred to such an extent that no low molecular weight components exists to aid in the recovery.

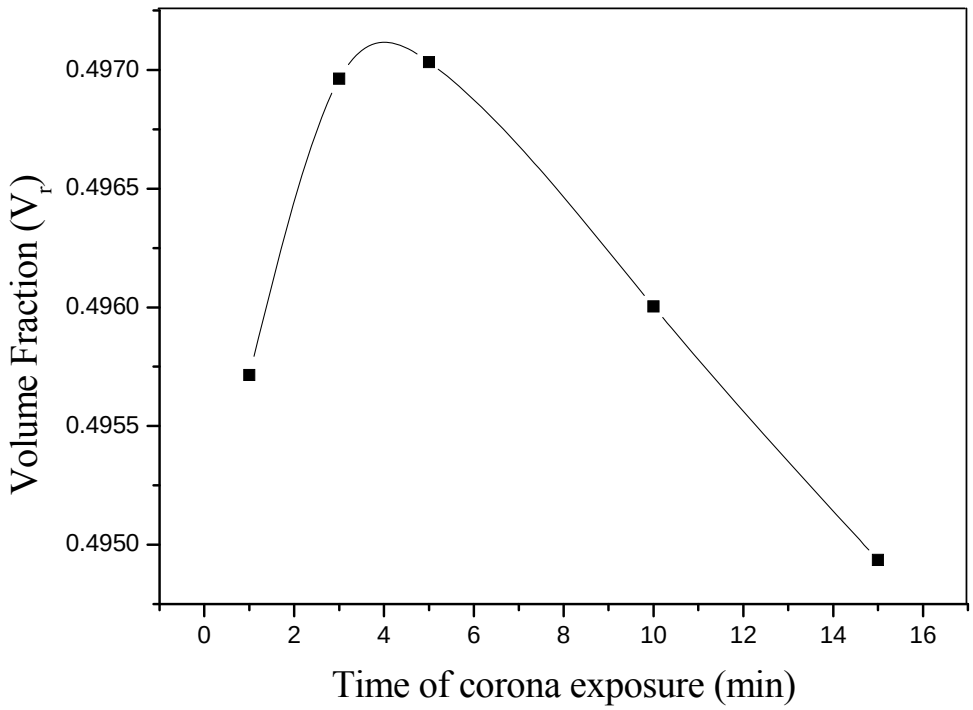

Figure 4.37 *Volume fraction polymer in the swollen state (V_r) for different corona exposure times*

SEM was also used to determine if the de-swollen residual polymer retained some of its fiber structure. As can be seen by looking at Figure 4.38 (c), (d) and (h), this was indeed the case. Figure 4.38 shows the SEM images for the de-swelled samples after the crosslink density determinations. It can be seen that after the swelling experiment some of the fiber structure is maintained.

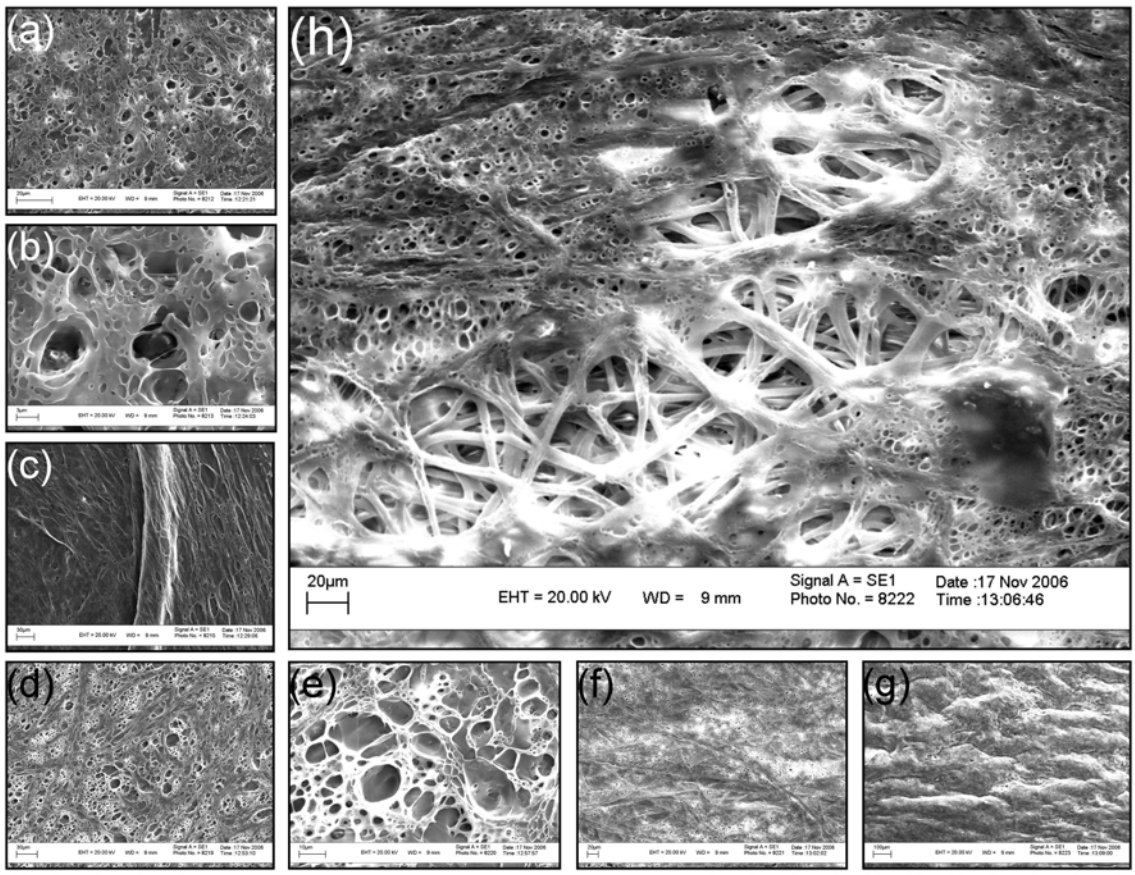

Figure 4.38 *SEM images of deswelled nanofibers after crosslinking determination.(a-c) 5min corona exposure, (d-e) 10min corona exposure and (f-h) 15min corona exposure*

To summarize then, corona discharge causes a large amount of surface degradation, formation of a silica rich layer on the surface of the nanofibers after exposure to high voltage corona discharge, a decrease in the surface roughness (partly due to fiber meltage) as well as crosslinking.

4.4. Self-reinforced silicone elastomer composites

4.4.1. Introduction

It is well known in literature that non-fibrous inorganic fillers like glass beads, calcite and talc, are often added to polymers (most often thermoplastics) to reduce cost. The incorporation of these particles into the matrix also often leads to an improvement of the mechanical properties. Short glass or carbon fibers are extensively used in engineering applications to enhance the performance of the materials. Reinforcement through the use of

particles or fibers can be achieved by conventional methods such as extrusion compounding and injection molding. These techniques, however, are mostly used for thermoplastics. The advantages of making use of hybrid materials instead of single individual materials are also discussed in literature[29, 30]. In this study we looked at the incorporation of nanofiber hybrid materials into a silicone elastomer (to create a reinforced composite) and its effect on the mechanical properties of the composite. Herein follows a description of the type of hybrid nanofibers used, the means by which they were created, the procedure for making the elastomer composites as well as the preliminary results of the physical testing. This project is limited to the preparation and evaluation of layered composite materials prepared directly by using the non-woven fibers produced during electrospinning.

4.4.2. Development of method for producing composites

The procedure for preparing the silicone matrix is as follows: 0.13g of Crosslinker V24 is added to 5g of Dehesive 920 silicone. The solution is then stirred with a glass rod. 0.05g of Catalyst C 05 is then added and the solution is again stirred vigorously. The process for the making the composites (or laminates) can then be followed as depicted in Figure 4.40. First a layer of Silicone matrix is placed on a piece of non-stick Teflon ®. This is then placed under vacuum to remove any air bubbles trapped inside. After this first step a pre-cut piece of nanofiber mesh is gently placed on top of the silicone layer and allowed to become completely wetted. It is then again placed under vacuum to remove air. In step 3 more silicone is placed on top of the fiber mesh to ensure complete coverage. The Teflon® mat is then placed in an oven and left to cure for 60min at 120^{o}C. The images in Figure 4.39 also illustrate the vacuum setup as well as the formation of trapped air bubbles inside the system. The nanofiber meshes were collected directly on the surface of a aluminium pan filled with water. This facilitated the collection of uniform pieces of the nanofibers. The amount of material (polymer in solution) used in the preparation of the nanofibers meshes was kept constant in an effort to ensure better uniformity between each mesh sample.

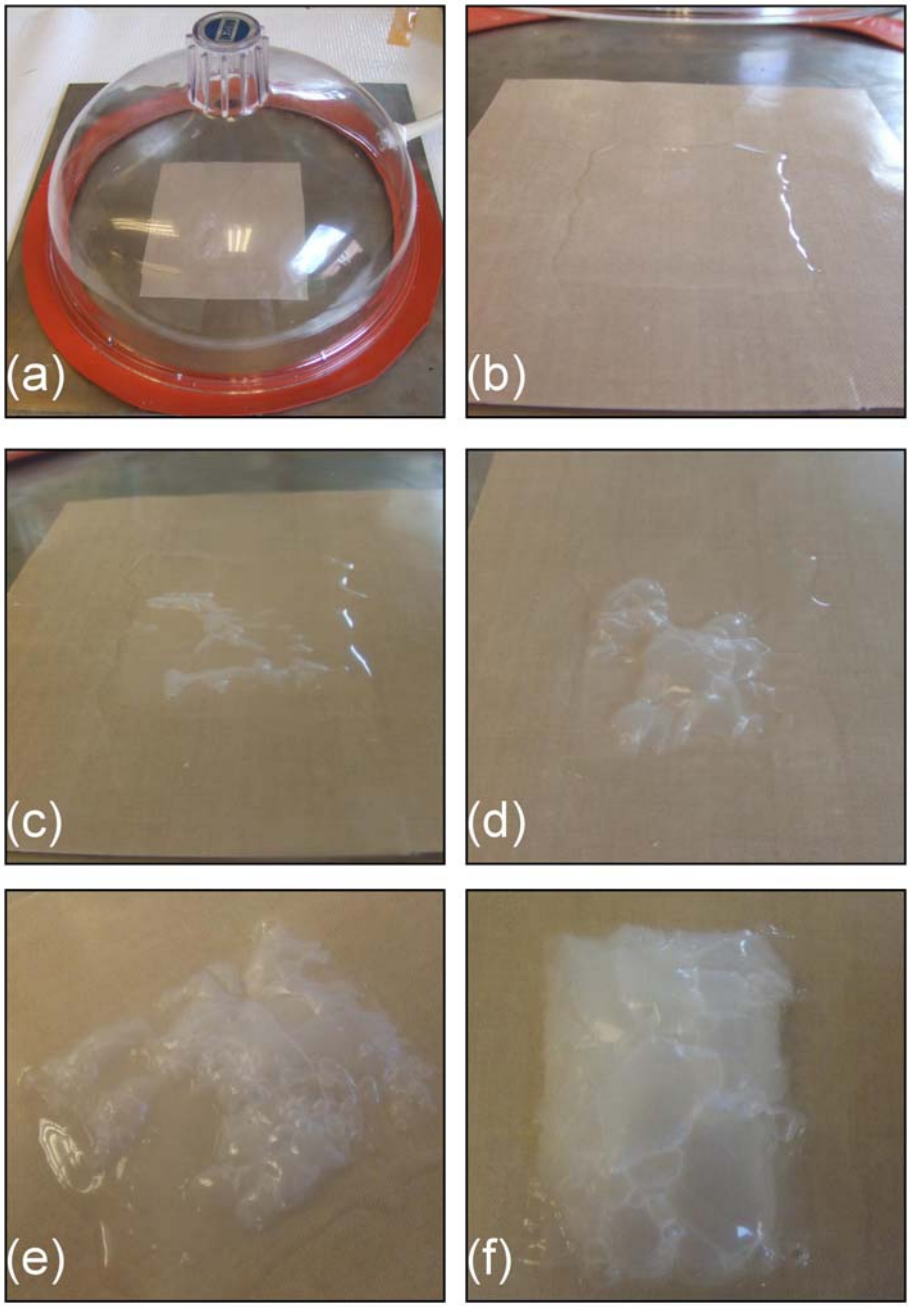

Figure 4.39 *Images showing the formation of air bubbles trapped inside the layers and fibers after removal of air under vacuum.*

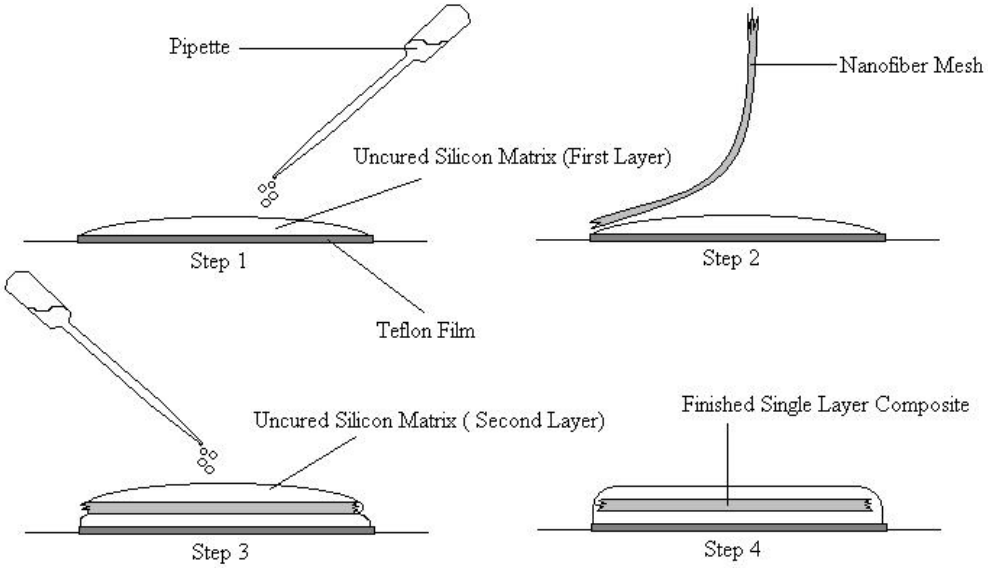

Figure 4.40 *Description of the experimental procedure used to produce the silicon composites*

4.4.3. Morphology

The morphology of the prepared laminates/composites was investigated by making use of Scanning Electron Microscopy (SEM). Cross sections were obtained and used to establish the distribution of the fibers throughout the silicone matrix. This was done in two ways. The first involved the cutting of the composite with a scalpel to obtain a cross sectional area. The second set of cross sections was obtained by cryo-fracturing the silicone composites. Cryo-fracturing was done by placing the composite material in liquid nitrogen. This ensured that the material froze rapidly below its T_g. The material was then removed and fractured immediately while the temperature was still well below the T_g. Figures 4.41, 4.42 and 4.43 show the SEM images of the cross-sections of the composites. It can be seen from this series of images that the fibers are remarkably well distributed within the silicone matrix. These images represent PDMS matrixes reinforced with 23wt %, 34wt % and 50wt% PDMS nanofiber systems respectively. The remarkably good distribution of the fibers is important since one of the main challenges in using nano-scale fillers is the good distribution of the fillers in the matrix. In this case it appears as if the PDMS component in the nanofibers promotes the compatibility with the matrix ensuring a even distribution of the fibers. This result is extremely important for the reason that this will ensure that when strain is placed on the composite that it will be evenly distributed throughout.

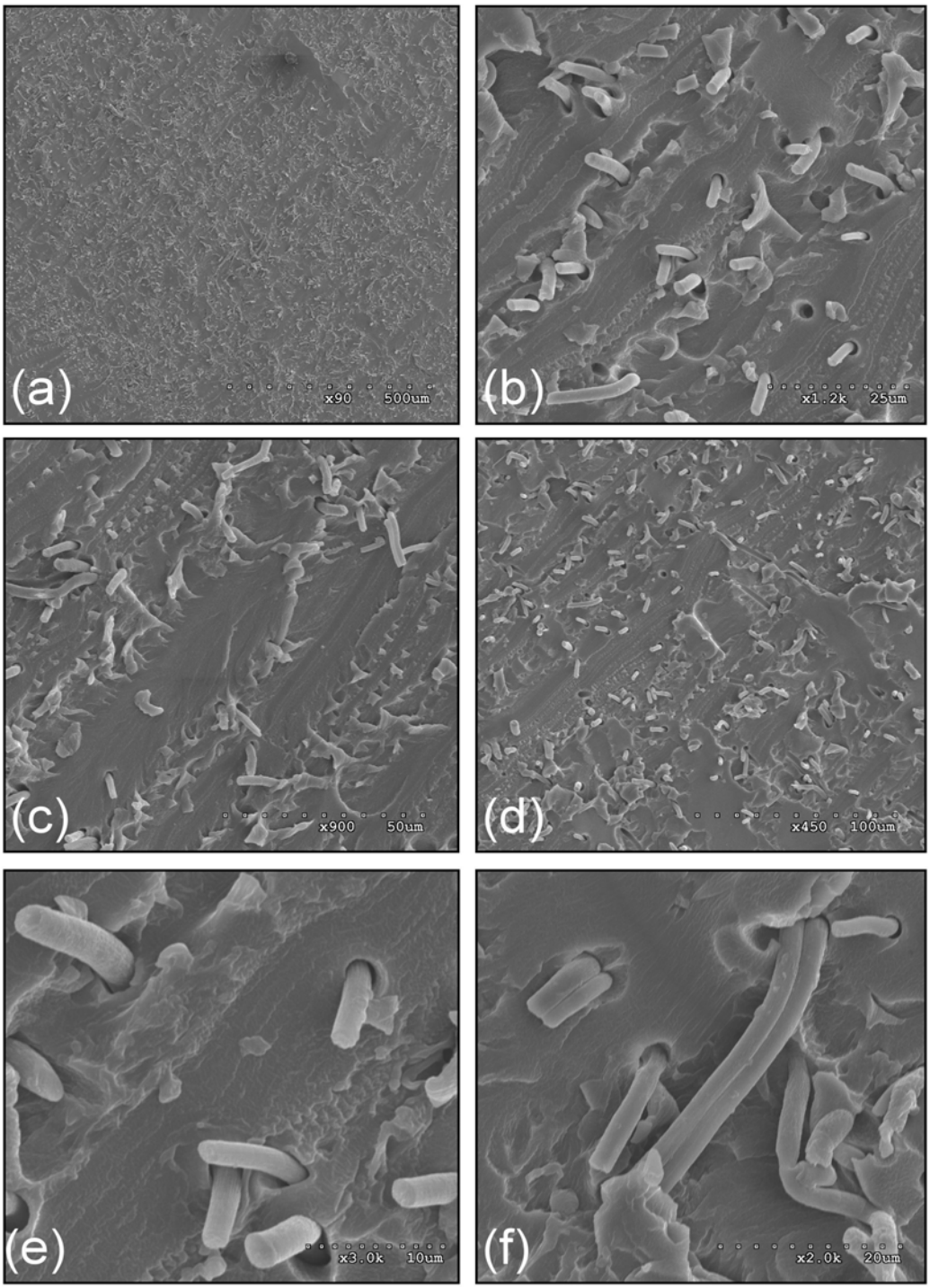

Figure 4.41 *Cross sectional SEM images of a silicone elastomer composite reinforced with a 23wt% PDMS hybrid nanofiber system.*

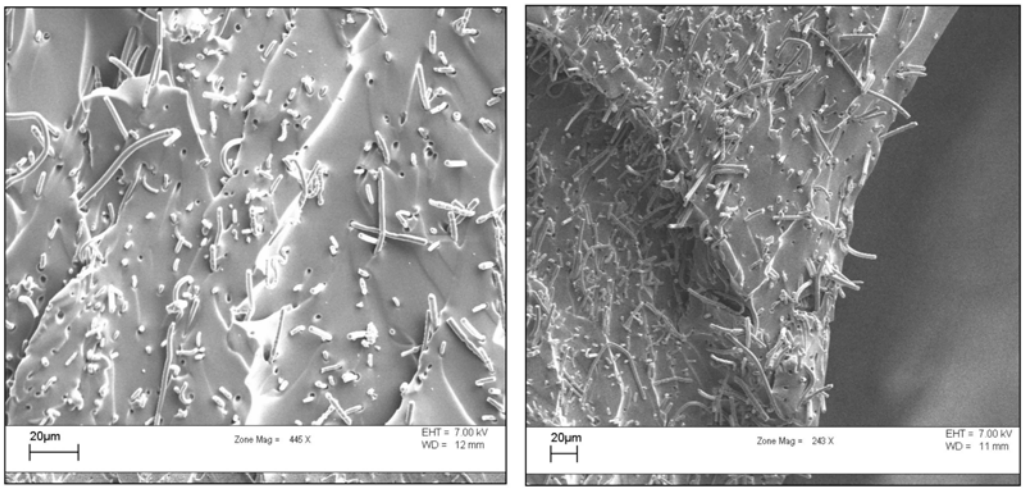

Figure 4.42 *Cross sectional SEM images of a silicone elastomer composite reinforced with a 34wt% PDMS hybrid nanofiber system.*

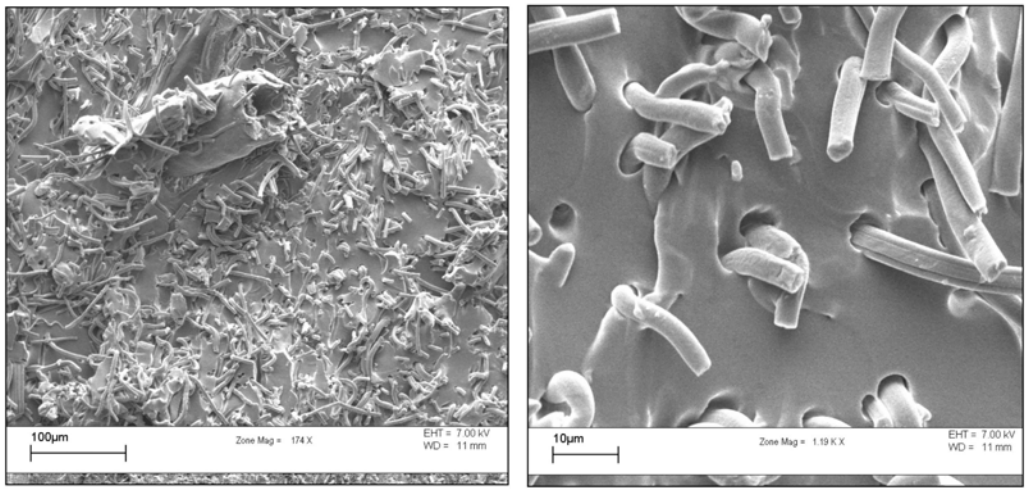

Figure 4.43 *Cross sectional SEM images of a Silicone Elastomer Composite reinforced with a 50wt% PDMS hybrid nanofiber system*

Figure 4.44 below shows examples of cross-sectional SEM images after cryo-fracturing. It can once again be seen that the fibers are well distributed in the PDMS matrix. Cryo-fracturing however shows a lot more fiber breakage (as expected) and a lot less fiber "pull-out". Fibers are broken much cleaner and more evenly (as seen in Figure (b) and (d)).

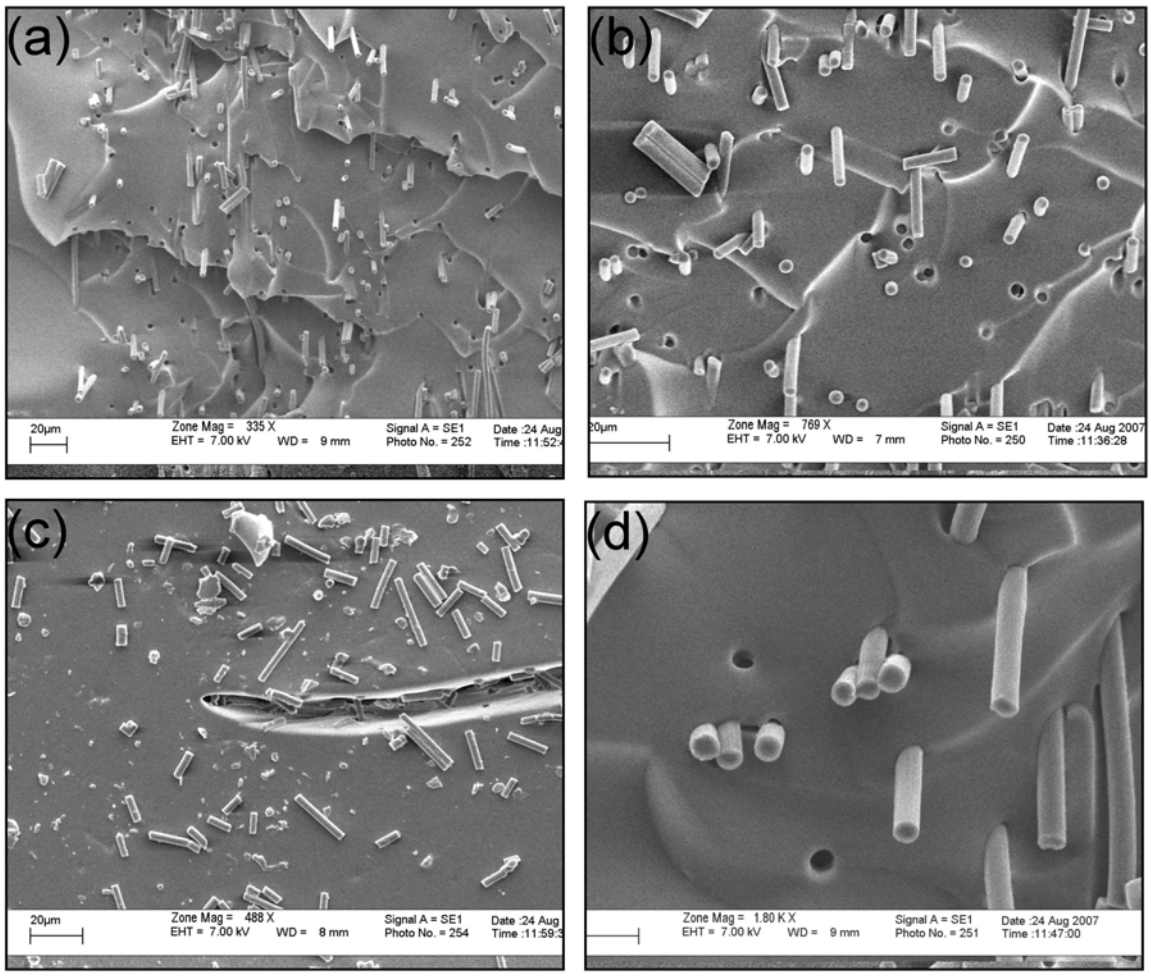

Figure 4.44 *SEM images illustrating cross-sectional areas of cryo-fractured silicone composites. All Figures are of a 34wt% multi layer composite.*

Figure 4.45 shows the Raman spectra of the 34wt% composite. The confocal Raman spectra obtained show clear differences between the prepared composite materials and the pure Dehesive 920 silicone. These spectra were obtained by focusing on individual fibers through the silicone matrix. In Figure 4.45 below it can be seen that there is a definite CH_3-C peak at 600cm^{-1} (due to the PMMA component of the nanofibers) in the composite material and not in the pure silicone (as expected). Also seen in Figure 4.45 is the C=O carbonyl peak at 1725cm^{-1} due to the PMMA component of the nanofibers. This result leads to several very interesting possibilities for future work. It shows that confocal Raman can focus through the matrix onto the distributed fibers. As the confocal Raman spectrometer can be fitted with a tensiometer, real time data can be collected on the individual fibers in the PDMS matrix when they are placed under strain. The spectrometer is also fitted with a real time camera and by focusing on an individual fiber in the matrix the time and strain at which necking or yielding occurs (like that seen in Figure 4.50) can also be established.

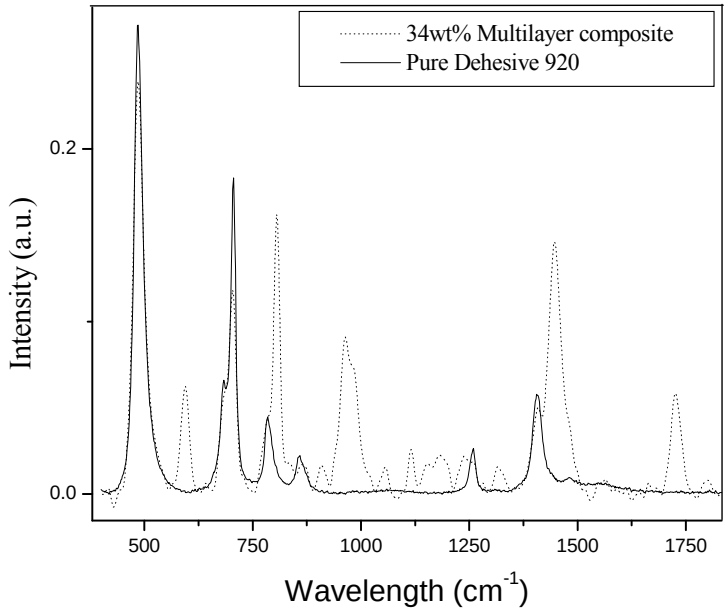

Figure 4.45 *Confocal Raman Spectra showing the difference between a pure Dehesive 920 Silicone elastomer and a nanofiber reinforced composite*

4.4.4. Mechanical properties

The prepared laminates were tested using a standard tensile test. The prepared composites were cut to form 3 identical pieces from each reinforced composite material. This ensured that tests were done on uniform materials and also ensured reproducibility. The tensile test strip had dimensions of 12.5mm in width, 40mm in height and between 1 and 1.5mm thick. Exactly 10mm on each side was used to clamp the specimen in place. Figure 4.45 (a) below shows a pure (non-reinforced) silicone specimen whereas Figure 4.45 (b) shows a multi-fiber composite secured in the tensile tester. Figure 4.46 (c) shows detailed schematic of the test strips prepared including the dimensions that were used.

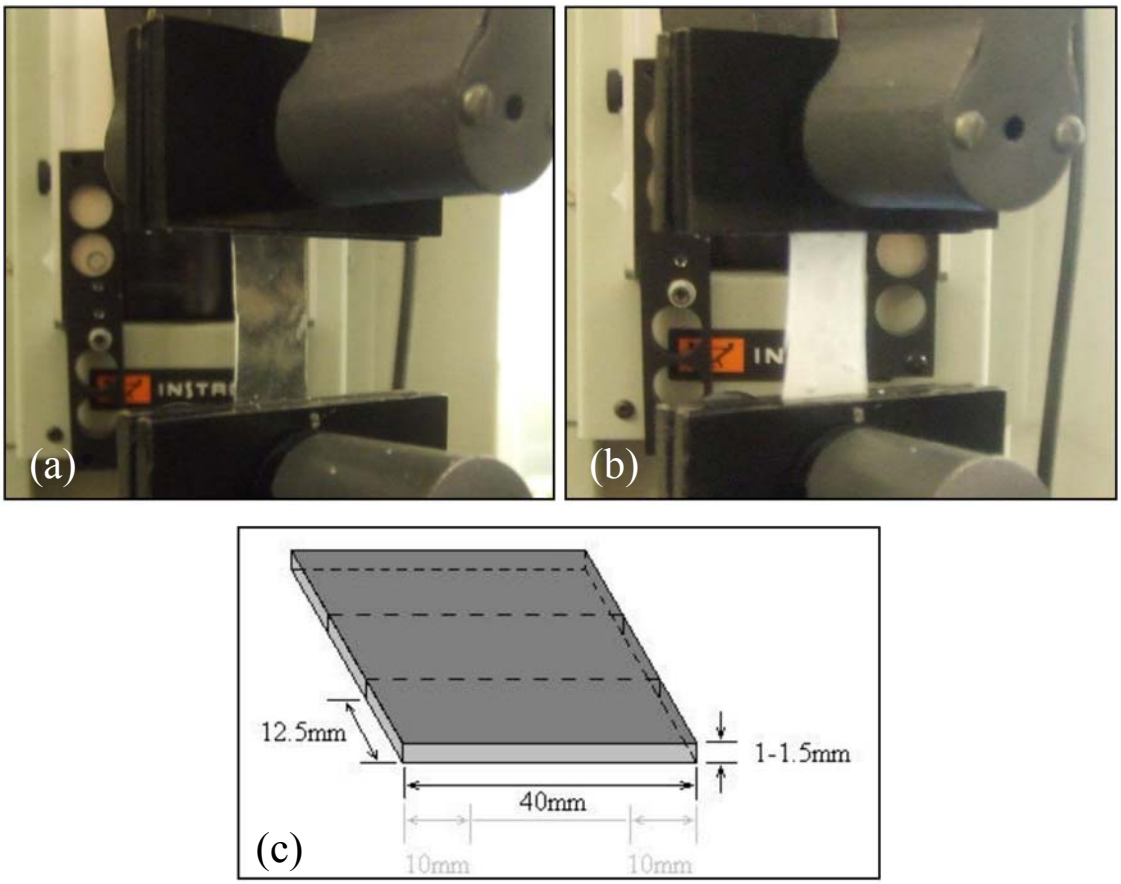

Figure 4.46 *Images showing tensile testing to establish the mechanical properties of the material. (a) Pure silicone (Dehesive 920), (b) Multi-fiber reinforced material and (c) Dimensions of prepared test strips.*

Figure 4.47 shows the energy at break for the single, double and multilayer (3 layers) composites. Figure 4.48 shows the tensile strength at maximum load for the same series. A summary of the tensile data is given in Table 4.6 and table 4.7 contains the standard deviation data.

Mechanical data obtained by tensile testing clearly proves the reinforcing effect of the nanofibers. Figures 4.47 and 4.48 show that the energy at break in the material increases with increasing wt% PDMS nanofibers used as well with increasing layers used. The increase in the energy needed to break the multi layered composite increases dramatically with increasing wt% PDMS nanofibers used. The same result is evident with the tensile strain at maximum load.

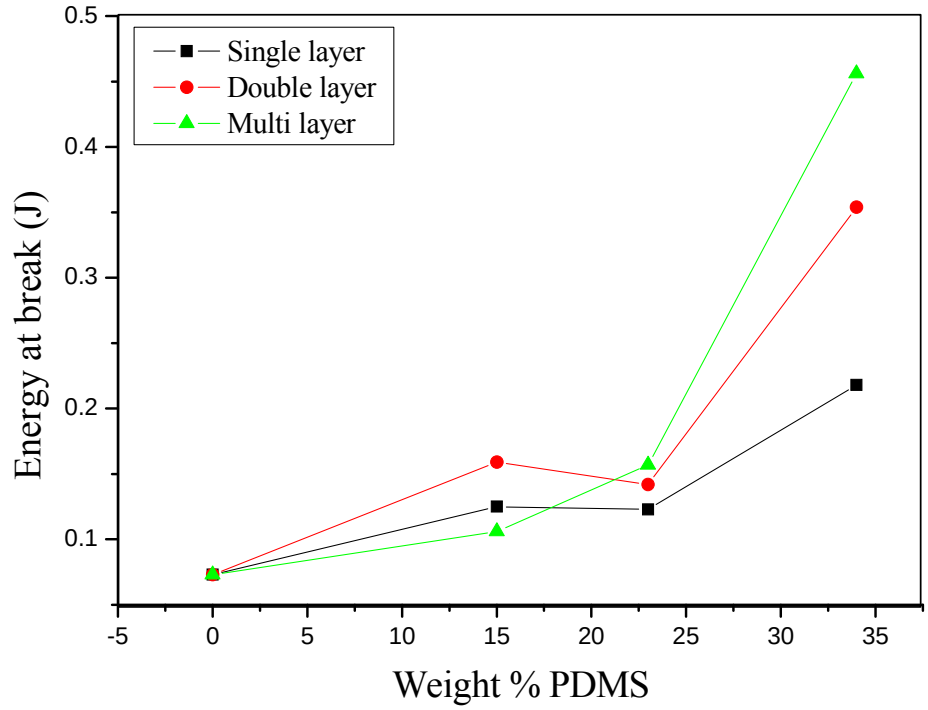

Figure 4.47 *Graph illustrating the increase in the energy at break with an increase of wt% PDMS samples used*

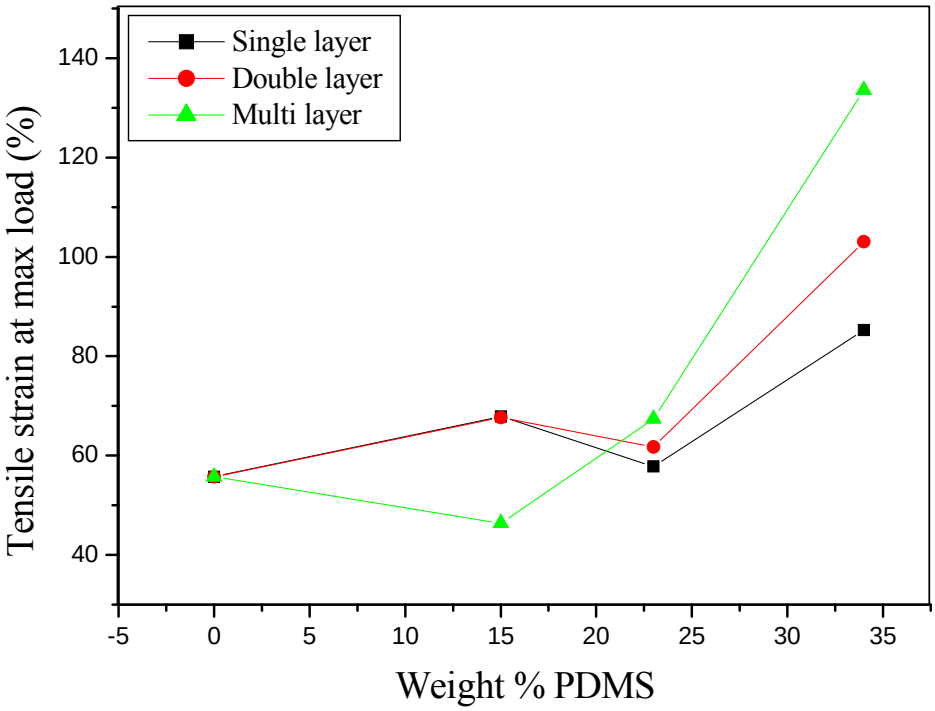

Figure 4.48 *Graph illustrating the increase in tensile strain at break at maximum load with an increase of wt% PDMS samples used.*

Table 4.6 below gives a summary of the average values obtained for multiple tensile tests with samples varying in the number of layers used, as well as the wt% PDMS nanofibers used to produce the composite. Where MS15, MS23 and MS34 represent 15wt%, 23wt% and 34wt% PDMS copolymer nanofibers systems used in the composite respectively. Single, double and multilayer indicates the amount of nanofiber layers (meshes) used in the composite.

Table 4.6
Mechanical properties of PMMA-g-PDMS Nanofiber Reinforced Silicon Composites

Sample ID	Maximum Load (N)	Tensile stress at max load (Mpa)	Tensile strain at max load (%)	Tensile stress at break (Mpa)	Load at break (N)	Tensile strain at break (%)	Energy at Break (J)	Energy at Max (J)
Dehesive 920	8.0175	0.56	55.74	0.33	4.685	60.36	0.073135	0.068775
MS15 Single Layer	12.24	0.977	67.903	0.49	6.1	71.313	0.125	0.121
MS15 Double Layer	14.677	1.173	67.647	0.49	6.107	71.807	0.159	0.154
MS15 Multi Layer	16.65	0.863	46.383	0.31	6.1	50.34	0.106	0.101
MS23 Single Layer	11.85	0.947	57.831	0.38	4.69	61.386	0.123	0.12
MS23 Double Layer	15.271	1.132	61.725	0.347	5.316	65.647	0.142	0.138
MS23 Multi Layer	14.813	1.18	67.349	0.37	4.67	72.316	0.157	0.15
MS34 Single Layer	19.486	1.552	85.218	0.466	5.484	81.007	0.218	0.214
MS34 Double Layer	23.036	0.832	103.044	0.196	5.514	107.6	0.354	0.348
MS34 Multi Layer	21.865	1.02	133.563	0.235	4.67	137.793	0.456	0.452

Table 4.7 below gives a summary of the standard deviation for each sample.

Table 4.7
Summary of the standard deviation in each composite material tested.

Sample ID	Maximum Load (N)	Tensile stress at max load (Mpa)	Tensile strain at max load (%)	Tensile stress at break (Mpa)	Load at break (N)	Tensile strain at break (%)	Energy at Break (J)	Energy at Max load (J)
Dehesive 920	0.62	0.06	20.52	0.09	0.01	21.49	0.03	0.02
MS15 Single Layer	0.754	0.064	6.064	0.000	0.010	6.473	0.012	0.012
MS15 Double Layer	0.725	0.061	6.917	0.000	0.006	7.023	0.020	0.021
MS15 Multi Layer	0.67	0.46	3.15	0.16	0.00	3.33	0.01	0.01
MS23 Single Layer	0.44	0.04	3.89	0.00	0.00	3.94	0.00	0.00
MS23 Double Layer	1.61	0.13	14.26	0.01	0.00	14.08	0.04	0.04
MS23 Multi Layer	1.54	0.12	14.51	0.00	0.00	14.62	0.05	0.05
MS34 Single Layer	5.68	0.41	21.00	0.05	0.76	22.01	0.11	0.11
MS34 Double Layer	2.058	0.130	31.931	0.005	0.775	30.343	0.136	0.140
MS34 Multi Layer	5.88	0.17	32.67	0.09	0.00	32.74	0.21	0.21

Figures 4.49, 4.50 and 4.51 show the SEM images of the fractured surfaces of the laminates after the tensile testing. Here it is clear that the fibers are responsible for carrying some of the

load once put under stress. Fiber "pull-out" and fibers breaking cleanly are clearly evident in all samples tested (15wt %, 23wt % and 34wt %). Initiation of the fracture is not clear and does not seem to originate from the fibers or immediately adjacent to the fibers. The 34wt% PDMS sample shows a very interesting phenomenon. Figure 4.51 (d-f)) shows "necking" or yielding of the fibers in the matrix. This indicates that after the silicone matrix failed when stress was applied that the fibers continued carrying load leading to the fact that additional force was required to break the material after the silicone matrix failed. The phenomenon is only seen for the 23 and 34wt% samples and not for the lower wt% PDMS samples. When correlating these findings with the data collected during tensile testing, this result can explain the reason why the 34wt% samples showed such a remarkably higher energy at break. The reason why this only occurs in the higher wt% PDMS samples can be due to the fact that the higher (34wt % and to a lesser extent the 23wt%) PDMS samples have much better interaction/adhesion with the matrix. This leads to the fact that after the silicone matrix fails the fibers are still embedded firmly in the matrix and all strain is then transferred to the fibers. Fibers then yield and eventually break or pull out.

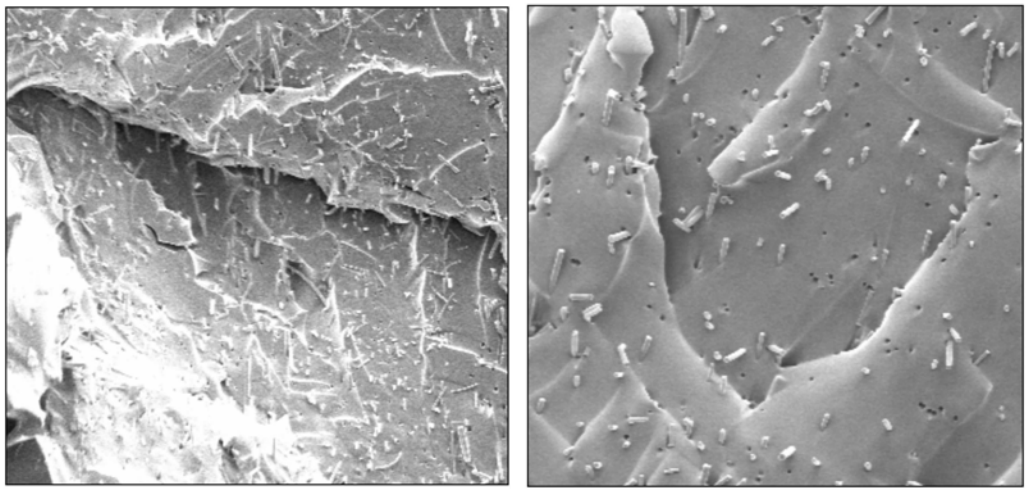

Figure 4.49 *SEM images of a 23wt% fractured composite*

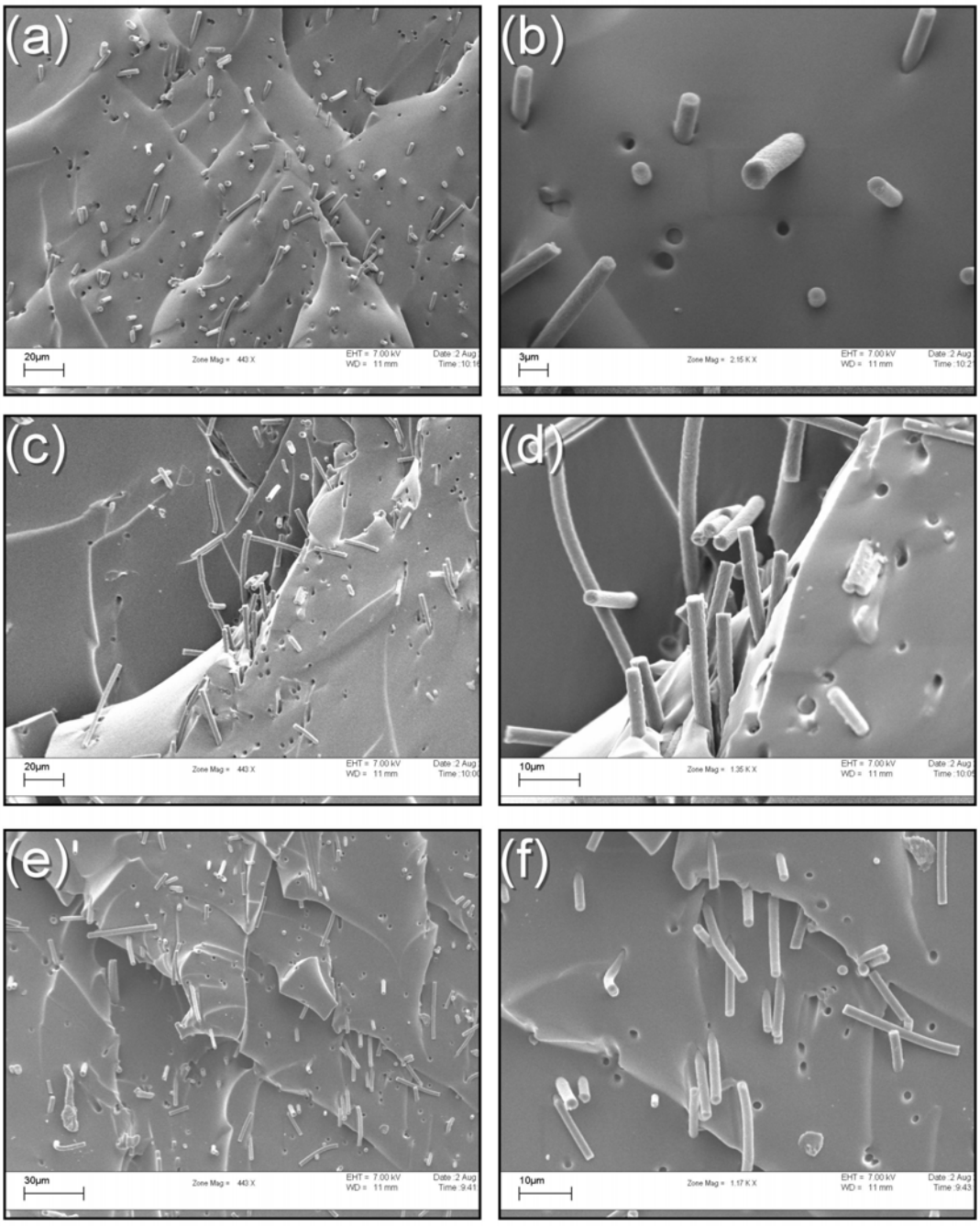

Figure 4.50 *SEM images of a 23wt% fractured composite. Figures (a) and (b) shows fractured surfaces of single layer composites, Figures (c) and (d) of double layer composites and Figures (e) and (f) of multi-layer composites*

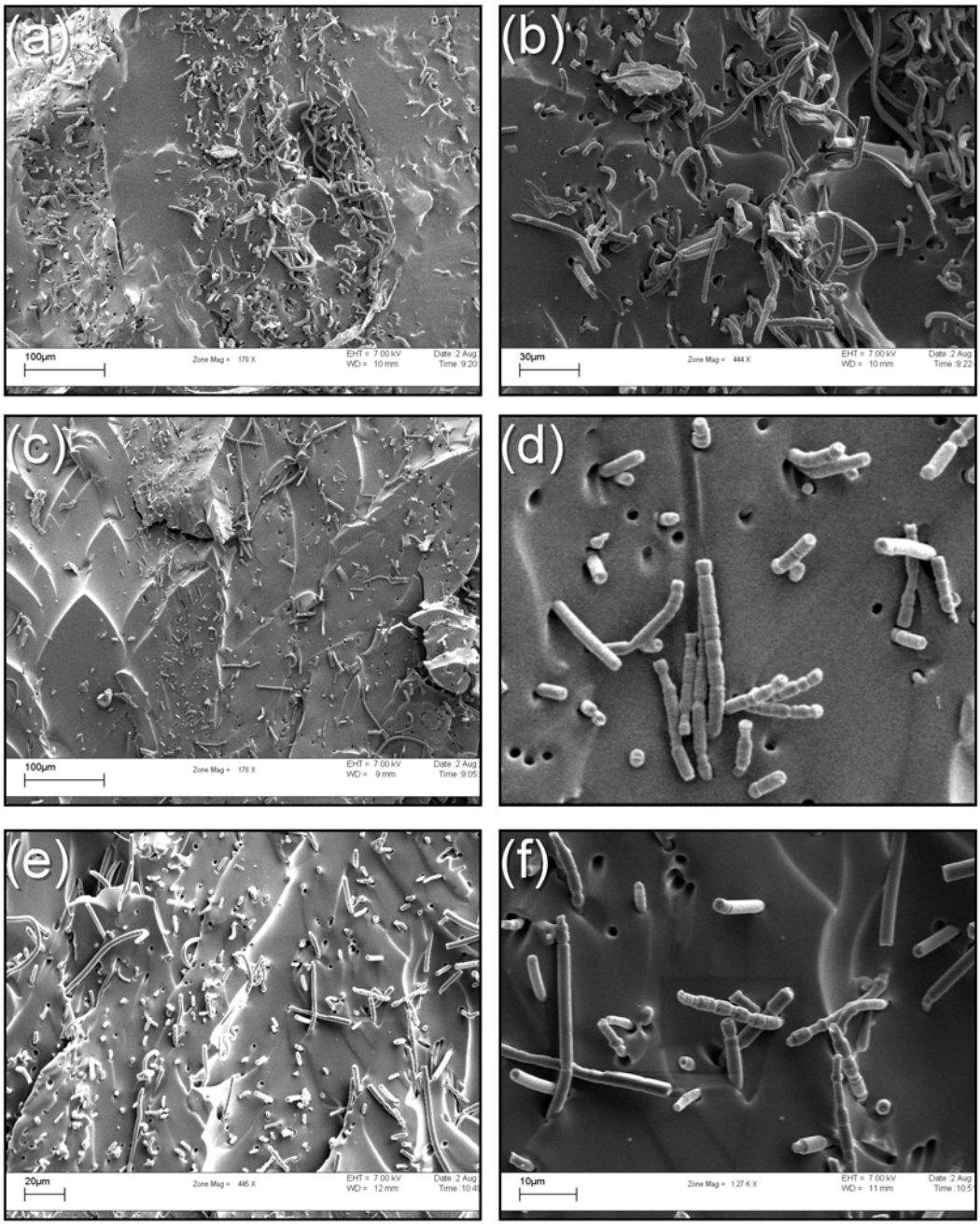

Figure 4.51 *SEM images of a 34wt% fractured composite. Figures (a) and (b) shows fractured surfaces of single layer composites, Figures (c) and (d) of double layer composites and Figures (e) and (f) of multi-layer composites*

4.4.5. Porous crosslinked PDMS

A preliminary study on the suitability of the composite material to be used as a technique for the synthesis of porous crosslinked PDMS compounds was carried out. This study was done to determine if the nanofibers could be "dissolved out" of the crosslinked PDMS matrix. The composite samples were placed in THF and allowed to swell. The PMMA-g-PDMS hybrid

nanofibers used to reinforce the silicone will readily dissolve in THF. This leads to the fact that when the composite is allowed to swell and reach equilibrium, the nanofibers will dissolve and leach out. Figure 4.52 shows the cryo-fracture surfaces of the composites after deswelling. In this case the samples were removed from the THF and the gel was placed in liquid N_2. This was then fractured and the gel allowed to deswell. Once deswelled the result will be a porous silicone matrix with nanometer pore sizes. Samples were left to swell and reach equilibrium for 48hours, where after they were placed in liquid nitrogen and cryo-fractured. The resultant fractured cross sections were then analyzed using Scanning Electron Microscopy. The results are shown in Figure 4.52 below. It is clear that the leaching technique worked well and that a porous silicone matrix was the result. Figure 4.52 shows several different regions of the cryofractured sample. In this case a multilayered reinforced 34wt % nanofiber system was used. Figure 4.52 (a-d) shows that pore sizes match those of individual fibers, and are well distributed throughout the matrix.

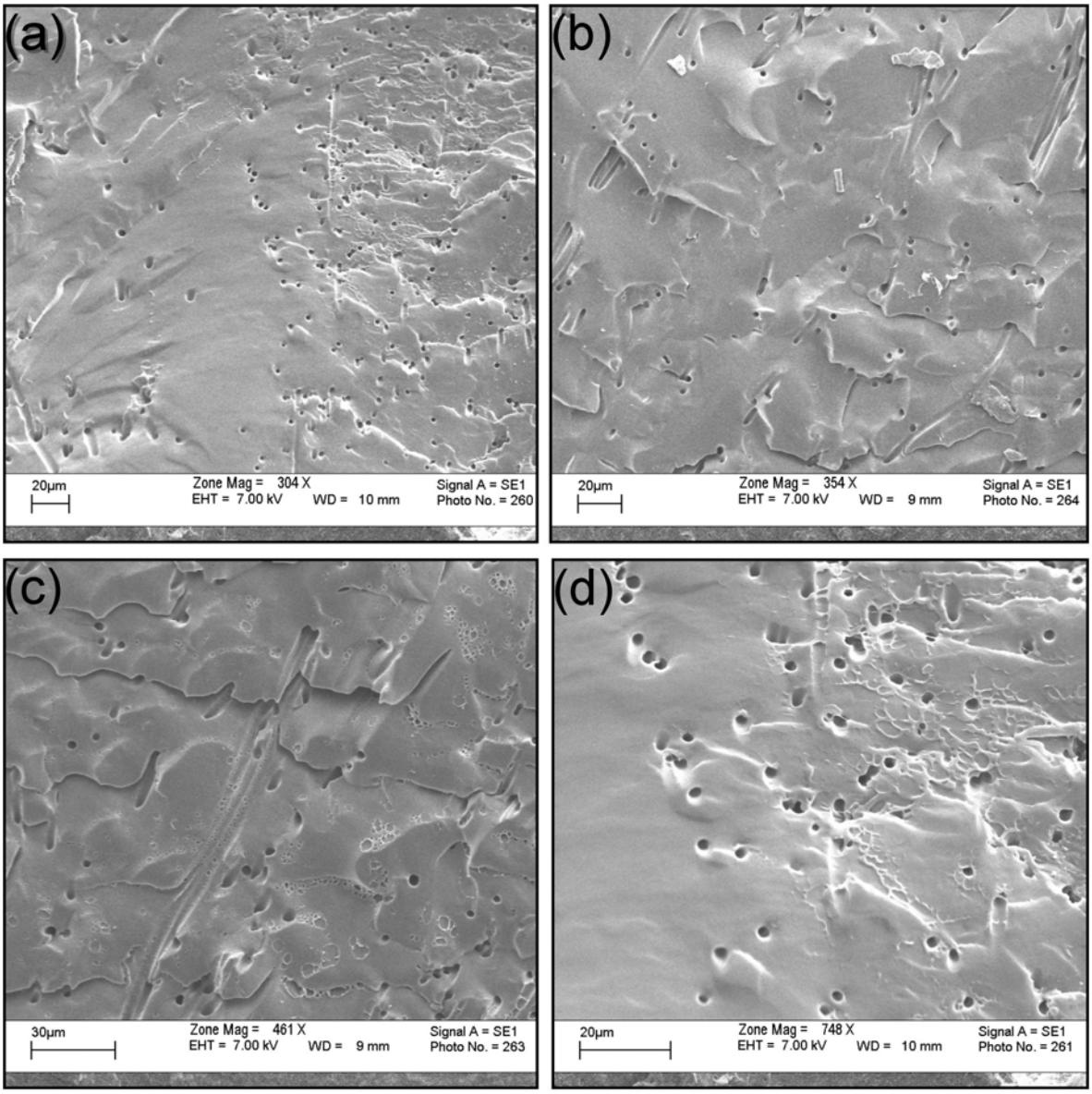

Figure 4.52 *SEM images illustrating the porous silicone matrix after the extraction of the PMMA-g-PDMS nanofibers.*

4.5. References

1. Buchko, C. J.; Shen, Y.; Martin, D. C.; Chen, L. C. *Polymer* **1999,** 40 7397–7407.
2. Zhong, X. H.; Kim, K. S.; Fang, D. F.; Ran, S. F.; Hsiao, B. S.; Chu, B. *Polymer* **2002,** 43, 4403-4412.
3. Schunk, T. C.; Long, T. E. *J. Chrom.* **1995,** 692, 221-232.
4. Ikada, Y., *Structure and Properties of Polymers (Advances in Polymer Science, Vol. 29)*. Springer: New York, 1978.
5. Schunk, T. C. *J. Chromatogr.* **1994,** 661, 215.
6. Bayley, G. Synthesis and characterization of organic-inorganic hybrid block copolymers of PDMS and polystyrene. University of Stellenbosch, Stellenbosch, 2007.
7. Smith, S. D.; DeSimone, J. M.; Huang, J. H.; York, G.; Dwight, l. D. W.; Wilkes, G. L.; McGrath, J. E. *Macromolecules* **1992,** 25, 2575-2581.
8. Ramahrisha, S.; Fujihara, K.; Teo, K. E.; Lim, T. C.; Ma, Z., *An introduction to Electrospinning and Nanofibers*. World Scientific Publishing Co. Pte. Ltd.: Singapore, 2005.
9. Megelski, S.; Stephens, J. S.; Chase, D. B.; Rabolt J.F. *Macromolecules* **2002,** 35, 8456-8466.
10. Mit-upputhum, C.; Nithitanakul, M.; Supapol, P. *Macromol. Chem. Physic* **2004,** 205, 2327-2338.
11. Koombhongse, S.; Liu, W.; Reneker, D. H. *J. Polym. Sci. B : Polym. Phys.* **2001,** 39, 2598.
12. Tsai, P. P.; Chen, W.; Roth, J. R., Investigation of the Fiber, Bulk, and Surface Properties of Meltblown and Electrospun Polymeric Fabrics. In Textiles and Nonwovens Development Center (TANDEC): 2004.
13. Jean, Y. C.; Mallon, P. E.; Schrader, D. M., *Principles and Applications of Positron and Positronium Chemistry*. World Scientific Publishing Co. Pte. Ltd.: 2003.
14. Coleman, P. G., *Positron Beam and Their Applications*. World Scientific Publishing: Singapore, 2000.
15. Krause-Rehberg, R.; Leipner, H. S., *Positron Annihilation in Semiconductors*. Springer: Berlin, 1999.
16. Schultz, P. J.; Lynn, K. G. *Rev. Mod. Phys.* **1989,** 60, 701.
17. Bayley, G.; Mallon, P. E. *Polym. Eng. And Sci* Article in press 2007.

18. Hinder, S. J.; Lowe, C.; Maxted, J. T.; Watts, J. F. *Prog. Org. Coat.* **2005,** 54, 104–112.
19. HA, C. S.; Gardella, J. A. *J. Macromol. Sci.* **2005,** 45, 1-18.
20. Chen, X.; Gardella, J. A. *Macromolecules* **1993,** 26, 3778-3783.
21. Callies, M.; Que´re´, D. *Soft Matter* **2005**.
22. Mathilde Callies; Que´re´, D. *Soft Matter* **2005**.
23. Chang, J. W.; Gorur, R. S. *IEEE Trans. Diel. Electr. lnsul* **1994,** 6, 1039.
24. Kim, S. H.; Cherney, E. A.; Hackam, R. *IEEE Trans. Power Deliv* **1991,** 6, 1549.
25. Owen, M. J.; Gentle, M.; Orbeck, T.; Williams, D. E., *Polymer Surface Dynamics*. Plenum Press: New York, 1988.
26. Vlastos, A.; Gubanski, S. *IEEE Trans. Power Deliv.* **1991,** 6, 888.
27. Hillbong, H.; Gedde, U. W. *Polymer* **1997,** 39, (10), 1991-1998.
28. Toth, A.; Bertoti, I.; Blazso, M.; Banhegyi, G.; Bognar, A.; Szaplonczay, X. *Appl. Polym. Sci* **1994,** 52, 1293.
29. Hara, T. A.; Serra, M. S.; Rodrigues, A. L. *Braz Dent J* **2000,** 12, (2), 2001.
30. Pyun, J.; Matyjaszewski, K. *Chem. Mater.* **2001,** 13, 3436-3448.

Conclusion

This chapter gives a brief discussion on the conclusions that can be made from the study. Also discussed are recommendations for future work.

5.1. Conclusions

PMMA-g-PDMS graft copolymers, with varying PDMS chain lengths and varying compositions were successfully synthesized using the grafting through technique. All the polymers prepared showed good distribution in molar mass with polydispersity values varying between 1.8 and 3. ^{1}H-NMR analysis confirmed that a relatively high amount of PDMS was incorporated into the graft copolymer with percentage macromonomer incorporations as high as 64%.

Gradient elution HPLC was used to track the extraction of unreacted PDMS macromonomer as well as to monitor the chemical composition of the prepared hybrid polymers. This separation technique can also be applied in future work to study the morphological changes in the graft copolymers as a function of chemical composition. Preliminary studies were done on SEC coupled to TEM via LC Transform to establish the morphology of the prepared materials. This yielded some very interesting results concerning the morphology and especially the phenomenon of phase segregation across the molar mass distribution.

The organic-inorganic hybrid polymers were successfully "spun" into nanofibers using the electrospinning technique. This is one of the first documented cases of PDMS containing hybrid materials being made into nanofibers and the first example for PMMA-graft-PDMS polymers. SEM analysis showed that the composition of the polymer has a definite affect on the morphology of the nanofibers after electrospinning. The fiber morphologies varied from highly beaded to completely smooth uniform fibers. The electrospinning process has many variables that affect the morphology of the resultant nanofibers. In this study, the affects of the tip-to-collector distance, and the spinning solution concentration on the fiber morphology were investigated. Both these parameters yielded interesting results regarding fiber diameter and appearance. It was established that increasing the tip-to-collector spinning distance led to a general decrease in the fiber diameter and that increasing the solution concentration resulted in the fiber appearance changing from branched to uniform as well as the formation of ribbon like

structures. By knowing which parameter yields a certain structure or morphology, electrospinning can be used to tailor the nanomaterials for a specific application.

Confocal Raman spectroscopy enabled the characterization of individual hybrid nanofibers and may prove a very valuable technique in the future for the characterization of nanofiber reinforced composites and the way the fibers behave under stress.

For the first time non-woven hybrid nanofibers were also analyzed using the Slow Positron Beam technique. Results showed that nanofiber materials have very interesting surface properties. However, due to the nature of the nanofiber surface, analysis by means of Slow Positron Beam led to unique problems. It is evident that methods will have to be developed to ensure that the surface character of the samples remains uniform and consistent during the pumping down of the chamber to vacuum. Comparing the electrospun samples to normal spin coated bulk polymer films still, however, yielded interesting results showing that the higher S parameter in electrospun samples at the surface are due to the presence and preferential surface segregation of the PDMS component.

The electrospun nanofibers yielded superhydrophobic surfaces with static contact angles (SCA) in excess of 160^{o}. This phenomenon can be attributed to two main factors; the presence of PDMS, which is naturally hydrophobic, as well as the essentially infinitely rough surface morphology of the nanofibers. Hydrophobicity was shown to increase with an increase in the amount of PDMS present in the copolymer as well as with increasing TCD (and hence smaller fiber diameter). Nanofibers were also subjected to corona discharge, which resulted in a total loss of hydrophobicity after as little as 1min of exposure. This change to an essentially superhydrophillic surface was seen to be temporary and the phenomenon of hydrophobicity recovery occurred. The tracking of this recovery is also one of the first documented cases for PDMS containing hybrid materials showing this type of behavior. It was established that there exists a critical exposure time where after loss in hydrophobicity is permanent.

The last section of this studied looked at the use of PMMA-g-PDMS nanofiber systems as reinforcing fillers in a silicone matrix. A method was developed to produce nanofiber composites. SEM analysis of both the cut cross sections of the composites as well as on the cryofracture surface of the composites showed a remarkably good fiber distribution in the crosslinked PDMS matrix. Mechanical testing showed a dramatic reinforcing effect of the nanofibers especially for the higher content PDMS nanofiber. Examination of the fracture surfaces of the composites after mechanical testing showed that in some cases the fibers were deformed (elongated) showing that they carried a significant load during the mechanical testing.

Recommendations for future work.

The preliminary study done by coupling SEC to TEM for morphological analysis of the hybrid materials as a function of the molar mass has shown some interesting results. Further work should be done where gradient elution chromatography is coupled in the same way to TEM. This would allow for the determination of the phase morphology as a function of the chemical composition of the graft copolymers.

This study has demonstrated that the electrospinning technique and preferential surface segregation of the PDMS component is a relatively simple processing technique which maximized the surface segregation of PDMS in the hybrid materials. This should be studied further for potential applications.

The reinforcing potential of organic-inorganic hybrid polymer nanofibers should be investigated further. Alternative composite preparation methods should be investigated for the distribution of the nanofibers in the matrix. Possible alternates would be the direct spinning of the nanofibers onto the uncrosslinked PMDS followed by curing. The possibility of producing aligned nanofiber and using them for reinforcing should also be investigated.

The preliminary study on the production of porous cross linked PDMS compounds has demonstrated that using nanofibers as templating materials is a viable method for the production of such materials. This should be further investigated. This methodology has the potential for controlling the porous structure by controlling the fiber morphology during electrospinning. If this is combined with alignment of the nanofibers this technique has the potential for producing cross linked porous PDMS compounds with continuous channels of controlled dimensions.

Appendix

Figure A.1 *Water droplet illustrating the superhydrophobicity of a PMMA-g-PDMS surface*

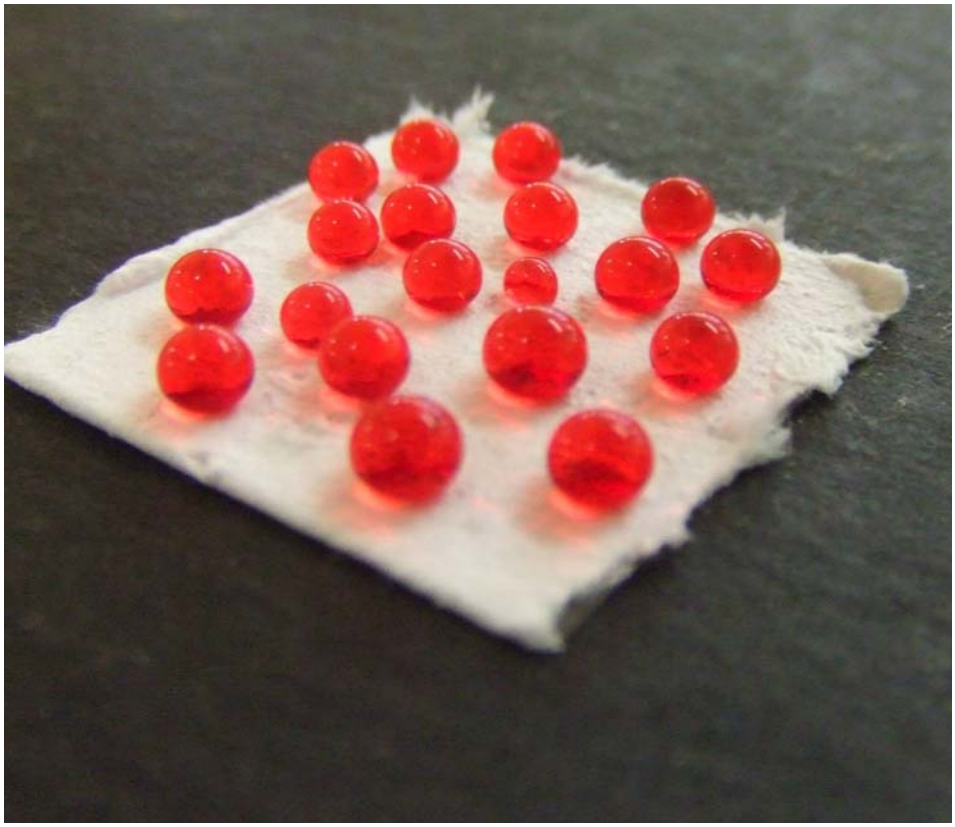

Figure A.2 Multiple w*ater droplets on a superhydrophobic surface.*

Figure A.3 Multiple w*ater droplets illustrating the superhydrophobicity of a PMMA-g-PDMS surface.*

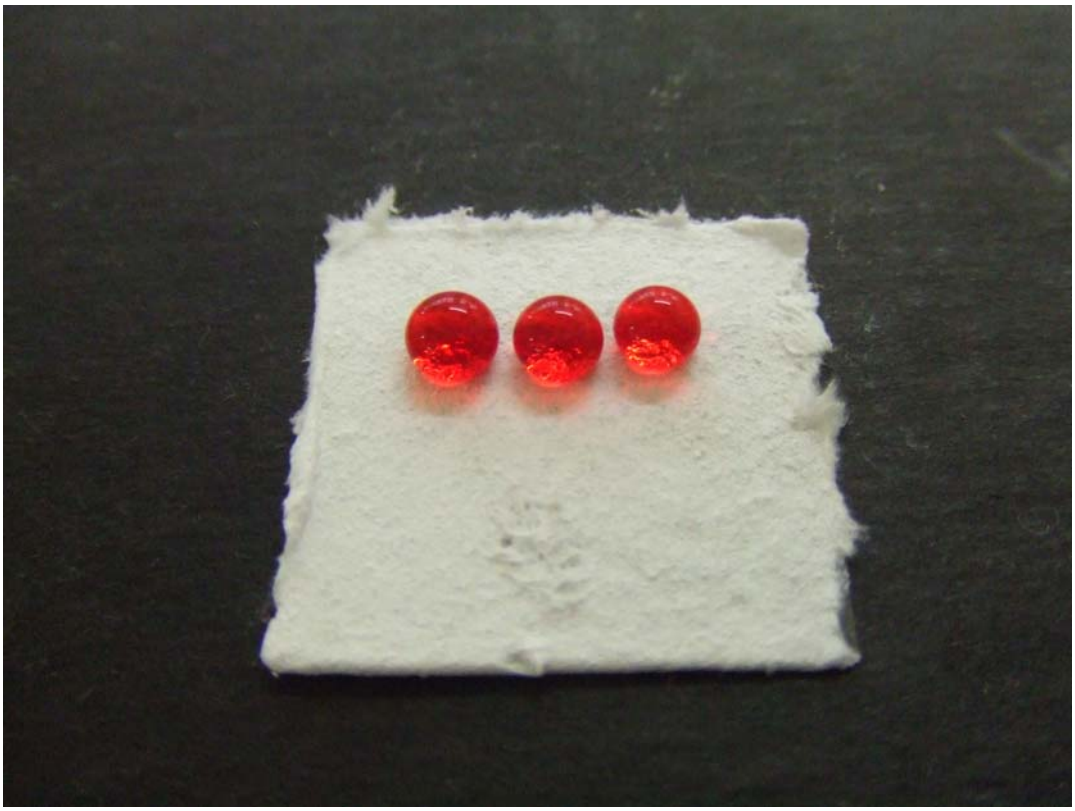

Figure A.4 *Water droplet illustrating the superhydrophobicity of a PMMA-g-PDMS surface*

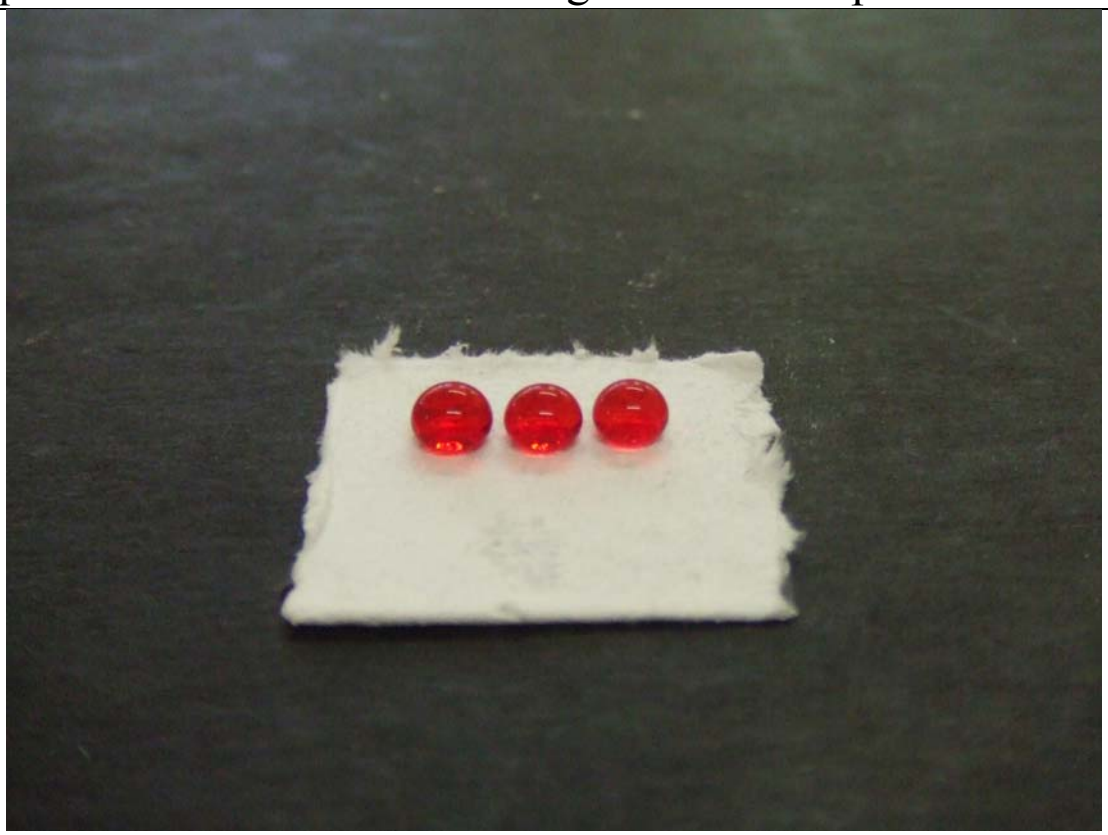

Figure A.5 *Water droplet illustrating the superhydrophobicity of a PMMA-g-PDMS surface*

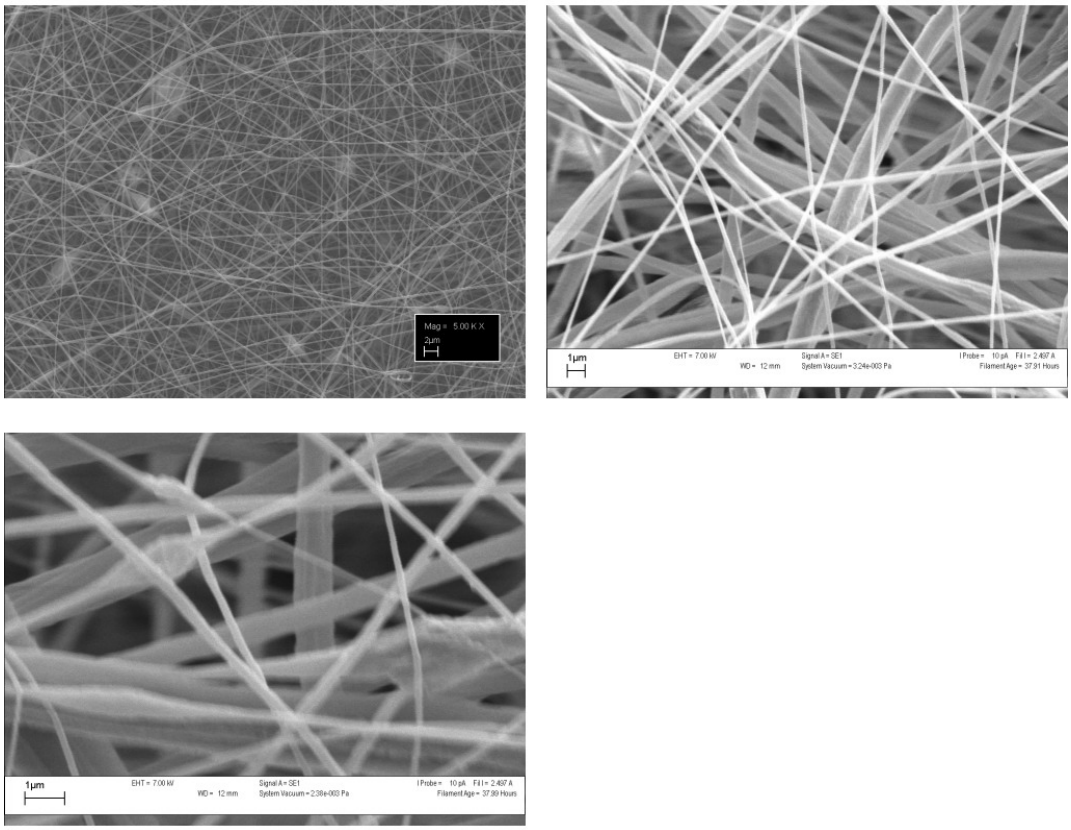

Figure B.1 *SEM images of electrospun PMMA nanofibers*

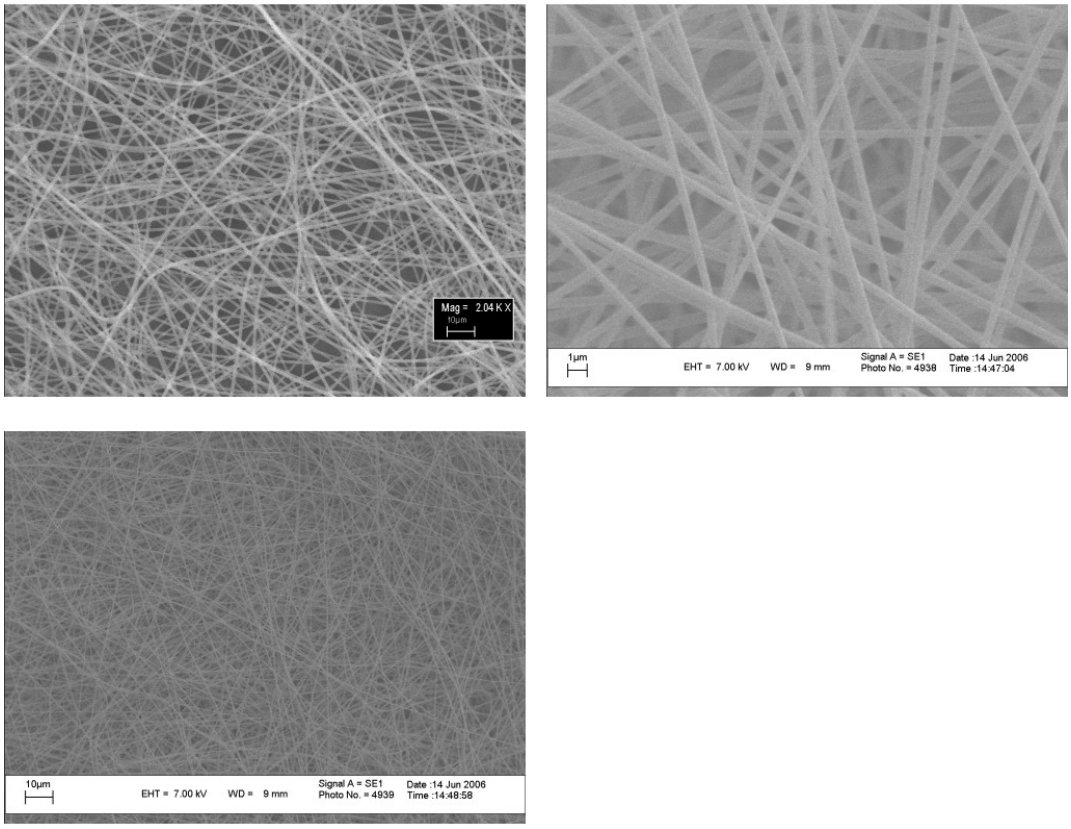

Figure B.2 *SEM Images of electrospun PMMA nanofibers after exposed to 30min of corona discharge*

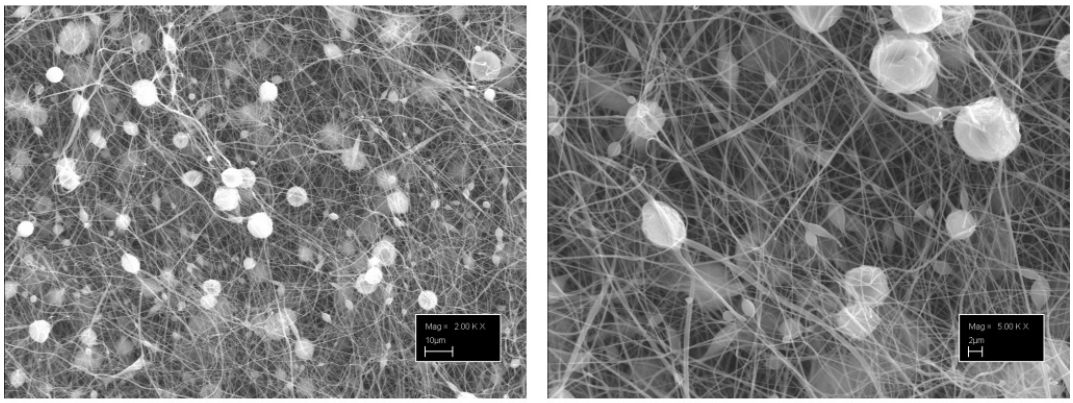

Figure B.3 *SEM images of electrospun 5wt% PDMS nanofibers*

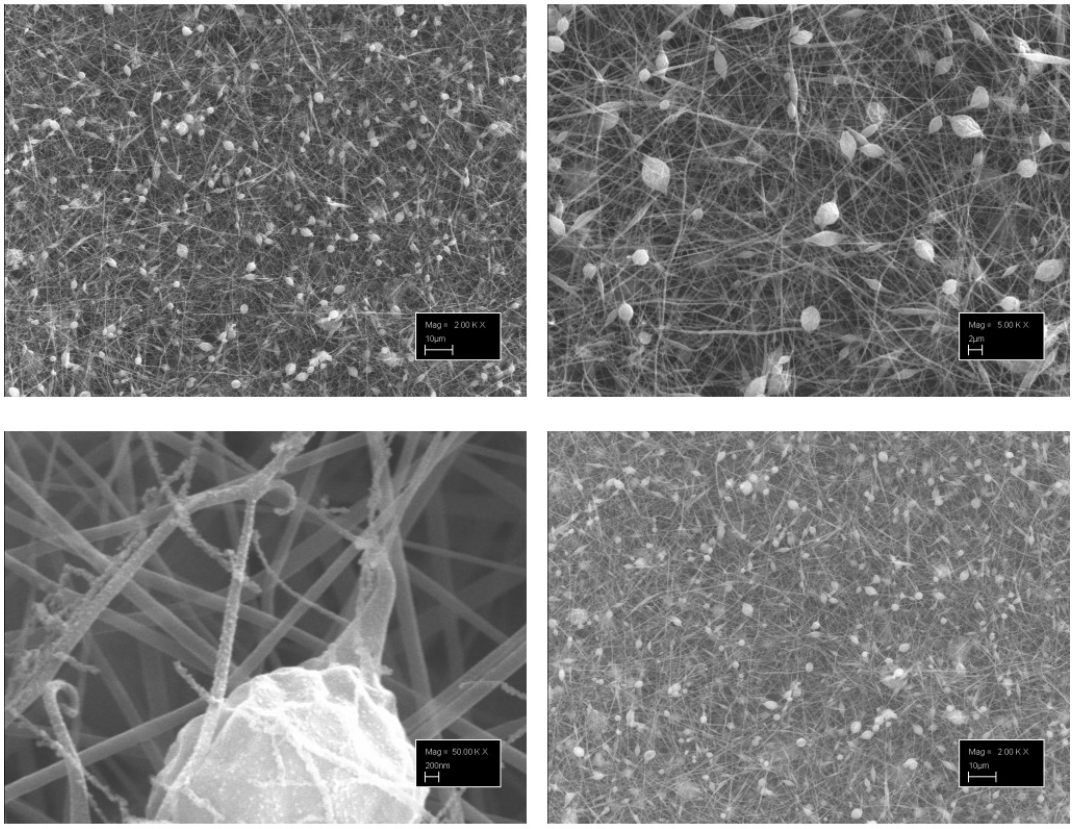

Figure B.4 *SEM Images of electrospun 5wt% PDMS nanofibers after exposure to 30min of corona discharge.*

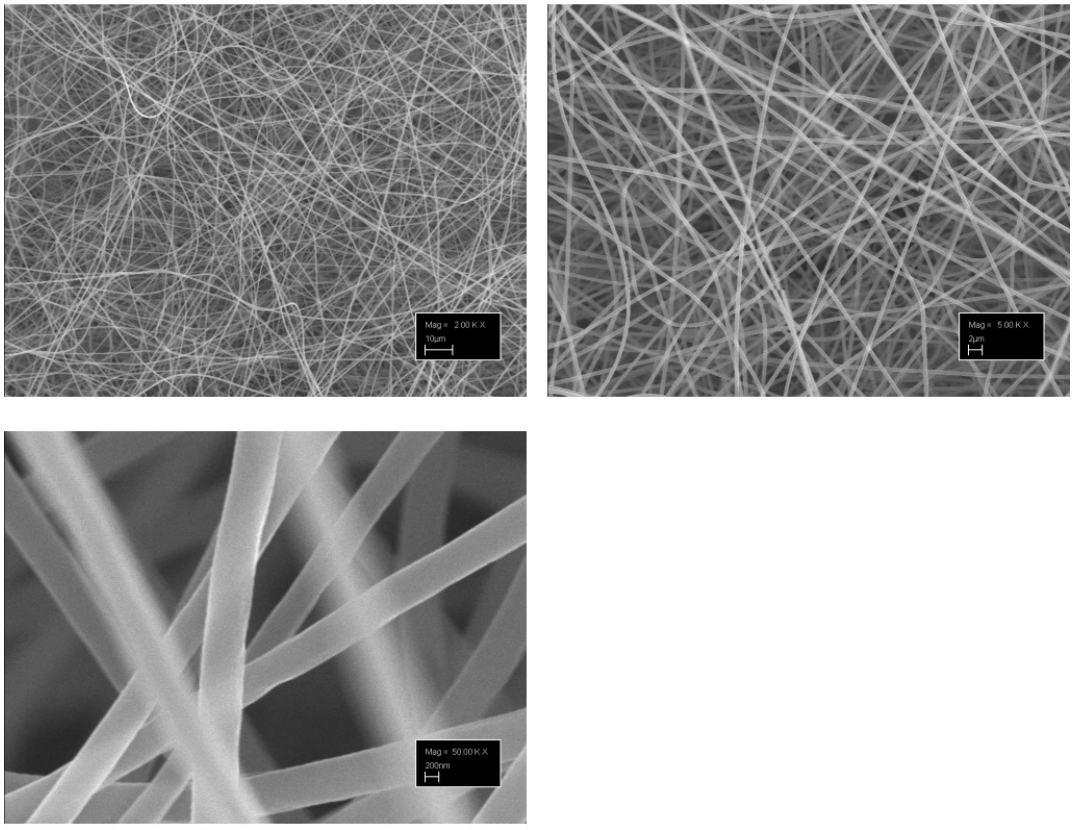

Figure B.5 SEM *images of electrospun 8.6wt% PDMS nanofibers*

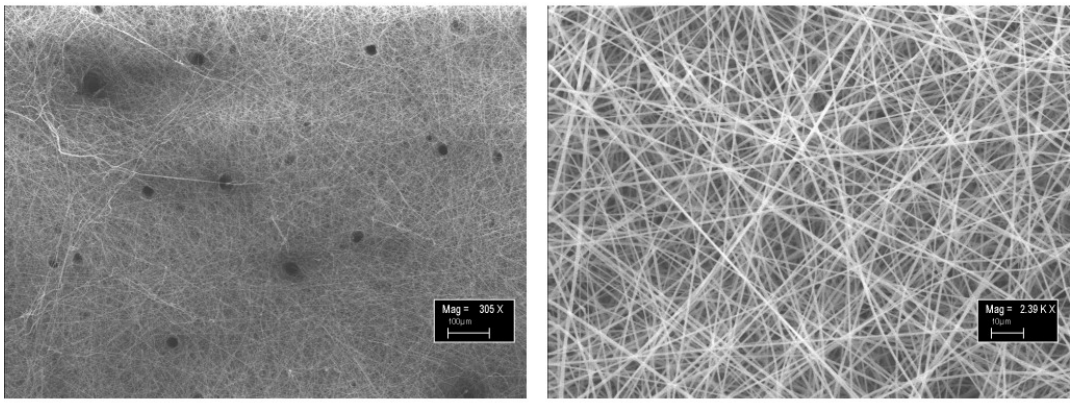

Figure B.6 *SEM Images of electrospun 8.6wt% PDMS nanofibers after exposure to 30min of corona discharge.*

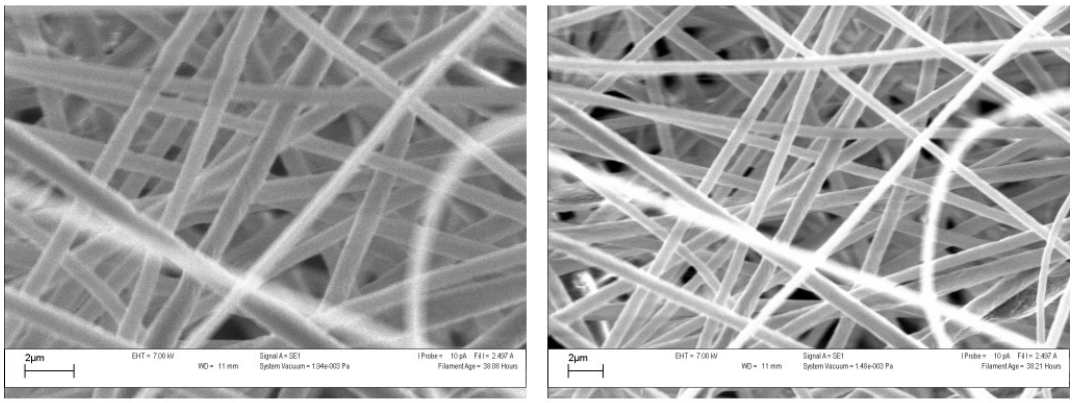

Figure B.7 SEM *images of electrospun 10wt% PDMS nanofibers*

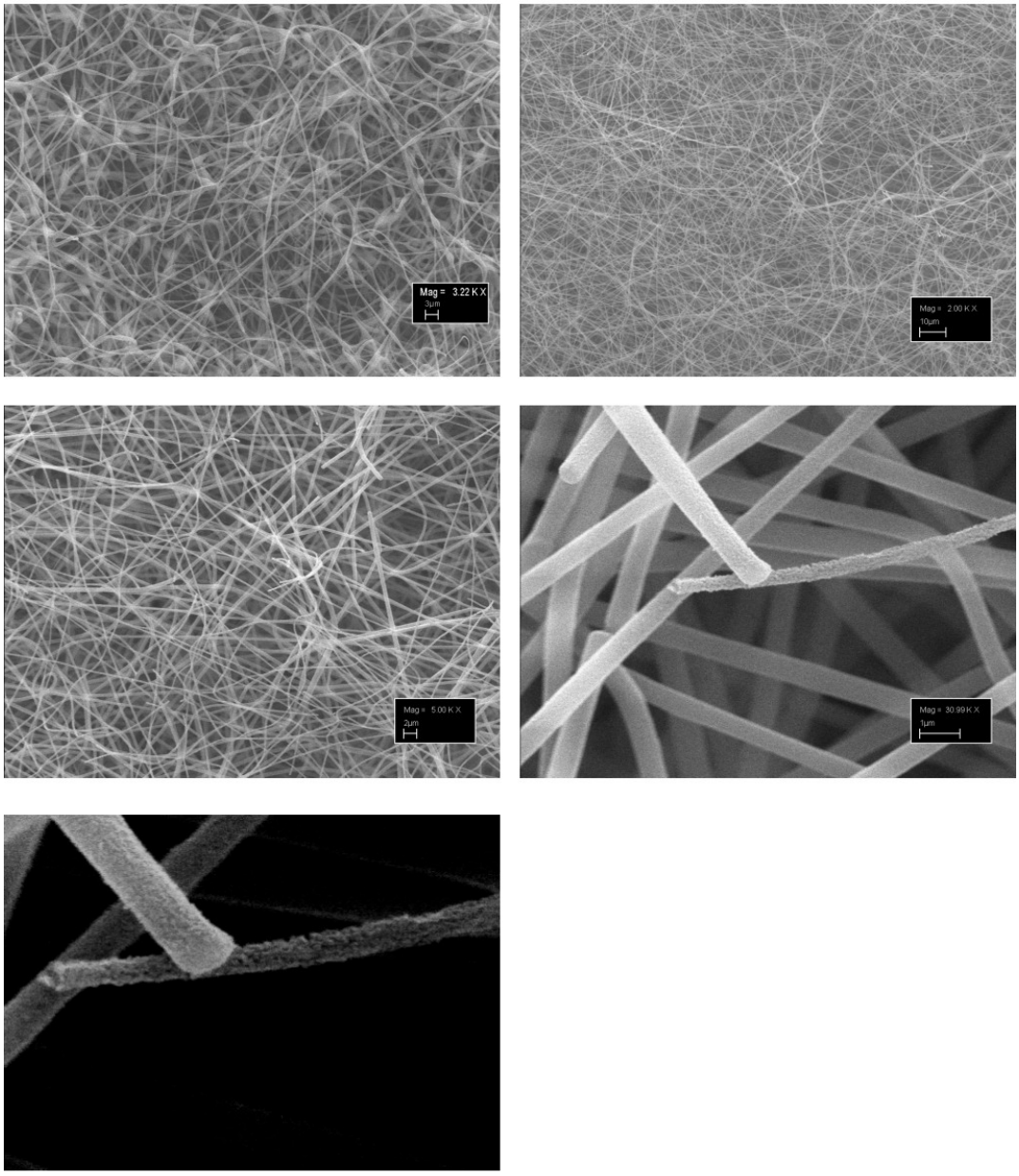

Figure B.8 *SEM Images of electrospun 10wt% PDMS nanofibers after exposure to 30min of corona discharge.*

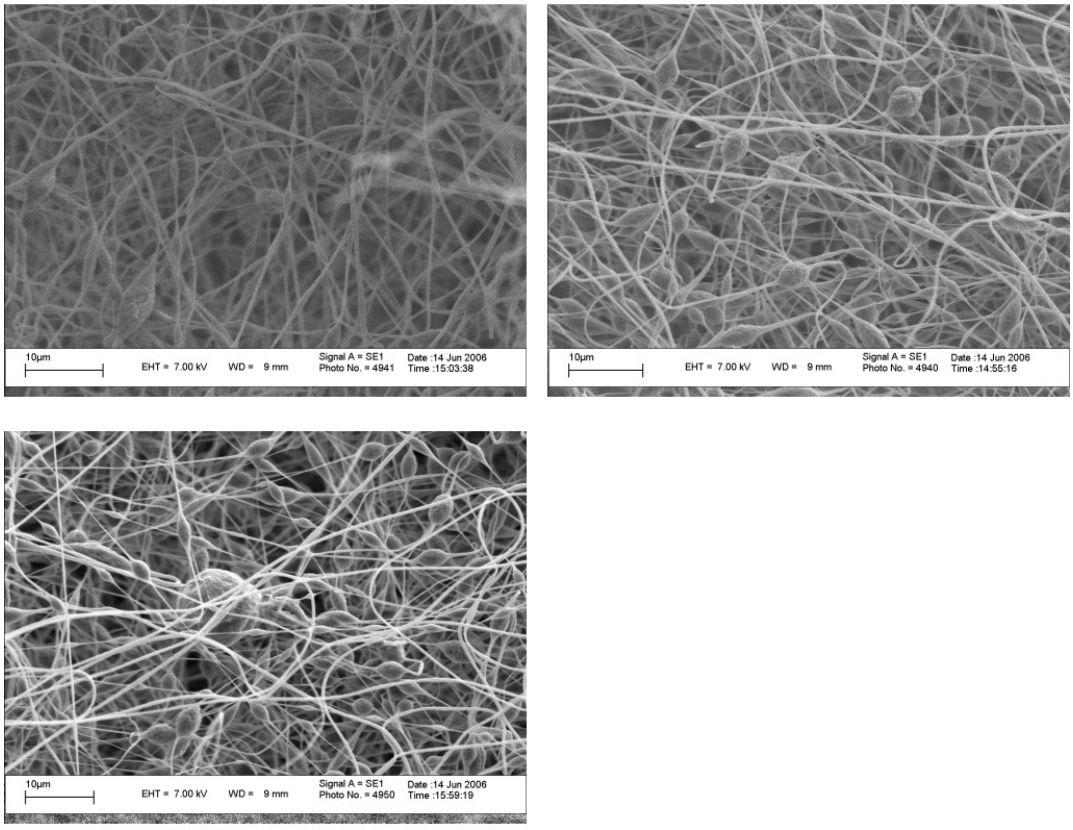

Figure B.9 SEM *images of electrospun 15wt% PDMS nanofibers*

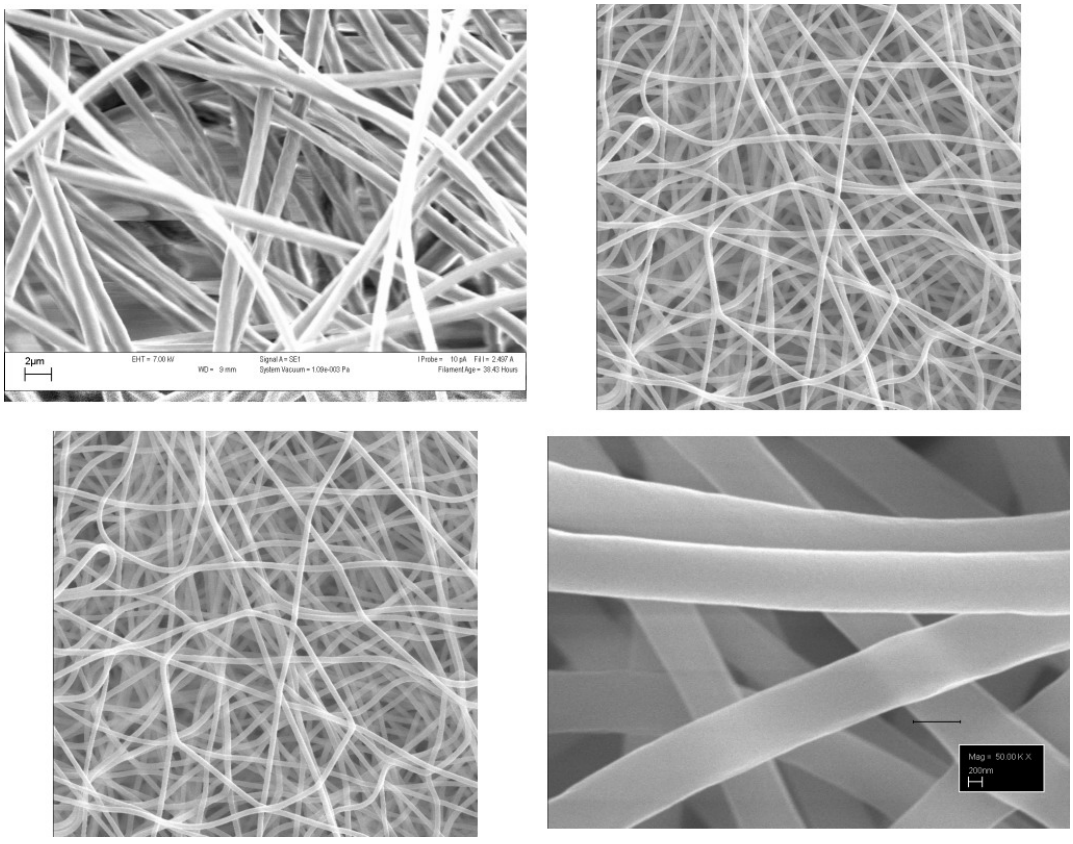

Figure B.10 SEM *images of electrospun 23wt% PDMS nanofibers*

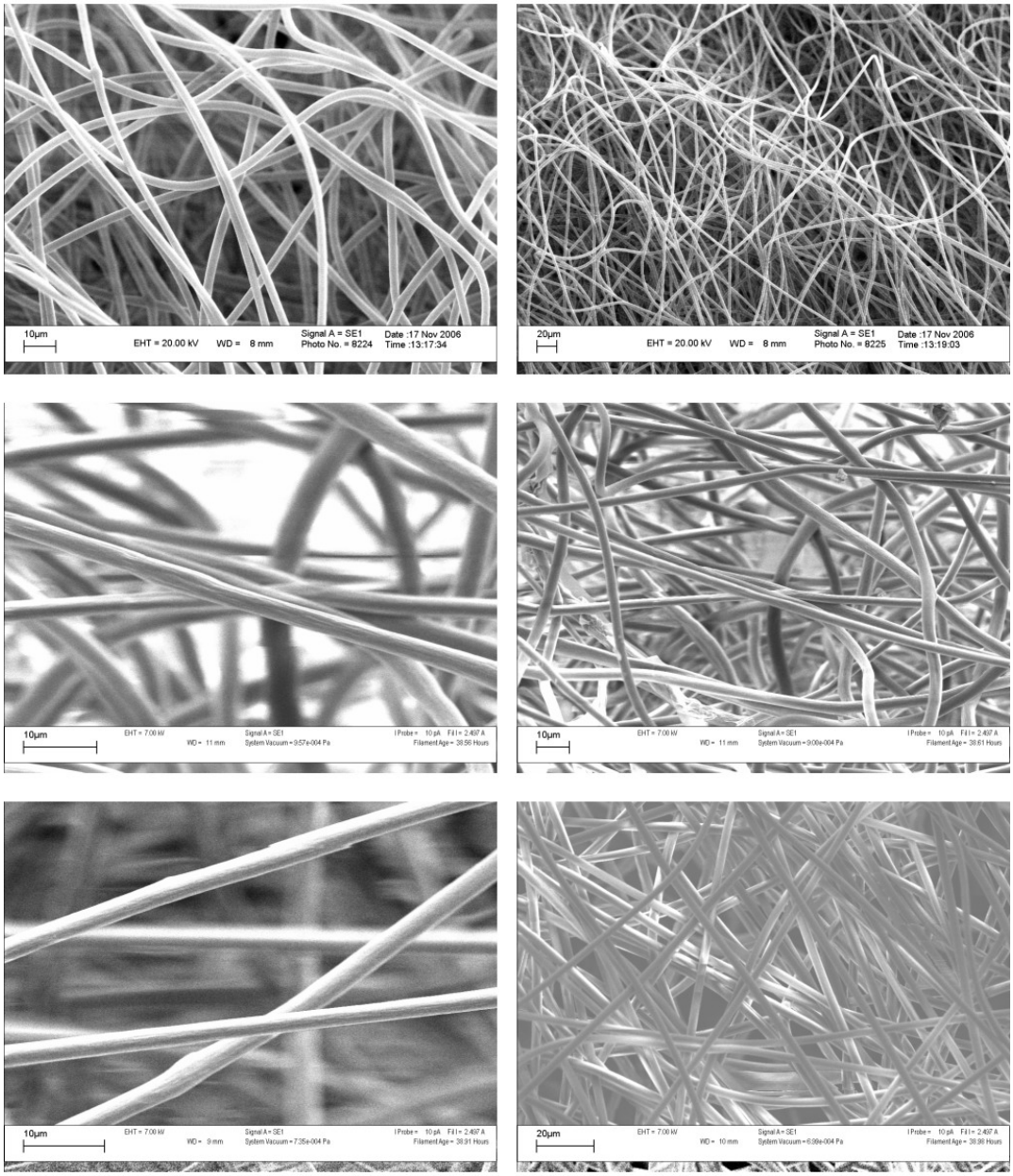

Figure B.11 SEM *images of electrospun 34wt% PDMS nanofibers*

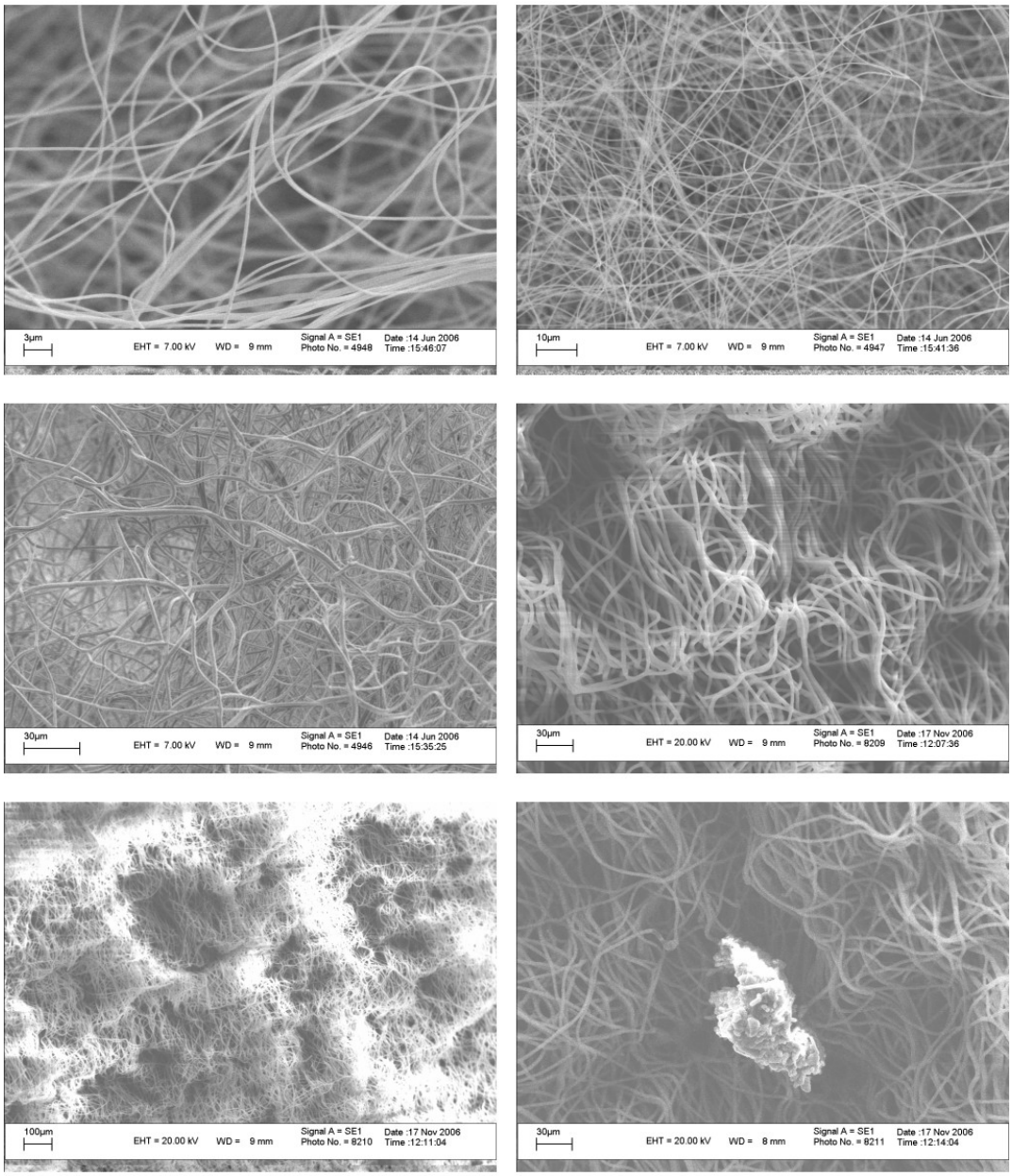

Figure B.12 *SEM Images of electrospun 34wt% PDMS nanofibers after exposure to 30min of corona discharge.*

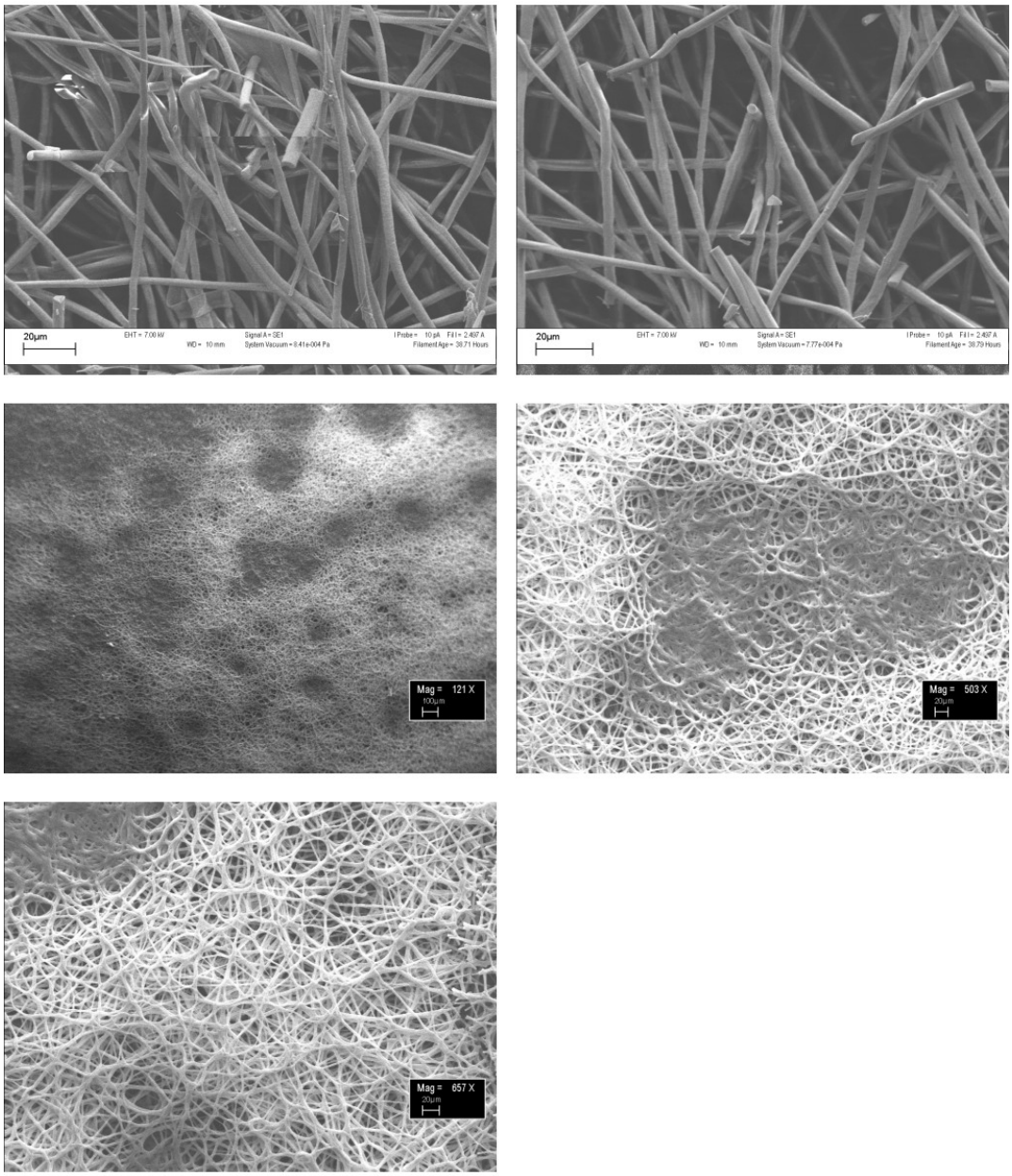

Figure B.13 *SEM Images of electrospun 34wt% PDMS nanofibers after exposure to 30min of corona discharge.*

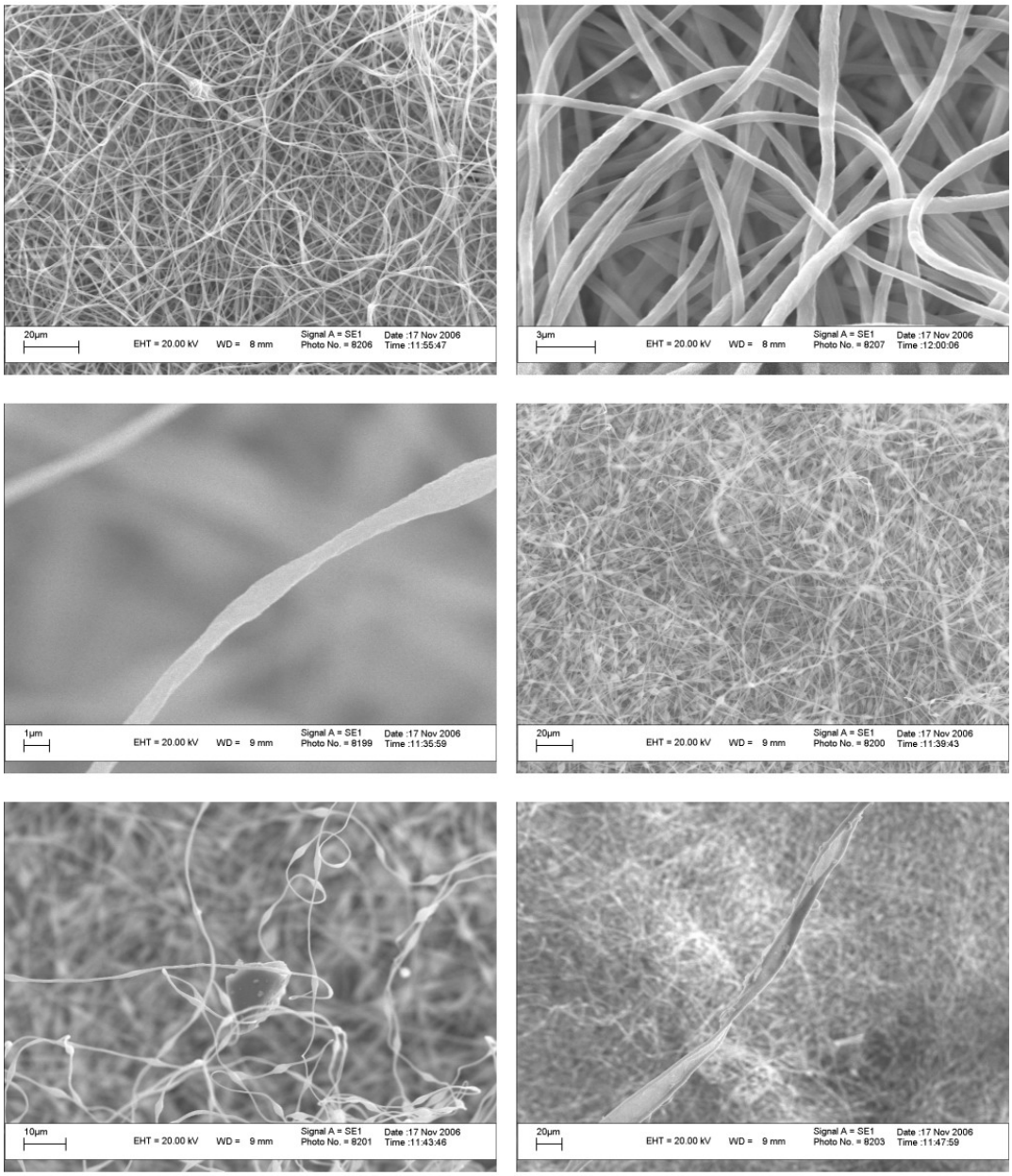

Figure B.14 SEM *images of electrospun 50wt% PDMS nanofibers*

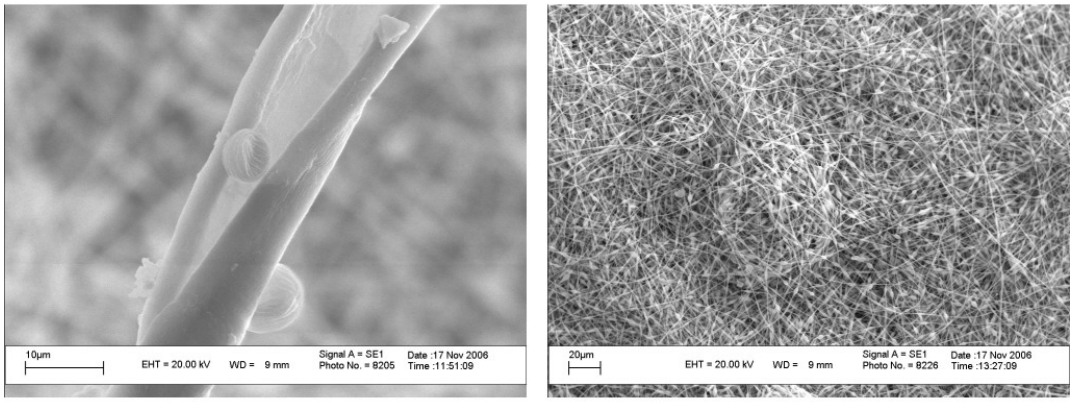

Figure B.15 SEM *images of electrospun 50wt% PDMS nanofibers*

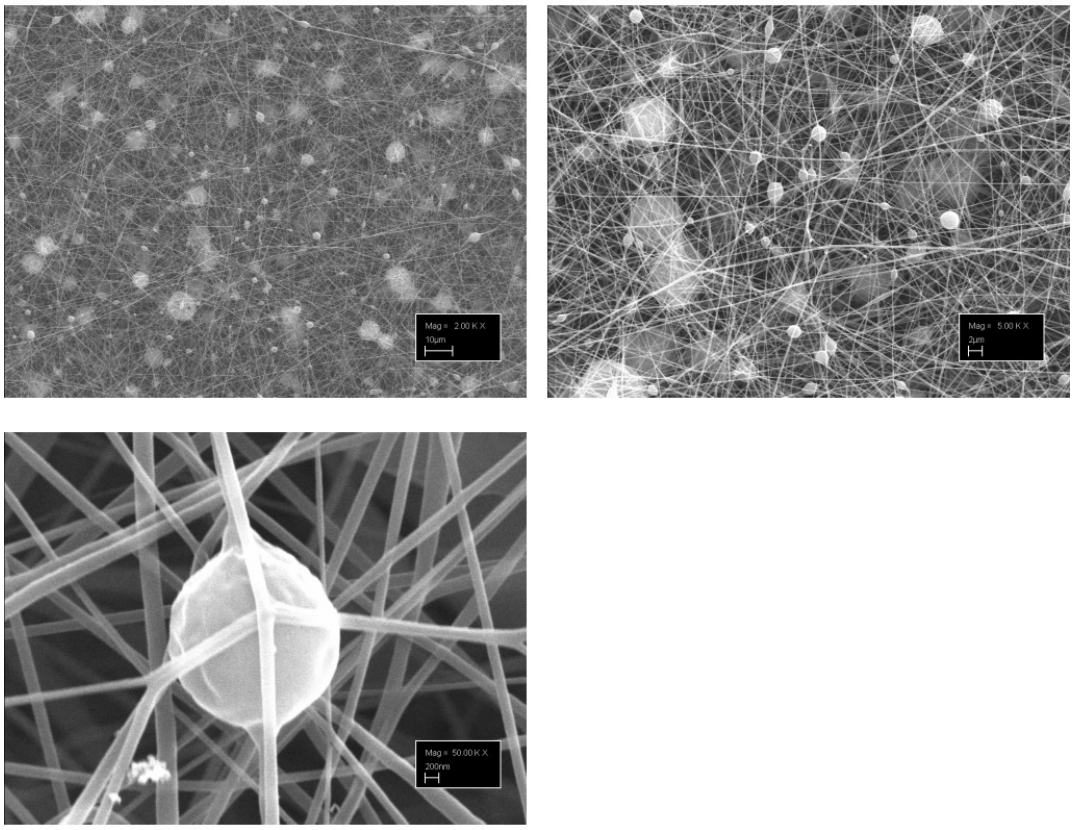

Figure B.16 SEM *images of electrospun 5wt% (medium) PDMS nanofibers*

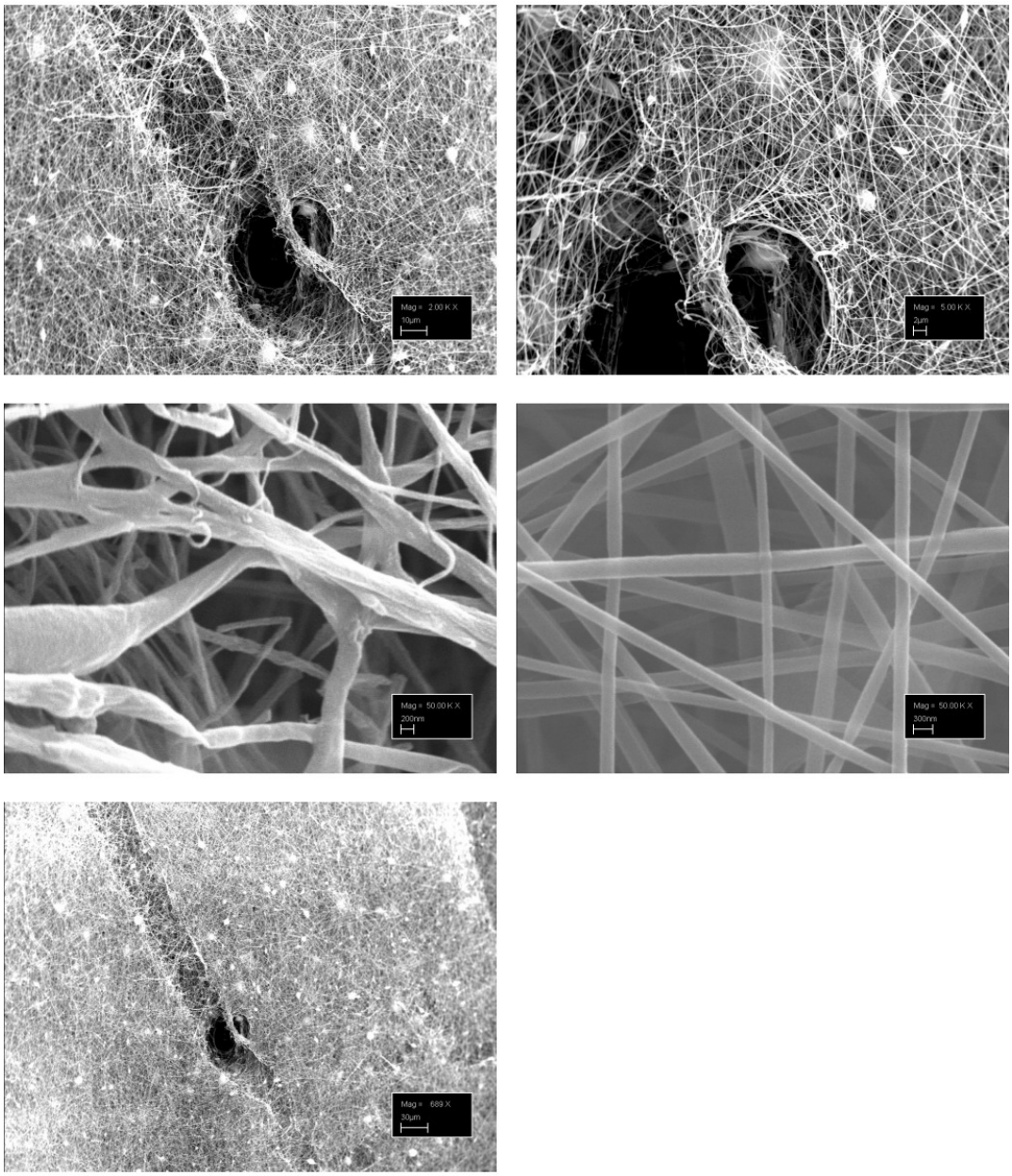

Figure B.17 *SEM Images of electrospun 5wt% (medium) PDMS nanofibers after exposure to 30min of corona discharge.*

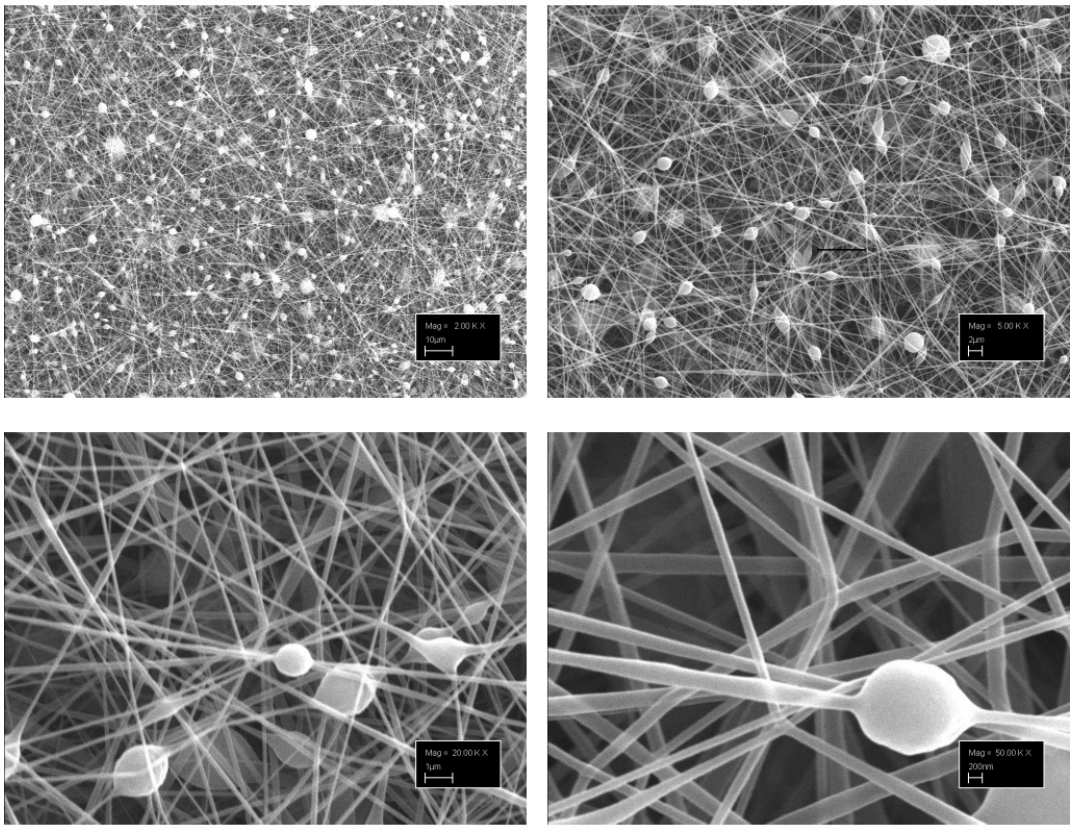

Figure B.18 SEM *images of electrospun 10wt% (medium) PDMS nanofibers*

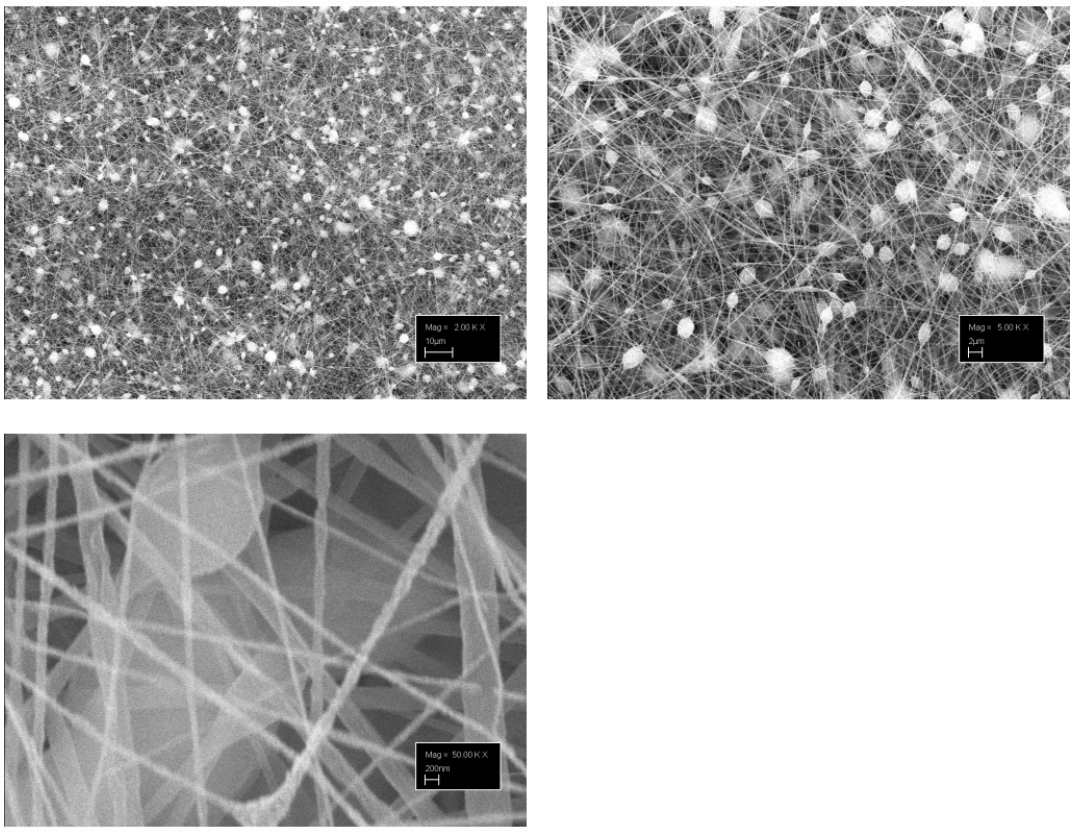

Figure B.19 *SEM Images of electrospun 10wt% (medium) PDMS nanofibers after exposure to 30min of corona discharge.*

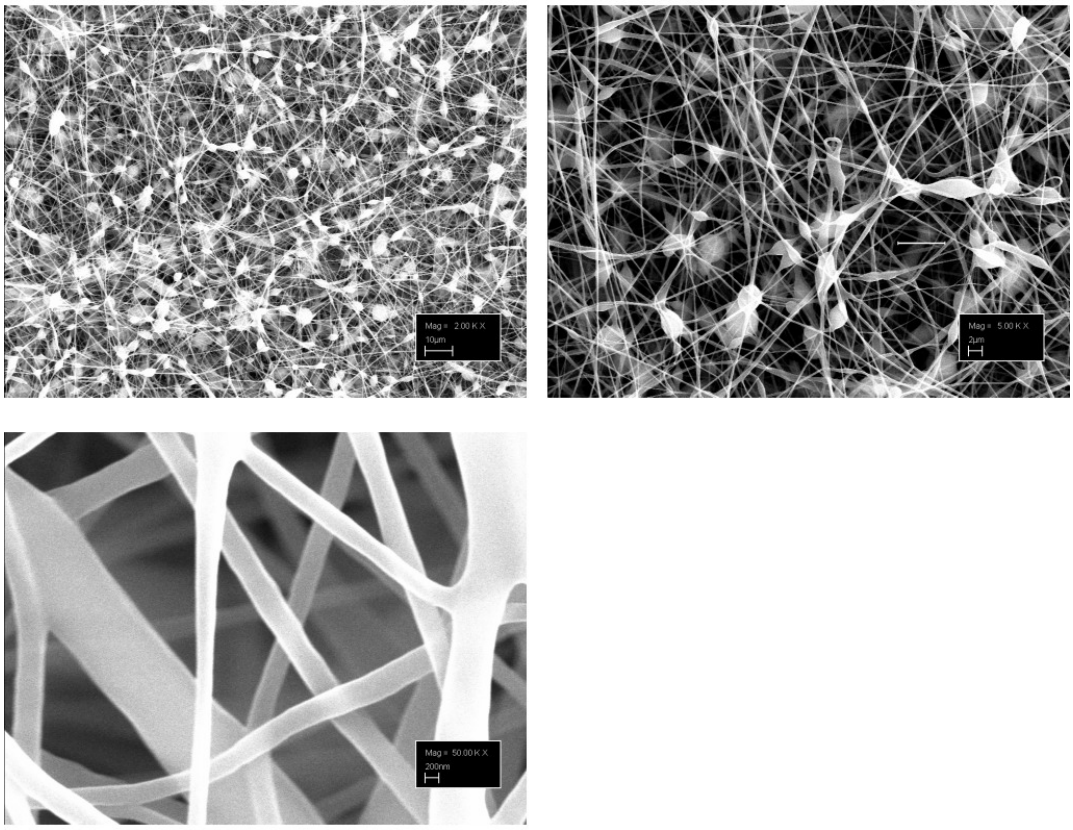

Figure B.20 SEM *images of electrospun 23wt% (medium) PDMS nanofibers*

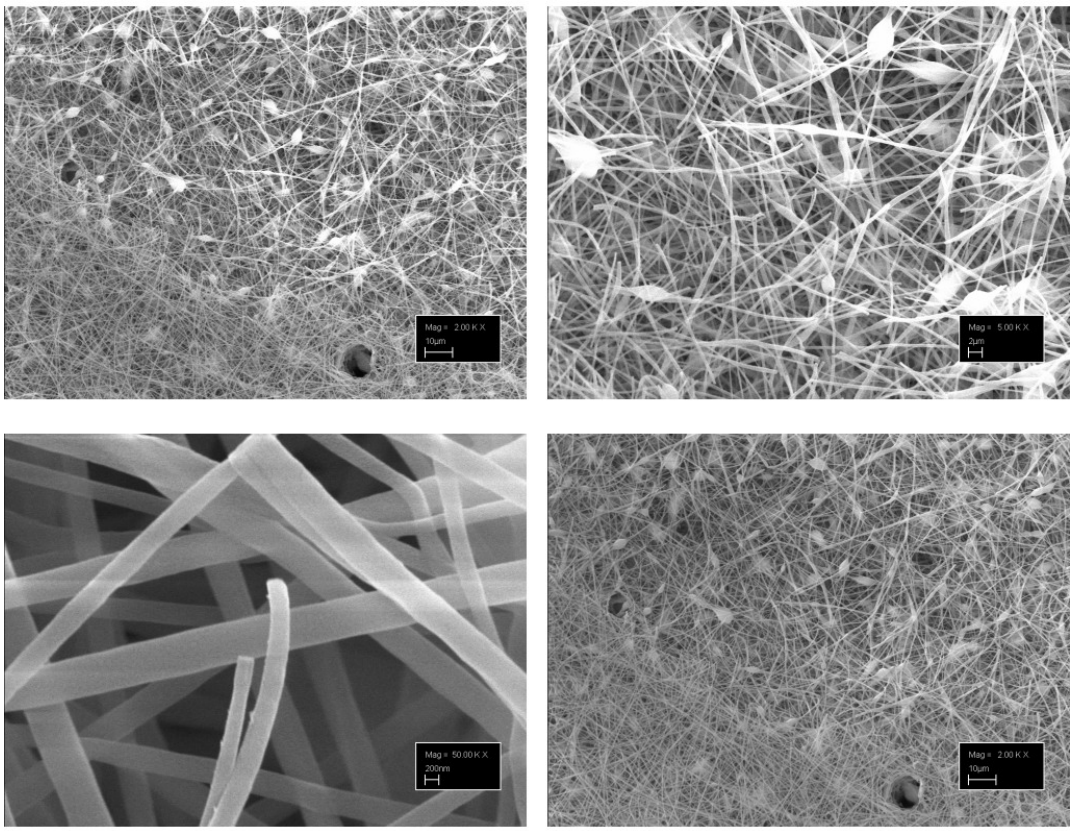

Figure B.21 *SEM Images of electrospun 23wt% (medium) PDMS nanofibers after exposure to 30min of corona discharge.*

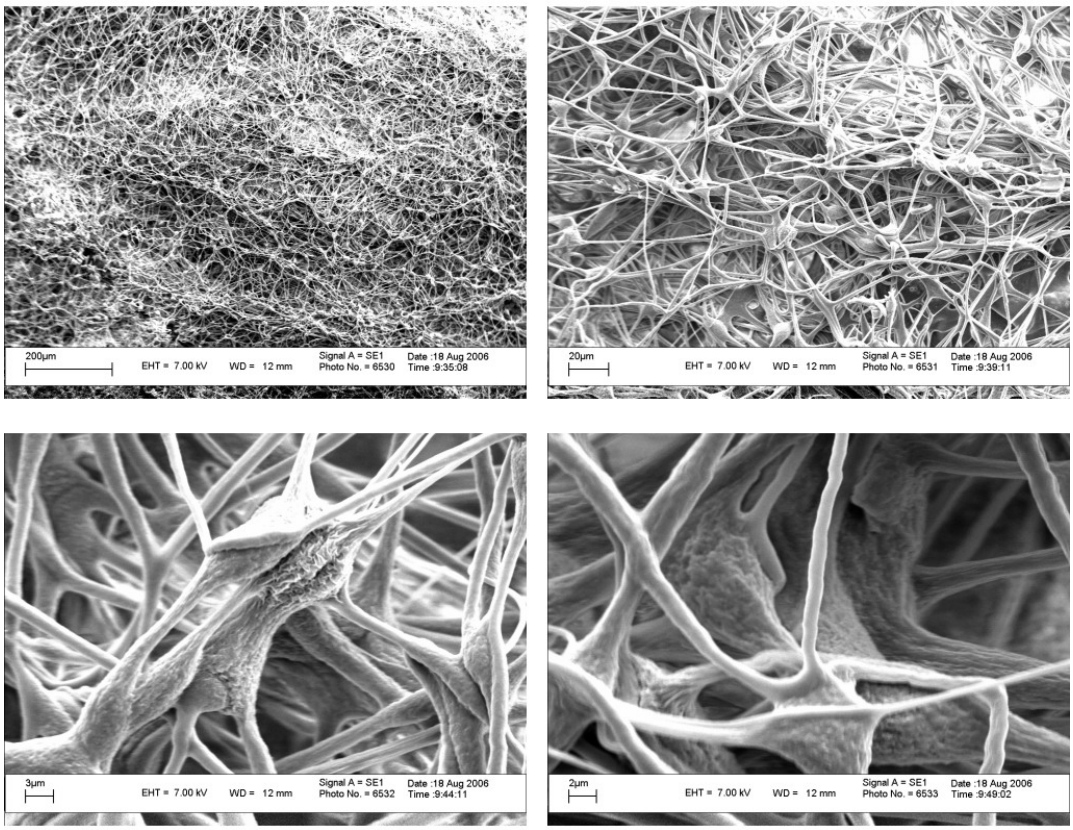

Figure C.1 *SEM images illustrating the surface morphology of electrospun 34wt% (short) PDMS nanofibers with an initial solution concentration of 5% (w/w)*

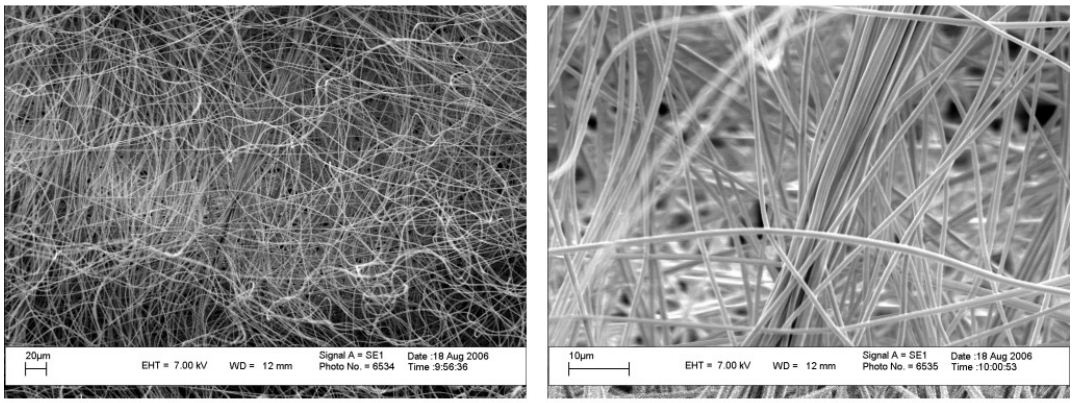

Figure C.2 *SEM images illustrating the surface morphology of electrospun 34wt% (short) PDMS nanofibers with an initial solution concentration of 10% (w/w)*

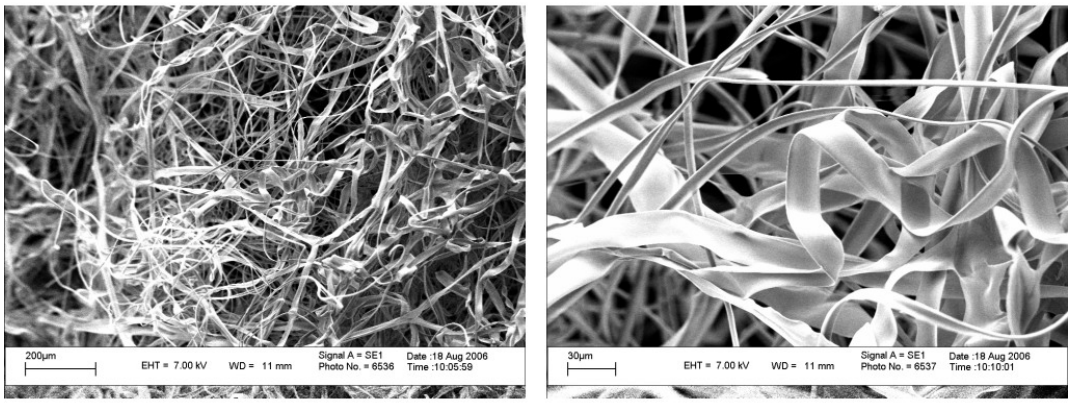

Figure C.3 *SEM images illustrating the surface morphology of electrospun 34wt% (short) PDMS nanofibers with an initial solution concentration of 15% (w/w)*

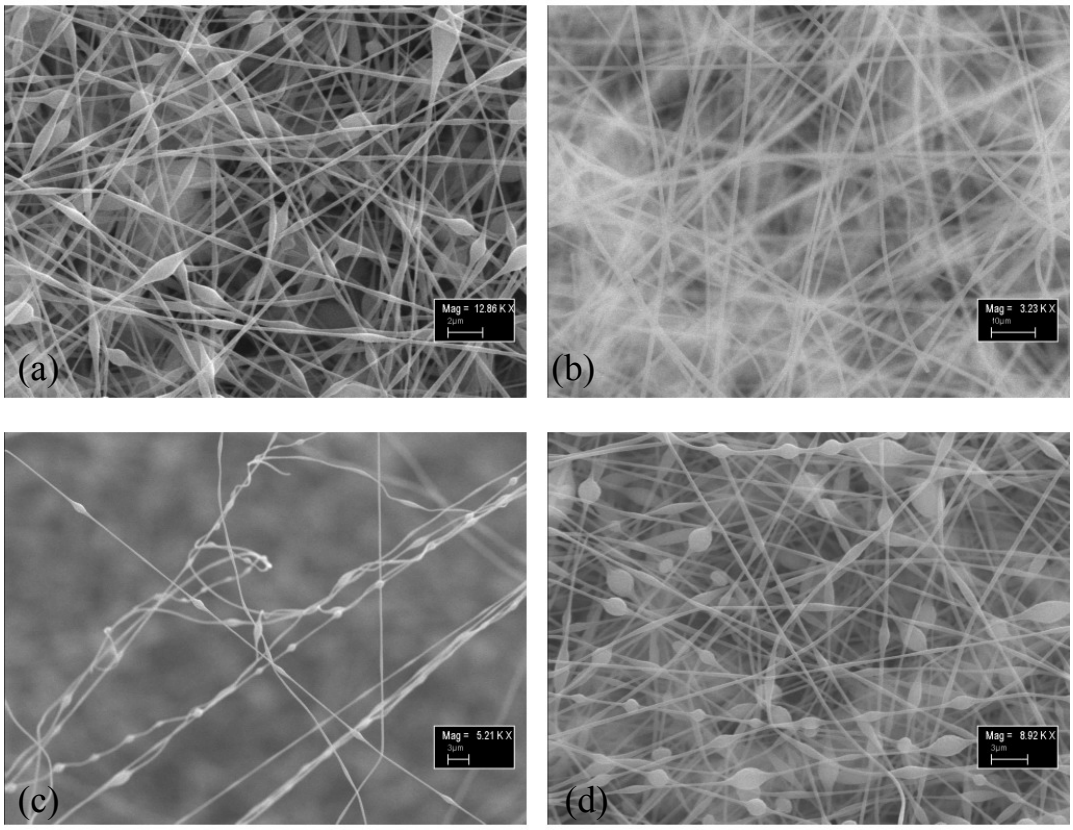

Figure D.1 *SEM images illustrating the changes in surface morphology as a function of varying TCD's of 10wt% (short) PDMS electrospun nanofibers . Figures a and b was spun at a TCD of 10cm, Figure c at 15cm and Figure d at 20cm.*

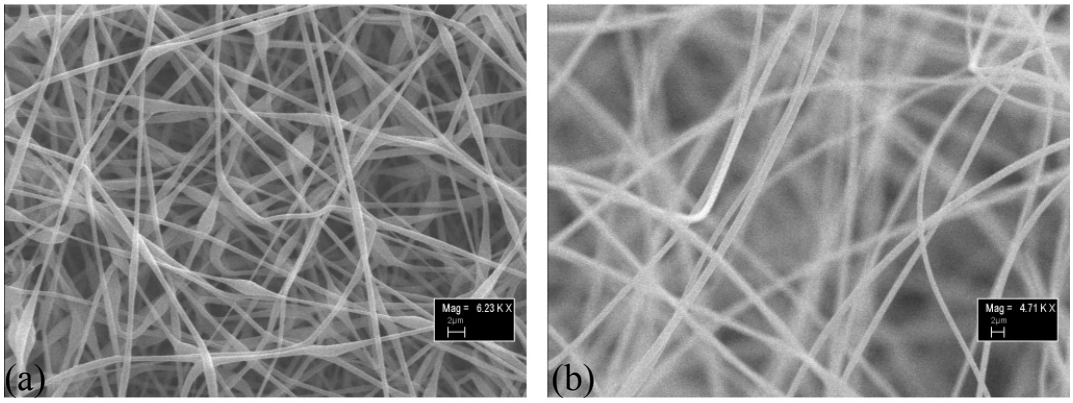

Figure D.2 *SEM images illustrating the changes in surface morphology as a function of varying TCD's of 23wt% (short) PDMS electrospun nanofibers. Figure a was spun at a TCD of 15cm and Figure b at 20cm*

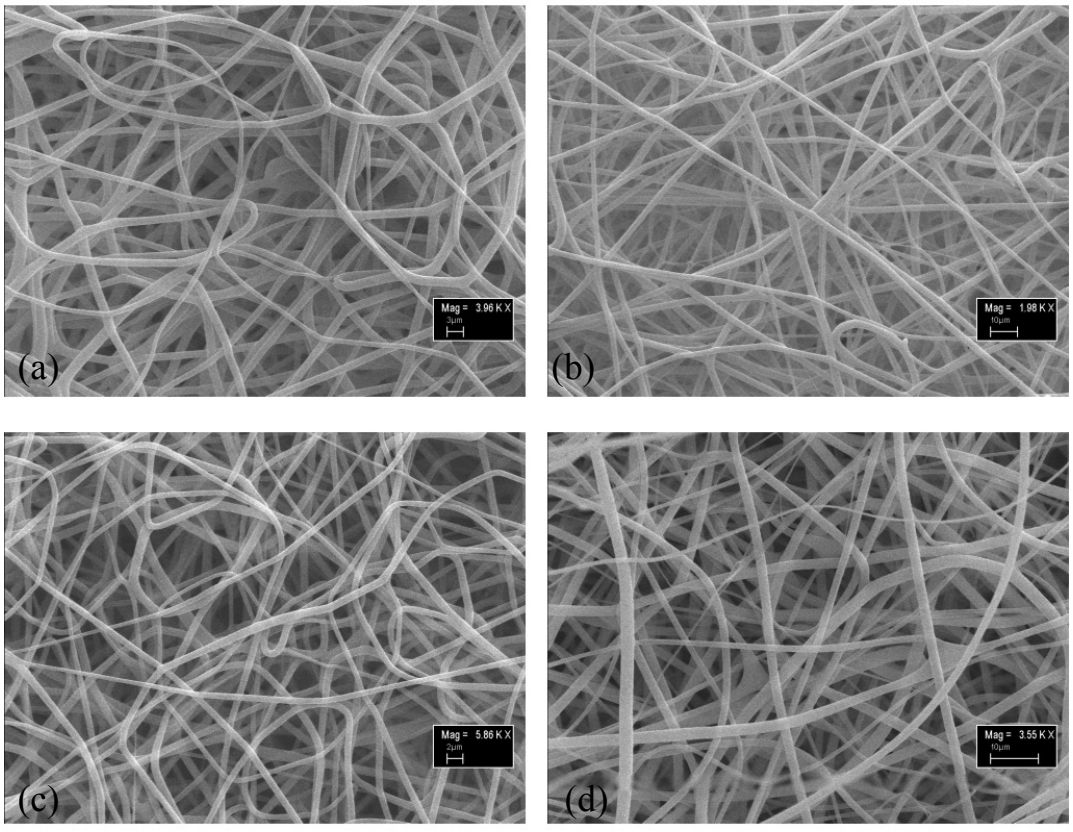

Figure D.3 *SEM images illustrating the changes in surface morphology as a function of varying TCD's of 34wt% (short) PDMS electrospun nanofibers. Figures a and b was spun at a TCD of 10cm, Figure c at 15cm and Figure d at 20cm.*

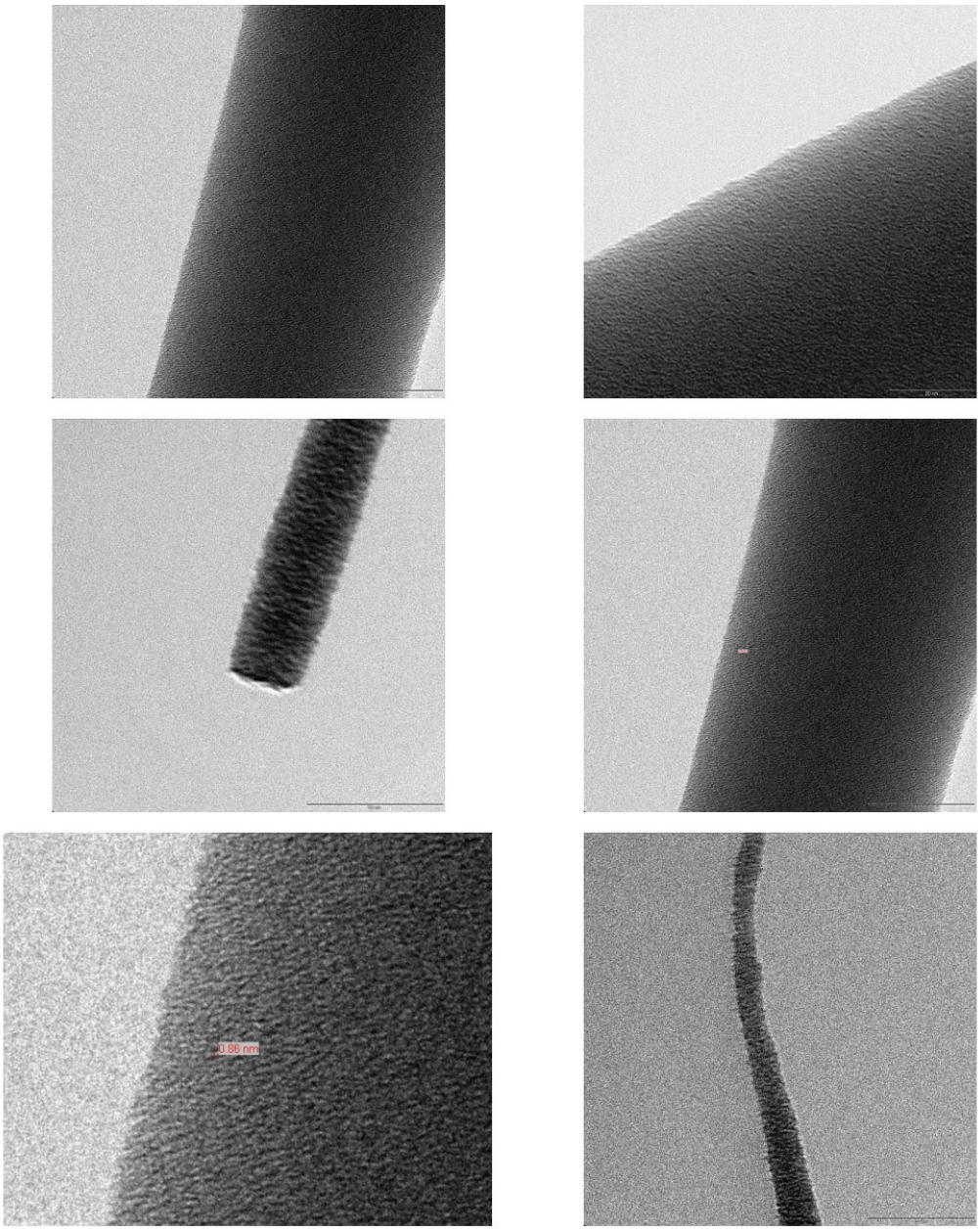

Figure E.1 *TEM images of electrospun 34wt% (short) PDMS nanofibers before annealing*

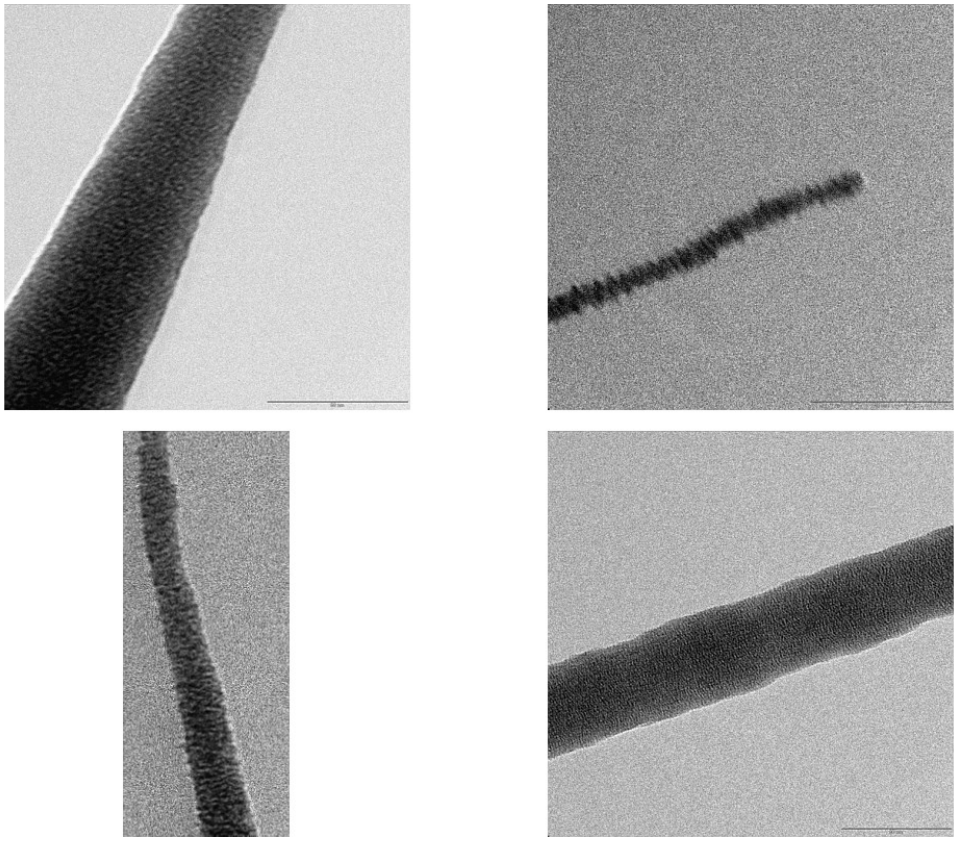

Figure E.2 *TEM images of electrospun 34wt% (short) PDMS nanofibers before annealing*

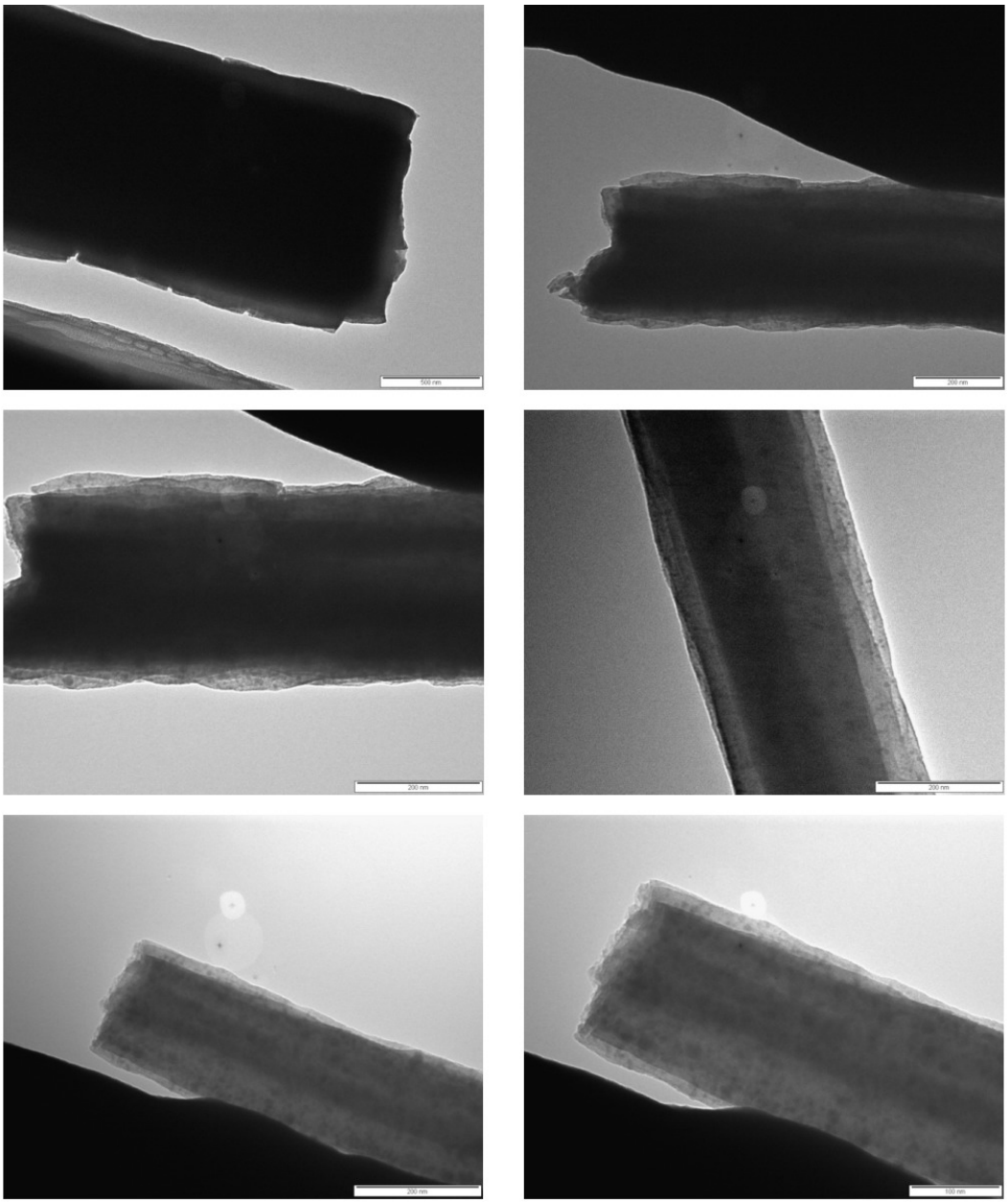

Figure E.3 *TEM images of electrospun 34wt% (short) PDMS nanofibers after annealing in under nitrogen atmosphere for 3hours at 280°C*

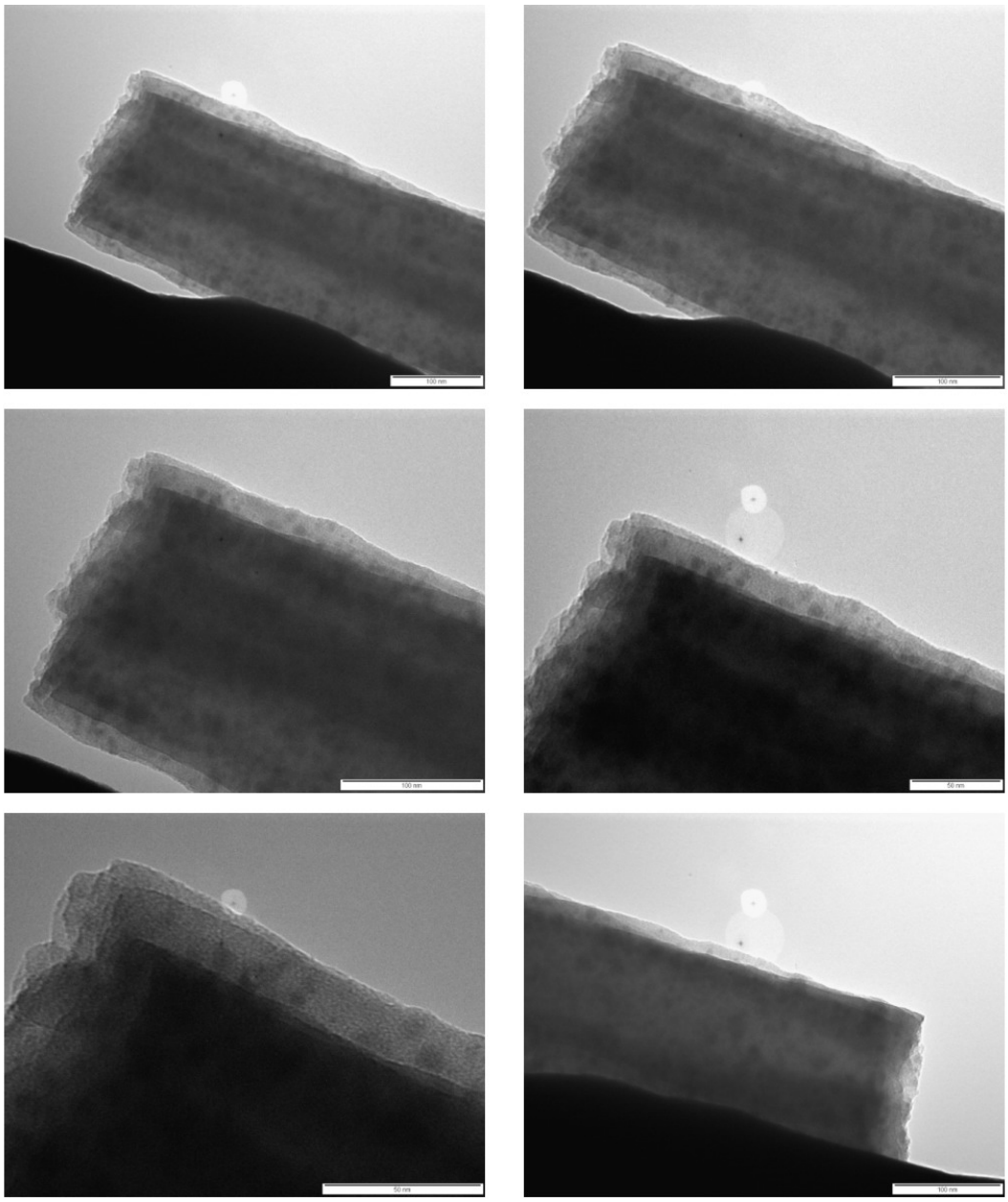

Figure E.4 *TEM images of electrospun 34wt% (short) PDMS nanofibers after annealing in under nitrogen atmosphere for 3hours at 280^{o}C*